

PROCEEDINGS

OF 4TH INTERNATIONAL CONFERENCE ON
COMMUNICATIONS, ELECTROMAGNETICS AND MEDICAL
APPLICATIONS (CEMA'09)

Organized by:



FACULTY OF TELECOMMUNICATIONS
TECHNICAL UNIVERSITY OF SOFIA, BULGARIA



NATIONAL TECHNICAL UNIVERSITY OF ATHENS, GREECE,
SCHOOL OF ELECTRICAL AND COMPUTER ENGINEERING

NATIONAL TECHNICAL
UNIVERSITY OF ATHENS,
GREECE



SCHOOL OF ELECTRICAL
AND COMPUTER
ENGINEERING

Sofia, Bulgaria
8th - 10th October, 2009

KING

Edited by Prof. Dr. Eng. **Dimiter Tz. Dimitrov**

All rights reserved. This book, or parts there of, may not be reproduced in any form or by any means, electronic or mechanical, including photocopying or any information storage and the retrieval system now known or to be invented without written permission from the Publisher.

ISBN 978-954-9518-63-4

Printed in Bulgaria



D. Dimitrov

Dear Colleagues,

It's my privilege to thank you all for your contributions submitted at the 4th regular International Conference on 'Communication, Electromagnetic and Medical Applications' CEMA'09. This is one conference which should help future collaboration between engineering, especially communication technologies and medicine. This is an important scientific event not only in the Balkan region, but in Europe, also. The International Conference on Communication, Electromagnetism and Medical Application CEMA'09 is dedicated to all essential aspects of the development of global information and communication technologies and their impact for medicine. The objective of the Conference is to bring together lecturers, researchers and practitioners from different countries, working on the field of communication, electromagnetism and medical applications, computer simulation of electromagnetic field, in order to exchange information and bring new contributions to this important field of engineering design and application in medicine. The Conference will bring you the latest ideas and development of the tools for the above mentioned scientific areas directly from their inventors. The objective of the Conference is also to bring together the academic community, researchers and practitioners working in the field of Communication, Electromagnetic and Medical Applications, not only from all over Europe, but also from America and Asia, in order to exchange information and present new scientific and technical contributions. Many well known scientists took part in conference preparation as members of the International Scientific Committee or/and as reviewers of submitted papers/. I would like to thank all of them for their efforts, for their suggestions and advices.

On behalf of the International Scientific Committee, I would like to wish you successful presentations of your papers, successful discussions and new collaborations for your future scientific investigations. Engineering and medicine should provide a high level of life for all people.

Dimiter Tz. Dimitrov
Conference Chairman

INTERNATIONAL SCIENTIFIC COMMITTEE

Honorary Chairman:

Prof. N. UZUNOGLU, National Technical University of Athens, Greece

Chairman:

D. TZ. DIMITROV, Technical University of Sofia, Bulgaria

Vice Chairmen:

P. FRANGOS, National Technical University of Athens, Greece

L. SVILAINIS, Kaunas University of Technology, Lithuania

Members:

N. AMPILOVA,	University of Perersburg, Russia
A. BEKJARSKY,	Technical University of Sofia, Bulgaria
B. DEKERIS,	Kaunas University of Technology, Litvania
V. DEMIREV,	Technical University of Sofia, Bulgaria
N. DIB,	Jordan University of Science and Technology, Jordan
M. DONTSCHEWA,	University of Applied Sciences, Dorbirn, Austria
V. DUMBRAVA,	Kaunas University of Technology, Litvania
D. EIDUKAS,	Kaunas University of Technology, Litvania
E. GAGO-RIBAS,	University of Oviedo, Spain
G. GOUSSETIS,	Heriot - Watt University, United Kingdom
A. GRIGORIEV,	St. Petersburg University, Russia.
S. GUERGOV,	Technical University of Sofia, Bulgaria
S. Ver HOEYE,	University of Oviedo, Spain
M. HOFMANN,	University of Ulm, Germany
V. HRISTOV,	University of Blagoevgrad, Bulgaria
I. ILIEV,	Technical University of Sofia, Bulgaria
L. JORDANOVA,	Technical University of Sofia, Bulgaria
R. KRIVICKAS,	Kaunas University of Technology, Litvania
A. LAZAROV,	Bourgas Free University, Bulgaria
G. MALLET,	University "Sophia Antipolis", Nice, France
G. MATSOPOULOS,	National Technical University of Athens, Greece
V. MARINKEV,	Medical University of Plovdiv, Bulgaria
M. MARTINS,	Instituto Superior Técnico, Lisboa, Portugal
M. MORALES-GONZALES,	University of Valladolid, Spain
K. NIKITA,	National Technical University of Athens, Greece
M. NIKOLOVA,	High Naval School, Varna, Bulgaria
J. PETROVSKA,	Medical University of Sofia, Bulgaria
F. PRATO,	University of Western Ontario, Canada
H. ROTH,	University of Siegen, Germany
S. SAUTBEKOV,	Euroasian University, Astana, Kazakhstan
A. SAVOV,	Medical University of Sofia, Bulgaria
S. SAVOV,	Technical University of Varna, Bulgaria
H-P. SCHADE,	Technical University of Ilmenau, Germany
L. SONG,	Technical University of Harbin, China
A. USHEVA,	University of Boston, USA

REVIEWERS

M. DONTSCHEWA,	University of Applied Sciences, Dornbirn, Austria
D. DIMITROV,	Technical University of Sofia, Bulgaria
V. MARINKEV,	Medical University of Plovdiv, Bulgaria
J. PETROVSKA,	Medical University of Sofia, Bulgaria
A. SAVOV,	Medical University of Sofia, Bulgaria
K. VLADIMIROV,	Medical University of Sofia, Bulgaria
L. SONG,	Technical University of Harbin, China
S. Ver HOEYE,	University of Oviedo, Spain
E. BOEMO,	Technical University of Madrid, Spain
M. HOFMANN,	University of Ulm, Germany
F. KLETT,	Franhofer Institute, Ilmenau, Germany
H-P. SCHADE,	Technical University of Ilmenau, Germany
H. BERG,	Technical University of Jena, Germany
Q. BALZANO,	University of Maryland, USA
A. USHEVA,	University of Boston, USA
G. MALLET,	University "Sophia Antipolis", Nice, France
M. MARTINS,	Instituto Superior Técnico, Lisboa, Portugal
N. ESCUDEIRO	Instituto Superior Técnico, Porto, Portugal

REGISTRATION

October, 08th 09h - 16h

The conference registration desk will be in the room 12134, 12th building,
Faculty of Electrotechnique, Technical University of Sofia

CONFERENCE PROGRAM

Opening ceremony and welcome party

08th October

09h-10h, room 12134 in 12th building

SCIENTIFIC PROGRAM

FIRST SESSION

10h – 11h30, room 12134 in 12th building

Chairman: Prof. D. Dimitrov, Technical University of Sofia, Bulgaria

1. *L. Svilainis, V. Dumbrava, Kaunas University of Technology, Lithuania,*
LED far-field pattern approximation functions study
2. *L. Sinkunas, L. Svilainis, V. Dumbrava, Kaunas University of Technology, Lithuania,*
Correlation properties of spread spectrum signals with multiband losses
3. *A. Chaziachmetovas, V. Dzenkauskas, Kaunas University of Technology, Lithuania,*
Analysis of complex impedance measurement I-V method
4. *V. Dzenkauskas, A. Chaziachmetovas, Kaunas University of Technology, Lithuania,*
Method selection and error evaluation for fault place detection in underground
heat distribution pipes
5. *Valentin Hristov, South-West University – Blagoevgrad, Bulgaria,*
Using Lightweight Directory Access Protocol for Service Level Specifications Ad-
ministration
6. *D. Brodić, University of Belgrade, Technical Faculty Bor, Serbia, Z. Milivojević, Tech-
nical College Niš, Serbia,*
Comparison of the Gaussian Window and Water Flow Algorithm for Printed and
Handwritten Text Parameters Extraction

Coffe-break
11h30 – 12h

SECOND SESSION

12h – 13h30, room 12134 in 12th building

Chairman: Prof. L. Svilainis, Kaunas University of Technology, Lithuania

1. *A. Chrysostomou, National Technical University of Athens, Greece, I. Zorbas, National
Technical University of Athens, Greece, E. Papkelis, National Technical University of Ath-
ens, Greece, P. Frangos, National Technical University of Athens, Greece,*
A Three-Dimensional Radio Coverage Prediction Model for Urban Outdoor Envi-
ronment using Physical Optics and Physical Theory of Diffraction
2. *G. S. Kliros, Hellenic Air-Force Academy, Dekeleia Air-Force Base, Attica, Greece,
G. Kyritsis, Hellenic Air-Force Academy, Dekeleia Air-Force Base, Attica, Greece,
D. Touzloudis, Hellenic Air-Force Academy, Dekeleia Air-Force Base, Attica, Greece,*
FDTD analysis of a conical microstrip antenna on EBG substrate

3. *H. D. Hristov, Department of Electronics, UTFSM, Valparaíso, Chile, M. S. Leong, Department of Electrical and Computer Engineering, NUS, Singapore, M. B. Perotoni, Department of Information Engineering, UFABC, Brazil, G. S. Kirov, Department of Radio-technics, Technical University, Varna, Bulgaria, W. Grote, Department of Electronics, UTFSM, Valparaíso, Chile,*
Waveguide-Fed Backfire Antennas for Low-Terahertz Frequencies
4. *Lidia T. Jordanova, Technical University of Sofia, Bulgaria, Jordan I. Nenkov, Technical University of Sofia, Bulgaria,*
On a Method to Increase the Effectiveness of Cable VoD Systems
5. *A. Bekiarski, Technical University of Sofia, Bulgaria, S. Pleshkova-Bekiarska, Technical University of Sofia, Bulgaria,*
Speaker Tracking Mobile Robot Audio Visual System for Surveillance Applications
6. *A. Bekiarski, Technical University of Sofia, Bulgaria*
Moving Objects Tracking Algorithm Design and Testing for Mobile Robots
7. *S. Sautbekov, Euroasian National University, Astana, Kazakhstan, P. Frangos, National Technical University of Athens, Greece,*
Radiation of electric and magnetic dipoles in uniaxial magnetic crystal media

Lunch

13h30 - 14h30

THIRD SESSION

14h30 - 16h, room 12134 in 12th building

Chairman: Prof. A. Bekiarski, Technical University of Sofia, Bulgaria

1. *Veska M. Georgieva, Technical University of Sofia, Bulgaria,*
Noise Reduction and Enhancement of Computed Tomography Images
2. *Veska M. Georgieva, Technical University of Sofia, Bulgaria,*
GUI for Morphological Processing of Medical Images
3. *S. Guergov, Technical University of Sofia, Bulgaria, D. Dimitrov, Technical University of Sofia, Bulgaria, A. Dimitrov, Technical University of Sofia, Bulgaria, Miglena Dontschewa, FH Vorarlberg University of Applied Sciences - Dornbirn, Austria,*
Design of System for Therapy with Running Low Frequency Magnetic Field
4. *S. Guergov, Technical University of Sofia, Bulgaria, D. Dimitrov, Technical University of Sofia, Bulgaria, Miglena Dontschewa, FH Vorarlberg University of Applied Sciences - Dornbirn, Austria,*
Design of Girdle Coil Flexible System for Magnetotherapy

5. *S. Guergov, Technical University of Sofia, Bulgaria, D. Dimitrov, Technical University of Sofia, Bulgaria, P. Petrov, Medical centre - Ivanjane*
System for Therapy with Acupressure and Low Frequency Magnetic Field
6. *D. Dimitrov, Technical University of Sofia, Bulgaria, N. Ralev, Technical University of Sofia, Bulgaria, Lukosevicius Arunas, Kaunas University of Technology, Lithuania,*
Simultaneously Influence of Permanent Electrical Field and Low Frequency Magnetic Field on the Human Body

Coffe-break

16h – 16h30, room 12134 in 12th building

FOUR SESSION

16h30 – 18h, room 12134 in 12th building

Chairman: Prof. P. Frangos, National Technical University of Athens, Greece

1. *Z. Cvetkov, Technical University of Sofia, Bulgaria, S. Guergov, Technical University of Sofia, Bulgaria, D. Dimitrov, Technical University of Sofia, Bulgaria, P. Decheva, Technical University of Sofia, Bulgaria, A. Savov, Medical University of Sofia, Bulgaria*
Modelling of influence of electromagnetic field on movement of ions in the human body
2. *M. Nikolova, N. Y. Vaptsarov, Naval Academy, Varna, Bulgaria, Tz. Dimitrova, Technical University of Sofia, Bulgaria,*
Computer simulation of ECG signal restoration
3. *Tz. Dimitrova, Technical University of Sofia, Bulgaria,*
Medical data risk exposure
4. *Song Li-xin, Harbin University of Science And Technology, Harbin, China, Chang Rui-feng, Harbin University of Science And Technology, Harbin, China, Wang Qian, Harbin University of Science And Technology, Harbin, China,*
Content-Based Retrieval Of Calcification Lesions In Mammography
5. *Natalia Ampilova, St. Petersburg State University, Russia, Darina Nikolaeva, St. Petersburg State University, Russia,*
On application of correlation dimension for EEG analysis of patients with epilepsy
6. *Ljudmila Roumenova Taneva, Technical University of Sofia, Bulgaria,*
Intelligent module for data exchange using CAN interface

CLOSING SESSION

18 – 18h30, room 12134 in 12th building

SOCIAL PROGRAM

Banquet

October, 08th, 19h30

Trip

to Ethnographie museum "Etara" and "Trojan monastery"

October, 09th

CONTACT US :

<http://www.tu-sofia.bg/fktt/cema09/>

GENERAL INFORMATION AND SUBMISSION OF CONTRIBUTIONS

Prof. Dr. D. Dimitrov

Faculty of Telecommunications

Technical University of Sofia

8, Kliment Ohridsky str.

1756 Sofia, Bulgaria

Phone/Fax: ++359 2 9652278

E-mail: dcd@tu-sofia.bg

Prof. Dr. P. Frangos

National Technical University of Athens

School of Electrical and Computer Engineering

9, Iroon Polytechniou Str.,

157 73 Zografou, Athens, Greece

Phone: 00 30 210 772 3694

Fax: 00 30 210 772 2281

E-mail: pfrangos@central.ntua.gr

TABLE OF CONTENTS

LED FAR-FIELD PATTERN APPROXIMATION FUNCTIONS STUDY	1
<i>L. Svilainis, V. Dumbrava</i>	
CORRELATION PROPERTIES OF SPREAD SPECTRUM SIGNALS WITH MULTIBAND LOSSES.....	6
<i>L. Sinkunas, L. Svilainis, V. Dumbrava</i>	
ANALYSIS OF COMPLEX IMPEDANCE MEASUREMENT I-V METHOD.....	11
<i>A. Chaziachmetovas, V. Dzenkauskas</i>	
METHOD SELECTION AND ERROR EVALUATION FOR FAULT PLACE DETECTION IN UNDERGROUND HEAT DISTRIBUTION PIPES	15
<i>V. Dzenkauskas, A. Chaziachmetovas</i>	
USING LIGHTWEIGHT DIRECTORY ACCESS PROTOCOL FOR SERVICE LEVEL SPECIFICA- TIONS ADMINISTRATION	19
<i>Valentin Hristov</i>	
COMPARISON OF THE GAUSSIAN WINDOW AND WATER FLOW ALGORITHM FOR PRINTED AND HANDWRITTEN TEXT PARAMETERS EXTRACTION	24
<i>D. Brodić, Z. Milivojević</i>	
A THREE-DIMENSIONAL RADIO COVERAGE PREDICTION MODEL FOR URBAN OUTDOOR ENVIRONMENT USING PHYSICAL OPTICS AND PHYSICAL THEORY OF DIFFRACTION.....	30
<i>Chrysostomou, I. Zorbas, E. Papkelis, P. Frangos</i>	
FDTD ANALYSIS OF A CONICAL MICROSTRIP ANTENNA ON EBG SUBSTRATE	35
<i>G. S. Kliros, G. Kyritsis, D. Touzloudis</i>	
WAVEGUIDE-FED BACKFIRE ANTENNAS FOR LOW-TERAHERTZ FREQUENCIES.....	39
<i>H. D. Hristov, M. S. Leong, M. B. Perotoni, G. S. Kirov, W. Grote</i>	
ON A METHOD TO INCREASE THE EFFECTIVENESS OF CABLE VOD SYSTEMS.....	44
<i>Lidia T. Jordanova, Jordan I. Nenkov</i>	
SPEAKER TRACKING MOBILE ROBOT AUDIO VISUAL SYSTEM FOR SURVEILLANCE APPLICATIONS.....	49
<i>A. Bekiarski, S. Pleshkova-Bekiarska</i>	
MOVING OBJECTS TRACKING ALGORITHM DESIGN AND TESTING FOR MOBILE ROBOTS.....	52
<i>A. Bekiarski</i>	

RADIATION OF ELECTRIC AND MAGNETIC DIPOLES IN UNIAXIAL MAGNETIC CRYSTAL MEDIA.....	56
<i>S. Sautbekov, P. Frangos</i>	
NOISE REDUCTION AND ENHANCEMENT OF COMPUTED TOMOGRAPHY IMAGES.....	60
<i>Veska M. Georgieva</i>	
GUI FOR MORPHOLOGICAL PROCESSING OF MEDICAL IMAGES.....	64
<i>Veska M. Georgieva</i>	
DESIGN OF SYSTEM FOR THERAPY WITH RUNNING LOW FREQUENCY MAGNETIC FIELD.....	68
<i>S. Guergov, D. Dimitrov, A. Dimitrov, M. Dontschewa</i>	
DESIGN OF GIRDLE COIL FLEXIBLE SYSTEM FOR MAGNETOTHERAPY.....	71
<i>S. Guergov, D. Dimitrov, M. Dontschewa</i>	
SYSTEM FOR THERAPY WITH ACUPRESSURE AND LOW FREQUENCY MAGNETIC FIELD.....	75
<i>S. Guergov, D. Dimitrov, P. Petrov</i>	
SIMULRTANEOUSLY INFLUENCE OF PERMANENT ELECTRICAL FIELD AND LOW FREQUENCY MAGNETIC FIELD ON THE HUMAN BODY.....	79
<i>D. Dimitrov, N. Ralev, Lukosevicius Arunas</i>	
MODELLING OF INFLUENCE OF ELECTROMAGNETIC FIELD ON MOVEMENT OF IONS IN THE HUMAN BODY.....	82
<i>Z. Cvetkov, S. Guergov, D. Dimitrov, P. Decheva, A. Savov</i>	
COMPUTER SIMULATION OF ECG SIGNAL RESTORATION.....	86
<i>M. Nikolova, N. Y. Vaptsarov, Tz. Dimitrova</i>	
MEDICAL DATA RISK EXPOSURE.....	90
<i>Tz. Dimitrova</i>	
CONTENT-BASED RETRIEVAL OF CALCIFICATION LESIONS IN MAMMOGRAPHY.....	94
<i>Song Li-xin, Chang Rui-feng, Wang Qian</i>	
ON APPLICATION OF CORRELATION DIMENSION FOR EEG ANALYSIS OF PATIENTS WITH EPILEPSY.....	99
<i>Natalia Ampilova, Darina Nikolaeva</i>	
INTELLIGENT MODULE FOR DATA EXCHANGE USING CAN INTERFACE.....	102
<i>Ljudmila Roumenova Taneva</i>	

AUTHOR INDEX

AMPILOVA N.	99
ARUNAS L.	79
BEKIARSKA S.PL.	49
BEKIARSKI A.	49, 52
BRODIĆ D.	24
CHANG RUI-FENG	94
CHAZIACHMETOVAS A.	11, 15
CHRYSOSTOMOU, I. Z.	30
CVETKOV Z.	82
DECHEVA P.	82
DIMITROV A.	68
DIMITROV D.	68, 71, 75, 79, 82
DIMITROVA TZ.	86, 90
DONTSHEWA M.	68, 71
DUMBRAVA V.	1, 6
DZENKAUSKAS V.	11, 15
FRANGOS P.	30, 56
GEORGIEVA V.	60, 64
GROTE W.	39
GUERGOV S.	68, 71, 75, 82
HRISTOV H.	39
HRISTOV V.	19
JORDANOVA L.	44
KIROV G.	39
KLIROS G.	35
KYRITSIS G.	35
LEONG M.S.	39
MILIVOJEVIĆ Z.	24
NENKOV J.	44
NIKOLAEVA D.	99
NIKOLOVA M.	86
PAPKELIS E.	30
PEROTONI M.B.	39
PETROV P.	75
RALEV N.	79
SAUTBEKOV S.	56
SAVOV A.	82
SINKUNAS L.	6
SONG LI-XIN	94
SVILAINIS L.	1, 6
TANEVA L.	102
TOUZLOUDIS D.	35
VAPTSAROV N.Y.	86
WANG QIAN	94

LED FAR-FIELD PATTERN APPROXIMATION FUNCTIONS STUDY

L. Svilainis, V. Dumbrava

Signal processing department, Kaunas University of Technology
Studentu str. 50, LT-51368 Kaunas, Lithuania
T, +370 37 300532; F, +370 37 753998; E, linas.svilainis@ktu.lt / vytautas.dumbrava@ktu.lt

Abstract

The approximation functions of the far-field pattern (FFP) of the light emitting diodes (LED) used in LED video displays have been investigated. The simplicity of an approximation function and ease of analytical handling have been targeted. Four candidate approximation functions were identified and the approximation performance evaluation criteria were analyzed. The relative intensity approximation root mean square (RMS) error and relative half power beam angle error have been selected. The influence of the angles range used in approximation was analyzed. The final performance evaluation is done on eight batches of LEDs sample. These LED samples have been chosen to represent the variety of the FFP shapes, the main colors and the range of the most popular viewing angles were used in LED displays design. The approximation by Gaussian function with DC offset performed the best.

1. INTRODUCTION

The light emitting diode (LED) application in video displays has proven a reasonable alternative when a large area of a high brightness imaging is required [1]. LED directional properties among the other LED parameters define the image quality at various viewing angles [2, 3]. The far-field pattern (FFP) [4] is used to determine the spatial directivity properties. The measurement is usually performed by measuring the intensity I distribution over the observation angles Θ , say $I(\Theta)$. A numerical parameters, such as: the peak emission direction Θ_{peak} and a half power beam angle $2\Theta_{0.5}$, where the source's relative intensity is dropping to the half of the peak emission can be obtained from the FFP using the measured $I(\Theta)$.

The FFP of the real LED can be treated as a sum of an ideal LED FFP and a clutter created by sidewall emissions, reflection distortions, tinting, etc. The LEDs used in video displays have wide $2\Theta_{0.5}$ angles. Here the main portion of FFP is created by focusing lens. In addition, these LEDs usually are tinted. Then such LED FFP can be approximated by a simple function [4]. The intention is to use this expression in LED directivity *in-situ* measurement system [5] without dismantling the LEDs from the tile. The goal of this paper was to establish a numerical approximation performance evaluation criterion, to provide the comparison and to indicate the best candidate function for FFP approximation.

2. THE APPROXIMATION FUNCTIONS

The polynomial fit could be the first candidate for any approximation. The second order polynomial fit for FFP approximation was suggested. The LED intensity at some angle Θ is a parabolic function of a form

$$I(\Theta) = a_0 + a_1\Theta + a_2(\Theta)^2, \quad (1)$$

where a_0, a_1, a_2 are polynomial coefficients. Obtaining the equation for $I(\Theta_{\text{peak}})$ and solving for a half of it, the viewing angle is

$$2\Theta_{0.5} = -\frac{\sqrt{2a_1^2 - 8a_0a_2}}{2a_2}. \quad (2)$$

The publication [4] presents the \cos in power ($g-1$) function as a candidate for LED FFP approximation. A point light source is usually assumed in luminous intensity measurements. The intensity I angular distribution can be approximated as:

$$I(\Theta) = I_{\text{max}} \cos(\Theta - \Theta_{\text{peak}})^{g-1}, \quad (3)$$

where g is a coefficient, proportional to viewing angle $2\Theta_{0.5}$. Solving (3) for $2\Theta_{0.5}$ it can be obtained

$$2\Theta_{0.5} = 2 \arccos\left(e^{\left(\frac{\ln(2)}{1-g}\right)}\right). \quad (4)$$

Gaussian approximation is most often used in RF antenna pattern approximation [6] as an ideal-

ized pattern of an antenna having a smooth main-lobe with no sidelobes:

$$I(\theta) = I_{\max} \cdot e^{\left(-\ln(2) \frac{(\theta - \theta_{peak})^2}{\theta_{0.5}^2} \right)}. \quad (5)$$

Ambient light during the measurement process under some circumstances can not be completely removed and the DC offset occurs. Then the Gaussian with DC offset I_{off} can be used for approximation:

$$I(\theta) = I_{off} + I_{\max} \cdot e^{\left(-\ln(2) \frac{(\theta - \theta_{peak})^2}{\theta_{0.5R}^2} \right)}. \quad (6)$$

The half power beam angle in (6) is evaluated after removing the DC component of the FFP. This property is useful if DC offset occurs due to the ambient light. But in case the offset is a property of LED then the half power angle will have a large systematic error. The half power angle has a notation with the index R ($2\theta_{0.5R}$) to distinguish from the conventional result. Then the corrected half power angle is:

$$2\theta_{0.5} = \frac{2\theta_{0.5R} \sqrt{\ln\left(\frac{I_{\max} - I_{off}}{I_{\max}}\right) - \ln(2)}}{\ln(2)}. \quad (7)$$

The candidate search was limited by four functions mentioned above.

The LEDs used in video screens usually have elliptical directivity diagram, i.e. vertical and horizontal directivity differ. The amount of possible horizontal and vertical angles combinations is large. The analysis can be greatly simplified if only the one dimensional approximation is used. The analyzed approximation functions can be easily converted into two dimensional by multiplying the horizontal $I_H(\theta_H)$ and vertical $I_V(\theta_V)$ diagram approximation functions:

$$I_{2D}(\theta_H, \theta_V) = I_H(\theta_H) \cdot I_V(\theta_V). \quad (8)$$

Then analysis was concentrated on 1D approximation functions.

3. EVALUATION CRITERIA

The relative value of the intensity approximation error root mean square (RMS) is suggested as maximum likeness criterion

$$\delta_{RMS} = \frac{\sqrt{\int_{\theta_1}^{\theta_2} (I(\theta) - \tilde{I}(\theta))^2 d\theta}}{\sqrt{\int_{\theta_1}^{\theta_2} (I(\theta))^2 d\theta}} \cdot 100\%, \quad (9)$$

where $I(\theta)$ is the original FFP, $\tilde{I}(\theta)$ is the approximating function, θ_1 and θ_2 are the boundary values of the approximation range. The batch of 40 blue LEDs with specified 70 degrees horizontal angle has been used for analysis. Results obtained by applying this criterion are presented in Figure 1. Relative intensity approximation error is presented as a box-and-whisker plot. The box encloses 50% of the data (the interquartile range, IQR), a line in the box represents the median; mean is shown as a square. The whiskers are of 1.5 IQR and the stars represent the minima and maxima of the data.

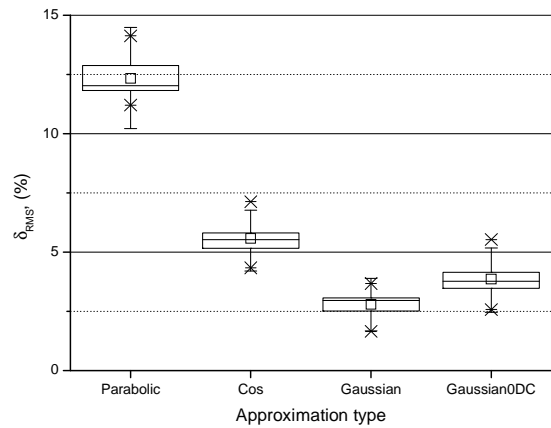


Fig. 1. Intensity approximation error δ_{RMS} vs. approximation functions

The performance of various approximation functions is clearly distinguishable. Application of the Gaussian function possesses the lowest intensity approximation error reaching 2.5%. The parabolic function approximation has the worst performance (12%).

It would be good to have some numerical performance values that are related to the parameters of LED directivity. Therefore, the analysis of θ_{peak} and $2\theta_{0.5}$ values obtained from approximation was suggested.

The initial investigation has been carried out on θ_{peak} values before the approximation and after the approximation. The same LEDs' batch as in Fig.2 has been used for the experiments. It is interesting to point out that peak emission direction obtained from the approximation function is following the

values obtained from the original FFP. The results indicated that mean values of Θ_{peak} have a similar variance for all approximation types. The explanation is that LEDs dedicated for professional LED display have been used. Those LEDs are tinted, so FFP is quite smooth and it makes no sense to analyze the Θ_{peak} values.

The same analysis can be applied on half power angle of $2\Theta_{0.5}$. The absolute error of $2\Theta_{0.5}$ was calculated as a difference between $2\Theta_{0.5A}$ angles obtained from the approximation and $2\Theta_{0.5O}$ of original FFP:

$$\varepsilon_{2\Theta_{0.5}} = 2\Theta_{0.5A} - 2\Theta_{0.5O} \quad (10)$$

The results when $2\Theta_{0.5}$ error analysis criterion is applied on the same batch as above are presented in Figure 2.

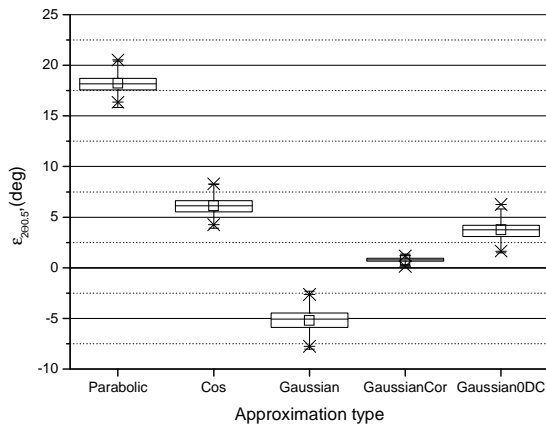


Fig. 2. Half power angle error $\varepsilon_{2\Theta_{0.5}}$ for various approximation functions

There is a difference in angle $2\Theta_{0.5}$ errors obtained for Gaussian approximation using (7) - $2\Theta_{0.5R}$ (labeled as "Gaussian") and corrected according (8) - $2\Theta_{0.5}$ (labeled as "GaussianCor"). The analysis of initial approximation performance study has indicated that the parabolic function has the worst accuracy. The parabolic function is not able to bend up (Figure1) at the lower end of the FFP curve. The result can be different if other approximation range is used. In order to verify whether this assumption is correct the approximation performance for various approximation ranges was investigated.

4. RANGE INFLUENCE

The same batch of blue LEDs has been used for the analysis. The relative intensity approximation

error $\bar{\delta}_{RMS}$ mean has been calculated at every approximation range. The approximation range has been varied from 75° (slightly above $2\Theta_{0.5}$) up to reasonable maximum of 175° (slightly below 180°). Graphs in (Figure 3) indicate that the intensity approximation error is increasing when range is increased. The increase is moderated only for both Gaussian approximations.

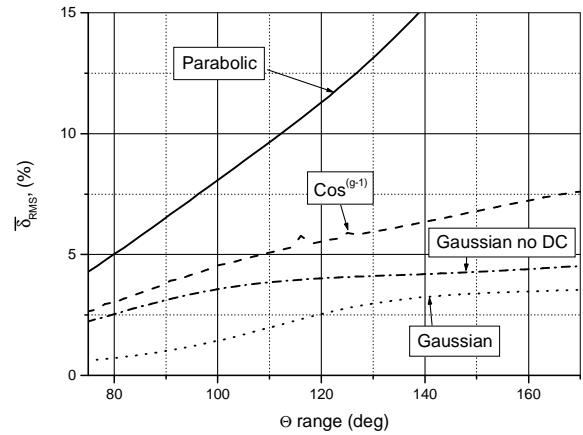


Fig. 3. Intensity approximation error $\bar{\delta}_{RMS}$ mean versus range

The maximum error of Θ_{peak} has been investigated varying the approximation range. The Θ_{peak} error has quite negligible decrease with the range (maximum 0.6° change for the worst case of parabolic approximation). The Gaussian approximation is exhibiting the lowest Θ_{peak} error variation with the range.

The similar analysis was done for the maximum error of $2\Theta_{0.5}$ (12). The same approximation range has been used. The results are presented in Fig. 4.

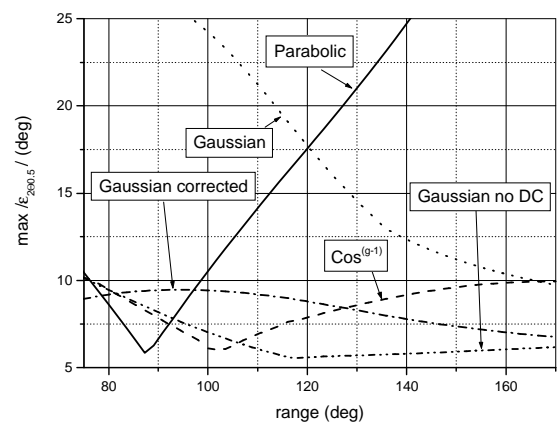


Fig. 4. Max error $\varepsilon_{2\Theta_{0.5}}$ vs. range

Again, only the Gaussian approximations are able to maintain the performance within a moderate range. The results of Figure5 indicate that uncor-

rected $2\Theta_{0.5R}$ for Gaussian approximation is approaching but not reaching the corrected value $2\Theta_{0.5}$ when the range is wide. Gaussian approximation angle $2\Theta_{0.5R}$ has a different physical meaning. Therefore, it was decided to use the corrected angle $2\Theta_{0.5}$ (obtained using (8) for further approximation performance analysis of Gaussian with offset. Almost all the curves in Figure 5 have a minimum. The reason can be that this minimum is the point where the low intensity area approximation is performing with a maximum of efficiency. It was concluded that it makes no sense to use the approximation range much wider than $2\Theta_{0.5}$ since there is no essential data beyond this range. For further analysis it was decided to use the range of 170% of $2\Theta_{0.5}$ (the last minimum position in Figure 4).

5. FINAL EVALUATION

We are aware that presented above analysis has covered only one type of LED. The LEDs of various FFP shape, color, and $2\Theta_{0.5}$ value should be investigated for more extensive final approximation performance evaluation. The LEDs (Table 1) have been chosen to represent the different FFP shapes, the main colors, and the range of most popular angles.

Table 1. LEDs used in investigation

Notation	Specified $2\Theta_{0.5}$, deg	Color	Batch size
BrGH	110	green	20
SBORH	110	red	20
Z2BH	70	blue	37
GrbGH	70	green	20
BrGV	45	green	20
Z2BV	40	blue	37
GrbGV	40	green	20
SBORV	45	red	22

The representative batches have been approximated by all the candidate functions. The obtained approximations have been analyzed using the relative intensity approximation RMS error mean $\bar{\delta}_{RMS}$ and a half power angle error mean $\bar{\delta}_{2\Theta_{0.5}}$. All LEDs have been measured with goniometer by 0.9° angular step in $\pm 90^\circ$ range with resulting 200 data points. Further data processing has been done using MATLAB. To make the decision on the approximation range, the $2\Theta_{0.5}$ angle has been measured on original FFP the first. Then this $2\Theta_{0.5}$ angle was used for approximation range decision. Every

FFP has produced the relative intensity approximation error δ_{RMS} and the relative viewing angle approximation error $\delta_{2\Theta_{0.5}}$. The mean values for these errors have been calculated after processing the whole batch. The results of obtained means of relative approximation error δ_{RMS} and viewing angle approximation error $\delta_{2\Theta_{0.5}}$ for all Table 1 LEDs are presented in Figure 5 and Figure 6.

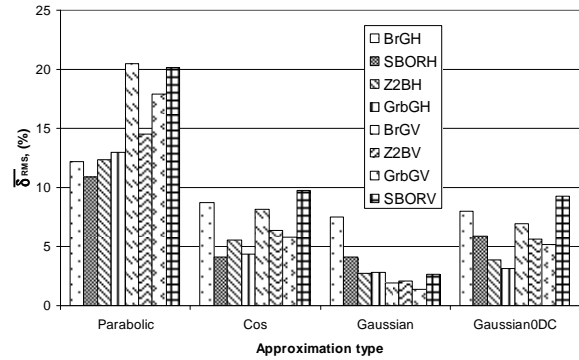


Fig. 5. Relative intensity approximation error $\bar{\delta}_{RMS}$

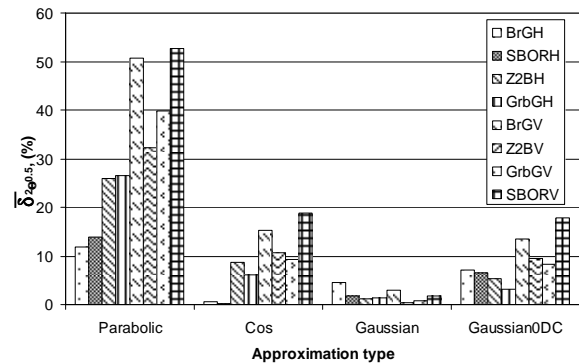


Fig. 6. Error $\bar{\delta}_{2\Theta_{0.5}}$, % of $2\Theta_{0.5}$

Results indicate that Gaussian approximation with DC offset has the best performance: majority of errors for Gaussian δ_{RMS} results are below 5%, and of $2\Theta_{0.5}$ error $\delta_{2\Theta_{0.5}}$ is well below 5% limit. It is interesting to point out that the *cos* in power ($g-1$) function presented better results for the large angle ($>90^\circ$) LEDs. Nevertheless, the individual FFP approximation analysis indicates that *cos* in power ($g-1$) function is getting unstable and the results start to vary significantly at large angles: coefficient g is close to 1 at a large angle so floating point accuracy influence increases.

The research presented in [7] investigated the performance of approximation when FFP original data is corrupted by the noise. The original FFP was added with an additive white Gaussian noise (AWGN) and then the approximation has been applied. The resulting intensity approximation error

was calculated. The average error graph is presented in Figure 7.

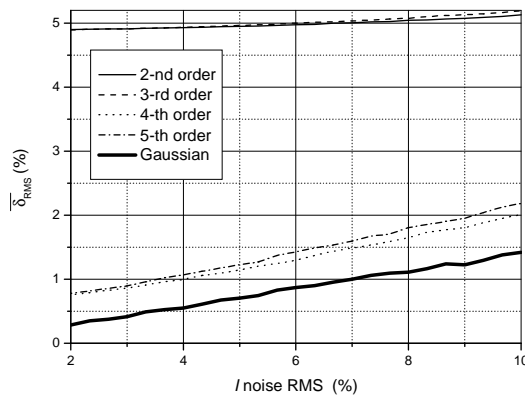


Fig. 7. Relative intensity approximation error $\bar{\delta}_{2\Theta_{0.5}}$ vs. noise

It is interesting to point out that even high polynomial orders possess the approximation error higher than Gaussian approximation. Experiments also indicate that only second order of polynomial has lower than Gaussian standard deviation of obtained $2\Theta_{0.5}$ angles. We think that increasing the polynomial order also increases the sensitivity for noise.

6. CONCLUSIONS

The relative intensity approximation RMS error δ_{RMS} and viewing angle $2\Theta_{0.5}$ error $\mathcal{E}_{2\Theta_{0.5}}$ have been assigned as the approximation performance evaluation criteria. The approximation using the Gaussian with DC offset function performed the best among four candidate functions evaluated. The intensity approximation error $\bar{\delta}_{RMS}$ and $2\Theta_{0.5}$ error $\bar{\delta}_{2\Theta_{0.5}}$ are below 5% limit. Such precision we consider as sufficient. Therefore we indicate the Gaussian with DC offset function as the best candidate for LED FFP approximation if simple analytical form is needed.

References

- [1] F. Nguyen, "Challenges in the design of a RGB LED display for indoor applications", *Synthetic Metals*, vol.122, 2001, pp. 215-219.
- [2] B.Wendler, "LED Viewing Angles vs. LED Video Display Viewing Angles", Technical Note 40, Daktronics Inc., USA, 2002.
- [3] L. Svilainis, V. Dumbrava, "LED goniometry system", *Electronics and Electrical Engineering*, vol. 72 (8), 2006, pp. 69-74.
- [4] "The radiometry of Light Emitting Diodes", Labsphere Inc., UK, 2001.
- [5] L. Svilainis, "LED directivity measurement in-situ", *Measurement*, 2008, vol. 41(6), pp. 647-654.
- [6] D. Barton, "Radar Technology Encyclopedia", Artech House inc., 1998.
- [7] L. Svilainis, V. Dumbrava, "LED Far Field Pattern Approximation Performance Study", in: *Proceedings of 29th IEEE ITI'07 conference, Croatia, 2007*, pp.645-649.

CORRELATION PROPERTIES OF SPREAD SPECTRUM SIGNALS WITH MULTIBAND LOSSES

L. Sinkunas, L. Svilainis, V. Dumbrava

Signal processing department, Kaunas University of Technology
Studentu str. 50, LT-51368 Kaunas, Lithuania

T, +370 37 300532; F, +370 37 753998; E, lsinkunas@gmail.com, linas.svilainis@ktu.lt / vytautas.dumbrava@ktu.lt

Abstract

The probing signals with multiband losses correlation properties were analyzed. We raise the idea that it is not necessary to have a complete signal spectrum for operation: "rake" type signal covering wide bandwidth could perform better than single band of the "rake".

Linear frequency modulated (chirp) type signals were chosen for investigation. The choice of chirp signals was justified by the need for easy controllable frequency response spectrum shape and content. Performance of simple linear-frequency-modulated chirp signals was investigated. Signals were passed thorough the various rake type filters and correlation function performance investigated.

We present the variation of these correlation function parameters: RF and envelope mainlobe beam width and sidelobes level in time domain, equivalent bandwidth, envelope equivalent bandwidth, envelope bandwidth and central weight frequency.

1. INTRODUCTION

The time domain processing is essential in SONAR, RADAR and non destructive testing (NDT) systems. Positioning and navigation systems find its use in a variety of applications. Location estimation is also essential in imaging systems used for NDT [1]. This can be simplified to time-of-flight (ToF) value estimation. The frequency response of the probing signal is defining the correlation properties of the signal received [2,3]. But electrical impedance of the transmission channel [4], losses in propagation media [5] alter the frequency content received: the output of matched filter (correlation function) will change accordingly [6,7]. Numerous publications present the spectral response for such case [2-7]. Especially in telecommunications such signal types prevail: those are addressed as "rake" or "comb" filter or spectrum. But usually, especially in NDT, operation is chosen to avoid the high attenuation areas and concentrate the operation in one complete frequency band. We suggest using a complete signal spectrum. The aim of investigation was to investigate whether operation of "rake" type signal covering wide bandwidth can perform better than single band of the "rake" and what is the performance compared with complete, lossless spectrum signal.

2. THE ToF ESTIMATION

We have located three ToF estimation techniques [8,9,10]: the direct correlation maximization (DCM), the L2 norm minimization (L2M) and the L1 norm minimization (L1M). The DCM technique is using the position of peak value of cross-correlation function R_{DC} for signal arrival position (so the ToF) estimate:

$$ToF_{DC} = \arg[\max R_{DC}(\tau)], \quad (1)$$

where R_{DC} is:

$$R_{DC}(\tau) = \int_{-\infty}^{\infty} s_T(t) \cdot s_R(t - \tau) dt. \quad (2)$$

The L2M is using the minima of position of L2-norm of received signal and reference signal subtraction:

$$ToF_{L2} = \arg\{\min[L2(\tau)]\}, \quad (3)$$

where $L2$ is:

$$L2(\tau) = \int_{-\infty}^{\infty} [s_R(t) - s_T(t - \tau)]^2 dt. \quad (4)$$

The L1M uses the average magnitude difference function of received signal and reference signal:

$$ToF_{L1} = \arg\{\min[L1(\tau)]\}, \quad (5)$$

where $L1$ is:

$$L1(\tau) = \int_{-\infty}^{\infty} |s_R(t) - s_T(t - \tau)| dt. \quad (6)$$

The direct correlation technique theoretical analysis on ToF estimation variance is broad [2,3,8-14]. Therefore it has been chosen for this analysis.

As suggested in [11] and [12] the ToF estimation can be done by the direct correlation maximization to find and estimate of the true position of signal arrival. The variance of ToF standard deviation is [7]:

$$std_{CRLB}(TOF) \geq \frac{1}{2\pi F_e \sqrt{\frac{2E}{N_0}}}, \quad (7)$$

where E is signal $s(t)$ energy, F_e is effective bandwidth of the signal. The effective signal bandwidth can be calculated as:

$$F_e^2 = \beta^2 + f_0^2, \quad (8)$$

where β is the envelope bandwidth and f_0 is the center frequency:

$$\beta^2 = \frac{\int_{-\infty}^{\infty} (f - f_0)^2 |S(f)|^2 df}{E}, \quad f_0^2 = \frac{\left[\int_{-\infty}^{\infty} f |S(f)|^2 df \right]^2}{E^2}. \quad (9)$$

The envelope bandwidth β is also defining the resolution because it is directly related to the signal duration after its compression in matched filter.

3. SPECTRUM SPREAD

As (7) suggests, the reduction of random errors is possible by maximizing the signal energy, reducing the noise level and increasing the effective signal bandwidth. Once noise level has some physical limit it is more feasible to increase the energy and the bandwidth. If spread spectrum signals are used, both long duration and wide bandwidth are achieved.

But use of wideband excitation signals is limited by multi-band losses, usually occurring in imaging or navigation systems. The ultra-wideband (UWB) radar should avoid certain bands; also there is a particle absorption in the propagation media (ground penetrating radar) or atmosphere. This creates multi-band losses. Similar losses exist in ultrasonic NDT: when layered ultrasound composites are inspected, those possess certain multiple positive and negative resonances due to wave interaction between the layers. Same can be addressed to fiber composite materials [18,19]. Also, in case of multi-transducer measurements some frequency regions might not be covered.

Multi-band losses in radar, sonar or ultrasonic NDT can create "rake" type signal. Instead of avoiding of wideband signal use, we want to exploit its advantages and apply on channel with multi-band losses. First, possible spectral spread techniques have to be investigated.

Several techniques can be applied to spread the signal spectrum: phase manipulated pseudo-noise sequences [6,7,15], chirp [4,16] and arbitrary waveform excitation [17].

Phase manipulated sequences (Figure 1) make the excitation task easier since square waves can be used for signal generation: the hardware is less complex because power amplifier is replaced with high speed switch.

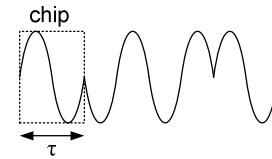


Fig. 1. Phase manipulated sequence

Application of the orthogonal coded sequences allows to easily separate the probing channels [15] so simultaneous surrounding area scanning with several ranging channels can be done.

The problem is that the resulting signal bandwidth is predicted by the smallest chip (Figure 1) duration. If integer number of half-periods must be used for chip this is a disadvantage since then the bandwidth adjustment step is discrete. Another disadvantage is that it's impossible to shape the signal spectrum in the arbitrary way.

Application of the arbitrary waveform produces any shape of amplitude and phasing spectrum and correlation function [15]. But this technique requires complicated excitation hardware. There are attempts to use some approximation using only limited number or excitation levels: in [7] a quinary excitation method is reported for linear frequency modulation windowing implementation.

A frequency spreading using a carrier frequency modulation [4,16] frequently is addressed as chirp signal (Figure 2).

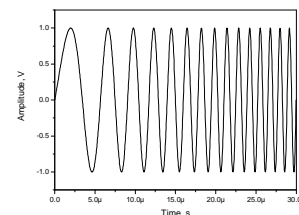


Fig. 2. Chirp signal

We suggest using chirp signals for excitation. Chirp signal excitation offers any spectral shape and easy excitation circuit and looks an attractive solution: in [2] the combination of chirp signals and wideband micromachined capacitance (CMUT) transducers application in air-coupled ultrasound is reported; in [4] a nonlinear frequency modulation of square wave signal is used in order to match the signal spectrum to ultrasonic transducer spectral response shape; in [16] chirp spectrum is wider than transducer bandwidth.

If nonlinear chirp signals are used, this would allow skipping the loss-bands and still using wide-band inspection.

4. NUMERICAL EXPERIMENT

Here we aimed to investigate correlation properties of signals with multi-band losses. Linear frequency modulation chirp was produced and signal passed through rake filter (Figure 3). Rake filter was constructed by using serially connected elliptical notch filters. Resulting signal with multi-band losses we assume to use for excitation. Therefore this signal was used for analysis.

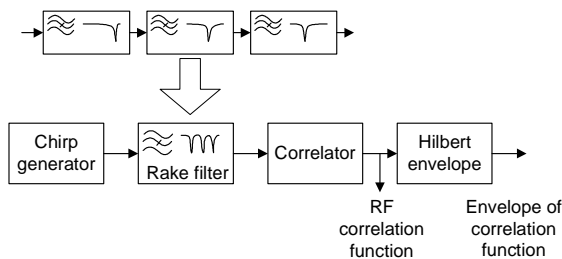


Fig. 3. Experiment diagram

The effective bandwidth F_e , envelope bandwidth β and the center frequency f_0 were calculated using discrete case of the equations (7), (8) and (9) presented in [3]. Signal with multi-band losses was used for autocorrelation function calculation. This function was treated as RF correlation function. The RF (before envelope extraction) autocorrelation function central lobe width at zero crossing level was measured and noted as τ_0 . It should correspond to $2/f_0$. The autocorrelation function envelope was calculated using Hilbert transform and central lobe width at -6dB level was obtained. It should correspond to envelope bandwidth as $1/\beta$.

Four types of investigations have been carried out: i) when total stopband width was held constant, minimum and maximum frequencies were kept constant, but number of rake tooth varied; ii) when

stopband width was varied, minimum and maximum frequencies and rake tooth number were kept constant; iii) same as above, but with single tooth; iv) when stopband was constant, but stopband tooth position in frequency domain varied.

4.1. Constant total bandwidth but variable tooth number

The aim of this investigation was to decide how the shape of the frequency response affects the correlation function. Number of notch tooth was varied, start and stop frequencies remained the same (Figure 4) in such way that and the center frequency f_0 was not affected.

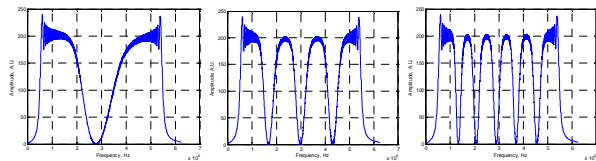


Fig. 4. Spectrum for variable tooth number, const. f_0

As expected, since f_0 was fixed there was no variation in RF correlation function central lobe width (Figure 5). There was a variation in sidelobes level: for tooth number above one in rake filter sidelobes were at acceptable level.

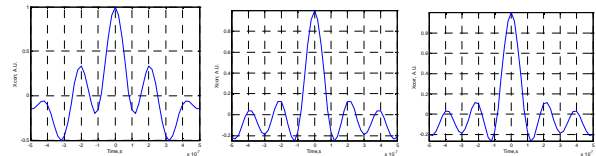


Fig. 5. RF correlation function for variable tooth number, const. f_0

Almost the same result was noted on envelope: for the case of single tooth envelope's mainlobe width was narrower than for multiple tooth. This can be explained by larger amount of energy being deviated from f_0 so the resulting increase of β (Fig. 6).

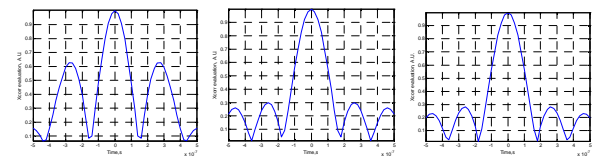


Fig. 6. Correlation function envelope for variable tooth number, const. f_0

4.2. Constant start and stop frequencies, center frequency and tooth number but variable bandwidth

The aim of this investigation was to check whether larger amount of energy being deviated from f_0 is resulting in increase of envelope bandwidth β . There was only one notch tooth but bandwidth was varied, start and stop frequencies remained the same (Figure 7) in such way that and the center frequency f_0 was not affected.

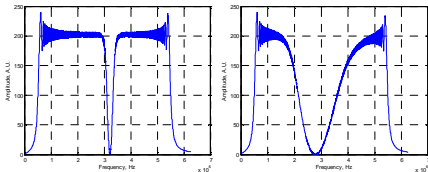


Fig. 7. Spectrum for variable bandwidth, const. f_0 and tooth number

Results confirmed the assumption: despite increase of stopband, envelope bandwidth was increasing (bottom grey line in Figure 8)

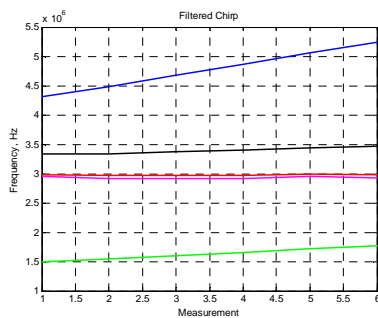


Fig. 8. Envelope bandwidth β , effective bandwidth F_e , and center f_0

4.3. Constant start and stop frequencies and tooth number but variable bandwidth

The aim of this investigation was to decide how the amount of stopband affects the correlation function. Number of notch tooth was kept constant but stopband increased, start and stop frequencies remained the same so that center frequency f_0 was not affected (Figure 9).

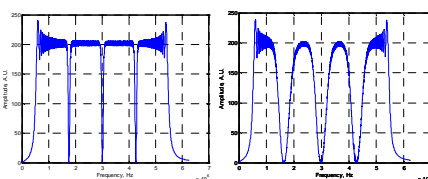


Fig. 9. Spectrum for variable stopband, const. f_0 and tooth number

As expected, since f_0 was fixed there was no variation in RF correlation function central lobe width (Figure 10). Odd result was noted on envelope: envelope's mainlobe width was narrower for larger stopband (Figure 11).

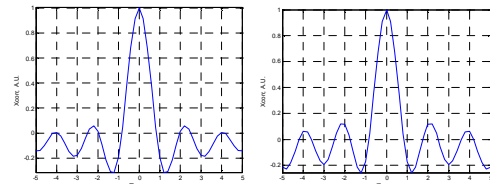


Fig. 10. RF correlation function for variable stopband, const. f_0 and tooth

This can be explained by shorter signal in time, resulting in shorter effective duration, since after passing the chirp through rake filter the corresponding positions in time are attenuated.

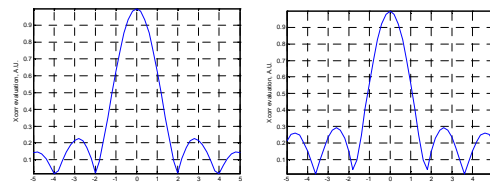


Fig. 11. Correlation function envelope vs. stopband, const. f_0

4.4. Constant start and stop frequencies and tooth number but variable tooth position

The aim of this investigation was to decide how the center frequency f_0 variation affects the correlation function. Number of notch tooth, envelope bandwidth β and stopband was kept constant, start and stop frequencies remained the same but tooth position was varied in such way that and the center frequency f_0 was affected (Figure 12).

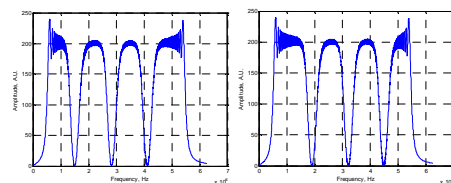


Fig. 12. Spectrum for variable f_0 , const. stopband, β and tooth number

As expected, since f_0 was varied, there was similar variation in RF correlation function central lobe width. The rest of function remained unaffected: envelope mainlobe, sidelobes varied very slightly.

6. CONCLUSIONS

Multi-band losses in radar, sonar or ultrasonic NDT create "rake" type media filter. Chirp signal posses the ability to easily modify the excitation signals spectrum and energy. Application of such signals would allow skipping the lossy bands and still using wideband inspection in order to get high resolution.

ToF measurement and resolution related properties have been investigated. Experiments show that even significant losses within "rake" allow maintaining essential wideband properties of the signal. A multi-band loss ("rake") is affecting the sidelobes, but mainlobe performance remains and in some cases is even improved.

References

- [1] R. J. Kazys, L. Svilainis, "Ultrasonic detection and characterization of delaminations in thin composite plates using signal processing techniques", *Ultrasonics*, vol. 35(5), 1997, p.p. 367—383.
- [2] T. H. Gan, D. A. Hutchins, D. R. Billson, D. W. Schindel, "The use of broadband acoustic transducers and pulse-compression techniques for air-coupled ultrasonic imaging", *Ultrasonics*, vol.39(3), 2001, p.p.181-194.
- [3] L. Svilainis, V. Dumbrava, "The time-of-flight estimation accuracy versus digitization parameters", *Ultragarsas*, vol.63(1), 2008, p.p.12-17.
- [4] M. Pollakowski, H. Ermert, "Chirp signal matching and signal power optimization in pulse-echo mode ultrasonic nondestructive testing", *IEEE trans. UFFC*, vol. 41(5), 1994, p.p.655-659.
- [5] S. Lonne, A. Lhemery, et al, "Modeling of Ultrasonic Attenuation in Uni-Directional Fiber Reinforced Composites Combining Multiple-Scattering and Viscoelastic Losses", *Proc.QNDE AIP*, vol.700, 2004, pp. 875-882.
- [6] A. Nowicki, I. Trots, P. A. Lewin, et. al. "Influence of the ultrasound transducer bandwidth on selection of the complementary Golay bit code length", *Ultrasonics*, vol. 47, 2007, p.p.64-73.
- [7] D. M. J. Cowell, S. Freear, "Quinary excitation method for pulse compression ultrasound measurements", *Ultrasonics*, vol.48(2), 2008, p.p.98-108.
- [8] G. C. Carter (editor). "Special issue on time delay estimation", *IEEE Trans. Acoust. Speech Signal Proc.*, vol. 29. 1981.
- [9] M. Parrilla, J. J. Anaya, C. Fritsch, "Digital Signal Processing Techniques for High Accuracy Ultrasonic Range Measurements", *IEEE Trans. Instrumentation and Measurement*, vol. 40(4), 1991, p.p. 759-763.
- [10] G. Jacovitti, G. Scarano, "Discrete Time Techniques for Time Delay Estimation", *IEEE Transactions on signal processing*, vol. 41(2), 1993, p.p.525-533.
- [11] C. Rao "Information and the accuracy attainable in the estimation of statistical parameters", *Bulletin of Calcutta Mathematics Society*, vol. 37, 1945, p.p. 81–89.
- [12] H. Cramer "Mathematical Methods of Statistics". Princeton Univ. Press. 1946.
- [13] R. Queiros, et.al. "Cross-Correlation and Sine-Fitting Techniques for High Resolution Ultrasonic Ranging", *proc. IMTC, Sorento*. 2006. p.p. 552-556.
- [14] A.H. "Quazi An Overview on the Time Delay Estimate in Active and Passive Systems for Target Localization", *IEEE Trans. ASSP*, vol. 29(3), 1981, p.p.527-533.
- [15] R. J. Kazys, L. Svilainis, L. Mazeika "Application of orthogonal ultrasonic signals and binaural processing for imaging of the environment", *Ultrasonics*, vol.38, 2000,p.p. 171-175.
- [16] L. Svilainis, G. Motiejūnas, "Spread spectrum signal performance investigation in a bandlimited channel", *Ultragarsas*, vol.63(4), 2008, p.p. 30-34.
- [17] J. Salazar, A. Turo, et al. "Deconvolution problem to produce ultrasonic short pulses", *IEE Proc. Science, Measurement and Technology*, vol.145(6), 1998, p.p. 317-320.
- [18] M. Torres, F. R. Montero de Espinosa, "Ultrasonic band gaps and negative refraction", *Ultrasonics*, vol.42, 2004, p.p. 787-790.
- [19] S. Banerjee, F. Riccib, et al. "A wave propagation and vibration-based approach for damage identification in structural components", *Journal of Sound and Vibration*, vol. 322(1-2), 2009, p.p.167-183.

ANALYSIS OF COMPLEX IMPEDANCE MEASUREMENT I-V METHOD

A. Chaziachmetovas, V. Dzenkauskas

Signal processing department, Kaunas University of Technology
Studentu str. 50, LT-51368 Kaunas, Lithuania

T, +370 37 300527; F, +370 37 753998; E, andrius.chaziachmetovas@ktu.lt / vaidotas.dzenkauskas@ktu.lt

Abstract

Complex impedance measurement methods are widely described, but the information on what the uncertainty of the measurement in case of complex result is scarce.

In this article we will investigate two techniques of I-V method: the I-V differential and I-V single ended. Both of them are based on "voltage divider". Complex value measurement uncertainty analysis is presented based on theoretical measurement setup analysis and complex sensitivity functions. Real and imaginary uncertainty components are presented in complex impedance plane.

1. INTRODUCTION

The complex circuit impedance is widely used in electromagnetic and ultrasound applications. Impedance variation over frequency range is receiving greater attention nowadays. Because of wideband nature of measurements, impedance is varying in wide range. In addition, impedance variance is in complex plane. Usually it is undesirable to have jumps in impedance measurements (in case of hysteretic analysis or nonlinear circuits). Therefore it is important to have a technique, capable to obtain the impedance without changing the reference impedance (reference impedance switching will cause current and voltage variation in investigated circuit). When complex values are measured, the uncertainty estimation becomes complex too.

Here we aim to analyze the measurement uncertainties of I-V method when it is used for complex impedance measurements.

2. I-V IMPEDANCE MEASUREMENT

The unknown impedance Z_x can be obtained from the measured values of voltage and current. When voltage and current are obtained directly then technique is named I-V [1]. The measurement can be arranged using two techniques: the I-V differential and I-V single ended. The simplified connection diagram of the I-V *differential* technique is presented in Figure 1.

Current is calculated using the voltage measurement across an accurately known resistor, R_{ref} .

$$Z_x = \frac{U_{Zx}}{I} = \frac{U_{Zx}}{U_{Rref}} R_{ref}. \quad (1)$$

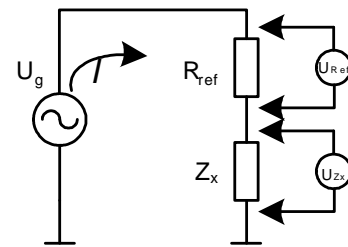


Fig. 1. Differential I-V technique

The *single-ended* technique is using only single-ended measurement channels. The implementation diagram for single-ended technique is presented in Figure 2.

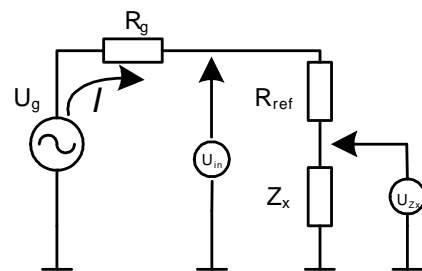


Fig. 2. Single ended I-V technique

The R_{ref} voltage dropout is obtained by voltages U_{Zx} and U_{in} subtraction:

$$Z_x = \frac{U_{Zx}}{U_{in} - U_{Zx}} R_{ref}. \quad (2)$$

The analysis below is based on circuits presented.

3. THE SENSITIVITY COEFFICIENTS

Uncertainty analysis was done to estimate the presented techniques' performance. Assuming that

impedance is measured using indirect method, for uncorrelated input quantities the combined standard uncertainty $u_c(Z_x)$ is a squares sum of corresponding uncertainties $u_i(Z_x)$ [2]:

$$u_c(Z_x) = \sqrt{\sum_{i=1}^n u_i(Z_x)^2} = \sqrt{\sum_{i=1}^n c_i^2 u(x_i)^2}. \quad (3)$$

The quantity $u_i(Z_x)$ is the contribution to the standard uncertainty associated with the output estimate Z_x associated with i -th the input estimate x_i . Then the i -th sensitivity coefficient c_i of the corresponding input estimate x_i is the partial derivative of the measurement function f with respect to x_i

$$c_i = \frac{\partial Z_x}{\partial x_i} = \frac{\partial [f(x_1, x_2, x_3, \dots, x_i)]}{\partial x_i}. \quad (4)$$

So, a single-ended I-V technique Z_x according to equation (2) is a function of U_{Zx} , U_{in} and R_{ref} accordingly. The sensitivity coefficients for those variables can be obtained as [3]:

$$c_{U_{Zx}} = \frac{R_{ref}}{U_{in} - U_{Zx}} + \frac{U_{Zx} R_{ref}}{(U_{in} - U_{Zx})^2}, \quad (5)$$

$$c_{U_{in}} = -\frac{U_{Zx} U_{Rref}}{(U_{in} - U_{Zx})^2}, \quad (6)$$

$$c_{R_{ref}} = \frac{U_{Zx}}{U_{in} - U_{Zx}}. \quad (7)$$

And the absolute combined standard uncertainty of Z_x [4]:

$$u_c(Z_x) = \sqrt{u^2(U_{Zx}) \left(\frac{R_{ref}}{U_{in} - U_{Zx}} + \frac{U_{Zx} R_{ref}}{(U_{in} - U_{Zx})^2} \right)^2 + u^2(U_{in}) \left(\frac{U_{Zx} R_{ref}}{(U_{in} - U_{Zx})^2} \right)^2 + u^2(R_{ref}) \frac{U_{Zx}^2}{(U_{in} - U_{Zx})^2}}, \quad (8)$$

where $u(U_{Zx})$, $u(U_{in})$ and $u(R_{ref})$ are corresponding components' absolute uncertainties.

4. UNCERTAINTY ANALYSIS

For performance evaluation the relative uncertainty of impedance Z_x was used:

$$u_{\%}(Z_x) = \frac{u_c(Z_x)}{|Z_x|} \cdot 100\%, \quad (9)$$

Equation (8), together with voltage measurement standard uncertainty and resistor accuracy have been used. Applying equation (8) for equation (9) gives the percentage relative uncertainty for impedance measurement when I-V impedance measurement using single-ended implementation is used

$$u_{\%}(Z_x) = \frac{\frac{U_{in} - U_{Zx}}{U_{Zx} R_{ref}} \sqrt{u^2(U_{Zx}) \left(\frac{R_{ref}}{U_{in} - U_{Zx}} + \frac{U_{Zx} R_{ref}}{(U_{in} - U_{Zx})^2} \right)^2} + u^2(U_{in}) \left(\frac{U_{Zx} R_{ref}}{(U_{in} - U_{Zx})^2} \right)^2 + u^2(R_{ref}) \frac{U_{Zx}^2}{(U_{in} - U_{Zx})^2}}{\sqrt{u^2(U_{in}) \left(\frac{U_{Zx} R_{ref}}{(U_{in} - U_{Zx})^2} \right)^2 + u^2(R_{ref}) \frac{U_{Zx}^2}{(U_{in} - U_{Zx})^2}}} \cdot 100\% \quad (10)$$

Voltage measurement uncertainty required for equation (8) and (10) was obtained from experimental results presented in [4], since similar system is planned for the measurements. The input voltage U_{in} has been assumed of 1 V value, reference resistor R_{ref} was assigned 10Ω value. The variation for unknown impedance was given the variance range as the fraction of reference resistor R_{ref} . The resulting voltages and currents were used to obtain final value of measurement uncertainty. Real and imaginary parts (Figure 3) were treated separately, giving the variance in corresponding range.

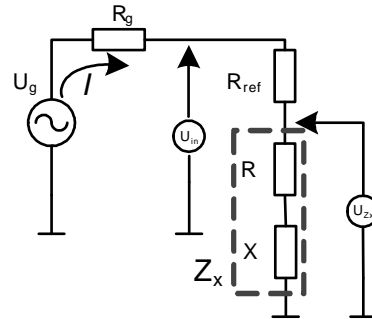


Fig. 3. Z_x complex measurement using single-ended implementation

If variables in equation (10) are complex, the resulting uncertainty will be complex too. In order to analyse the uncertainties, three ways were chosen: absolute value:

$$u_{abs\%}(Z_x) = |u_{\%}(Z_x)|, \quad (11)$$

and real and imaginary parts:

$$u_{RE\%}(Z_x) = \Re(u_{\%}(Z_x)), u_{IM\%}(Z_x) = \Im(u_{\%}(Z_x)), \quad (12)$$

The uncertainty absolute value is presented in Figure 4.

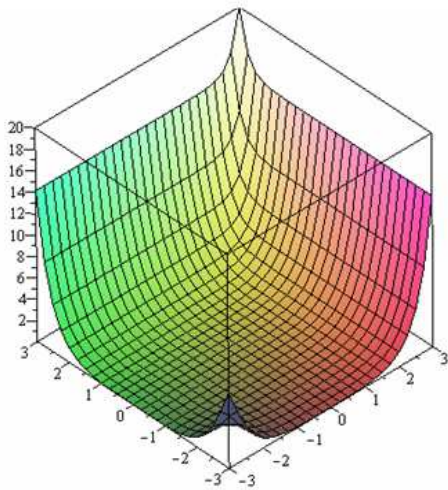


Fig. 4. Relative standard uncertainty of Zx complex measurement influence of $u\%(R_{ref})$

Wide range (x1000 times above and below the R_{ref}) for variance was given. Real and imaginary parts and uncertainty value itself produce the 3-dimensional space. Contour plot might be more convenient (Figure 5).

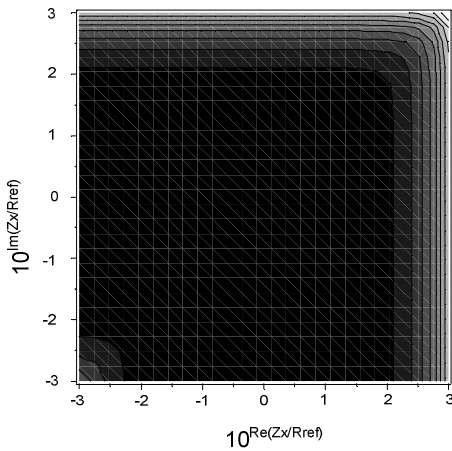


Fig. 5. Contour plot of absolute value of relative standard uncertainty

It can be seen that there is significant area of flat plateau in measurement uncertainties, and only when approaching ratios of 1000 times random errors become significant.

When analyzing in details (Figure 6, x10 times) it can be noted that there is a insignificant local minima, located at $1.6 \times R_{ref}$. It depends on reference resistor accuracy.

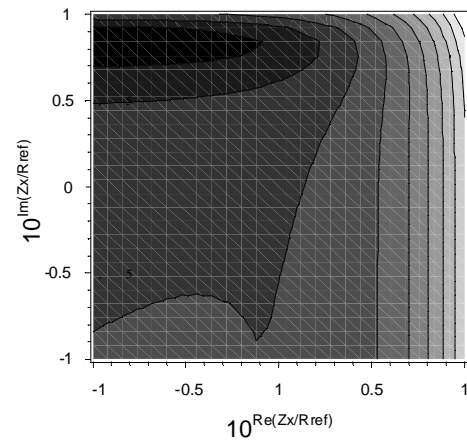
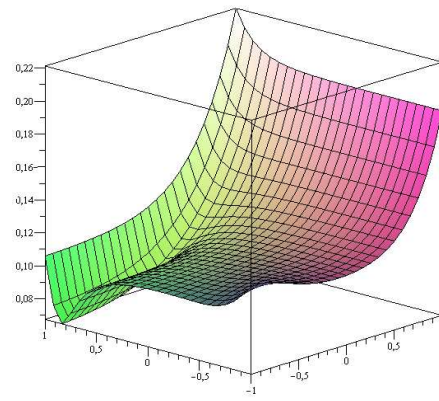


Fig. 6. 3D plot and contour plot of absolute value of relative standard uncertainty for smaller range

Theoretically uncertainty of 0,2% can be reached, if 0.1% uncertainty reference resistor is used.

Real (Figure 7) and imaginary (Figure 8) parts for the same analysis are presented.

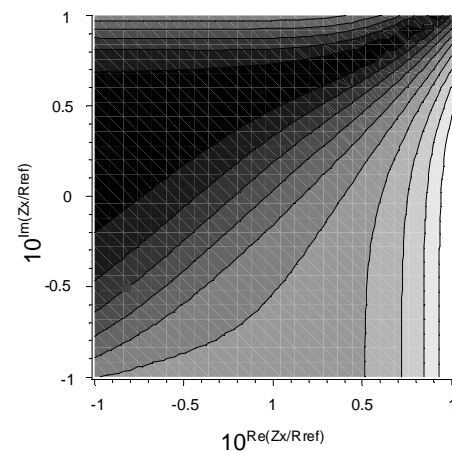


Fig. 7. Contour plot of real value of relative standard uncertainty for smaller range

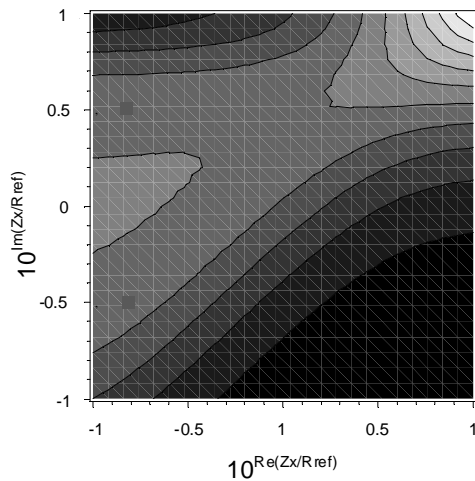


Fig. 8. Contour plot of imaginary value of relative standard uncertainty for smaller range

It can be seen that real part of uncertainty varies along real impedance axis and imaginary part varies along imaginary axis correspondingly.

5. ACKNOWLEDGMENTS

We would like to thank the Dr. Vytautas Dumbrava and Dr. Linas Svilainis for their consultations and useful literature on uncertainty analysis support.

6. CONCLUSIONS

The analysis uncertainties of complex impedance measurement estimation were presented.

It has been shown that both real and imaginary parts of uncertainty exist which define the optimal range for the technique application.

References

- [1] "Impedance Measurement Handbook". *Agilent Technologies*. USA. 2003.
- [2] "Expression of the Uncertainty of Measurement in Calibration", EA-4/02, *European cooperation for accreditation*, 1999.
- [3] L. Svilainis, V. Dumbrava. "Amplitude and phase measurement in acquisition systems", *Matavimai*, vol. 38(2). 2006, p.p. 21-25.
- [4] V. Dumbrava, L. Svilainis. "Uncertainty analysis of I-V impedance measurement technique", *Matavimai*, vol. 41(1), 2008, p.p. 9-14.

METHOD SELECTION AND ERROR EVALUATION FOR FAULT PLACE DETECTION IN UNDERGROUND HEAT DISTRIBUTION PIPES

V. Dzenkauskas, A. Chaziachmetovas

Signal processing department, Kaunas University of Technology
Studentu str. 50, LT-51368 Kaunas, Lithuania

T, +370 37 300534; F, +370 37 753998; E, vaidotas.dzenkauskas@ktu.lt / andrius.chaziachmetovas@ktu.lt

Abstract

The fault location technique for modern hot water transportation pipes used for hot water transfer was suggested. It is an alternative to time domain reflectometry measurements usually used in such type of task. Technique is capable of locating the fault place by using the measured EM field strength outside the pipe. The location of the pipe end using just peak of the emissions level is complicated. Therefore modified measurements procedure was suggested which is using two linear regression curves approximating the fields strength before the fault and after fault. Those curves interception point is the estimate of the fault position.

The position estimation example for the pipe buried at 1.2m depth was given. The resulting fault location estimation error was presented. It can be seen, that while digging the ground out and getting closer readings, less than 5cm location error is possible.

1. INTRODUCTION

Quality of water supply pipelines is of great importance: shortage of fresh water leads even to tension between the countries [1-3]. In particular, our interest lies in water transportation pipes. Corrosion, pressure differences lead to ruptures of pipes creating a water leak. Even a small leak might cause a lot of water to be lost. For example, in Chicago leak-related losses make 40 % [4].

Modern pipes [5] used for hot water transfer are encased in external cover from high density polyethylene and inner space is filled with plastic foam for a thermal insulation.

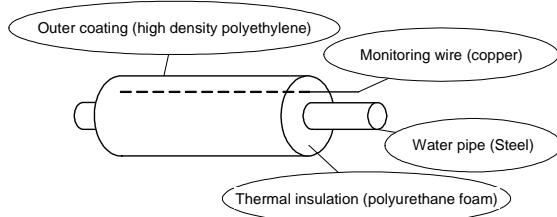


Fig. 1. Modern water pipe design

For inspection and monitoring purposes, wires are placed inside the thermal protection foam. Those wires together with a metal pipe represent a two-wire asymmetric transmission line which is used for definition of damage of a pipe at even weak leak of water. Impedance measurement is used for leakage event detection and time domain reflectometry (TDR) is used for leak location [6]: wet

foam is disrupting the transmission line impedance, so reflection occurs at leakage point.

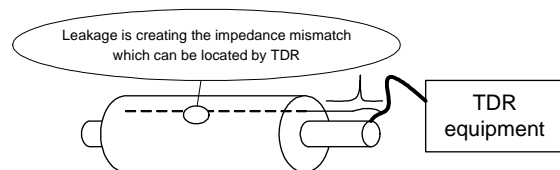


Fig. 2. Leakage location by TDR

Unfortunately, TDR location is prone to location errors due to reflection at the [4,7,8] closest point of fault and propagation speed estimation errors.

We are suggesting an alternative fault location technique, capable of locating the fault place by doing the electromagnetic (EM) field strength measurements outside the pipe.

2. FAULT LOCATION PRINCIPLE

The transmission line has losses; in particular caused by electromagnetic field radiation outside (outer conductor for shielding does not exist). We have decided to try to define the amount of this radiation and to try to use this effect for location of a damage place (Figure 3).

Arrangement of the radiated EM field measurement of the matched transmission line-type pipe is presented on Figure 4.

Termination was placed at the open pipe end. The outer shell diameter of the pipe used was 200 mm, inner steel pipe diameter was 50 mm. Pipe length was 3m. Pipe was hung in the labora-

tory to keep away from metal objects at least by 500mm. The RF generator injected the 50MHz 10Vp-p signal into the opposite end of the pipe. EM field strength was measured using whip antennae (500 mm length), level was registered using Thurbly Thundar Instruments PSA1301T spectrum analyzer. Measurements were taken at antennae located across the pipe direction. Measurement results are presented on Figure 5.

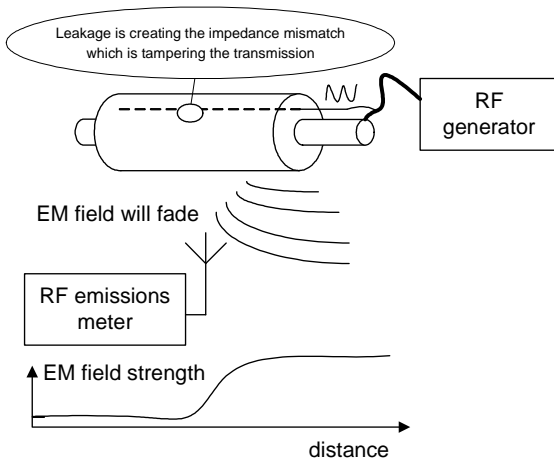


Fig. 3. Suggested location principle

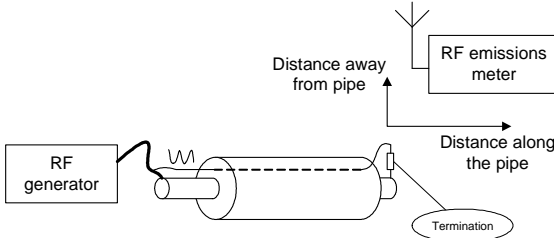


Fig. 4. Radiated EM fields measurement setup

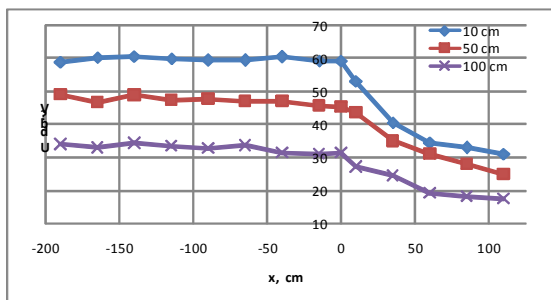


Fig. 5. Radiated 50MHz EM fields vs. distance from terminated end

It can be seen, that due to proper termination there is a radiated EM field decay in the area beyond the pipe. Experiment was carried out with transmission line being not terminated. Broken pipe case was simulated. Radiated EM fields measure-

ment of the mismatched (open ended) transmission line is presented on Figure 6 and Figure 7.

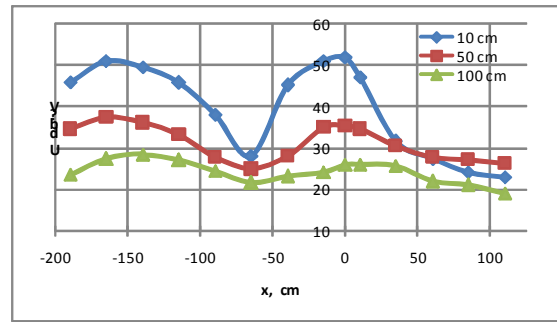


Fig. 6. Radiated 50MHz EM fields vs. distance from unterminated end

It can be seen, that due to standing waves location of fault place is complicated. Experiment was carried out at 50MHz (Fig. 6) and 10MHz (Fig. 7).

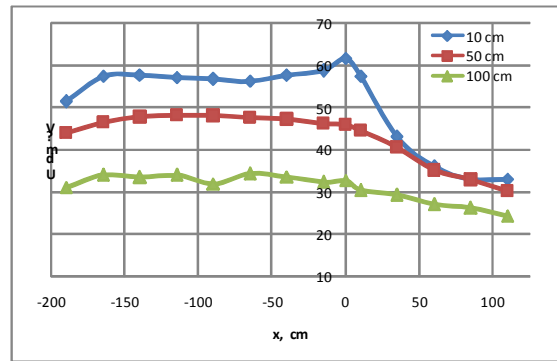


Fig. 7. Radiated 10MHz EM fields vs. distance from unterminated end

Such frequency was chosen intentionally, since suggested method should locate the buried pipe: higher frequencies will be largely attenuated in soil [8]. Using lower frequencies will give larger distance between standing waves and the accuracy or the measurement will be decreased.

Experiments were carried out on pipe buried 1,2m in soil (Figure 8). The pipe end was left open (unterminated case), polyethylene cap was applied on the open end. Pipe was buried in wet clay.

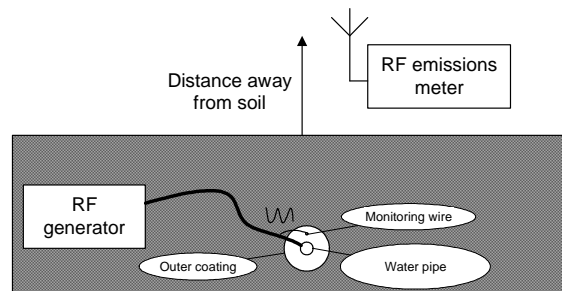


Fig. 8. Buried pipe radiated EM field above the soil @10MHz

Radiated EM fields measurements of the open ended transmission line at 10MHz frequency are presented on Figure 9.

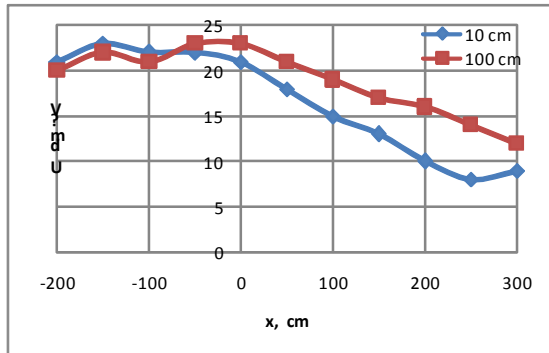


Fig. 9. Radiated 10MHz EM fields vs. distance from buried pipe @10MHz

It can be seen that there are two curves prevailing: standing wave profile created field along the pipe with transmission line and decaying EM field at the end of the pipe. The location of the pipe end using peak of the emission is complicated. Therefore modified measurements procedure was suggested.

3. THE MODIFIED PROCEDURE

We suggest using two linear regression curves approximating the aforementioned fields' strength. Left hand side (standing wave profile along the pipe with transmission line):

$$y_1 = a_1x + b_1 \tag{1}$$

And the right – hand side curve (field along the pipe without transmission line):

$$y_2 = a_2x + b_2 \tag{2}$$

Then curves interception point can be determined by equating (1) to (2):

$$a_1x + b_1 = a_2x + b_2 \tag{3}$$

The solution x for the equation (3) is the estimate of the fault position:

$$x = \frac{b_2 - b_1}{a_1 - a_2} \tag{4}$$

Equation (4) was used on Figure 8 and Figure 9 data to locate the fault position (Figure 10).

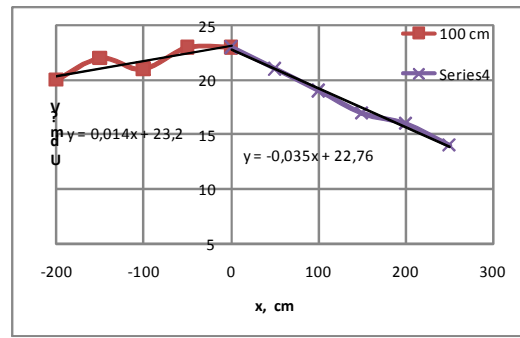


Fig. 10. Radiated 10MHz EM fields vs. distance from buried pipe @10MHz

Coefficients used and error obtained are presented in Table 1.

Table 1. Fault position estimation data

Away from soil, cm	a ₁	b ₁	a ₂	b ₂	Δx, cm
10	0,015	59,6	-0,4	60,6	2,16
50	0,004	47,2	-0,16	45,9	7,39
100	0,002	33,3	-0,07	31,8	19,44
120	-0,002	21,6	-0,05	20,7	18,80

The resulting fault location estimation error is presented in Figure 11.

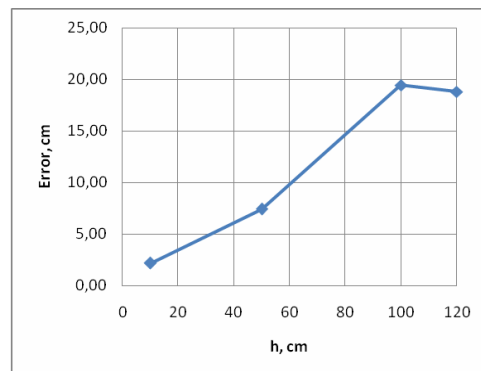


Fig. 11. Buried pipe fault location error vs. distance from soil @10MHz

4. CONCLUSIONS

A TDR alternative fault location technique for modern hot water transportation pipes by using the measured EM field strength outside the pipe was suggested. It has been shown that the location of the pipe end using just peak of the emissions level is complicated. Therefore modified measurements procedure using two linear regression curves approximating the fields' strength before the fault and after fault was suggested.

The position estimation example for the pipe buried at 1.2m depth given suggests that the resulting fault location estimation error can be less than 5cm.

References

- [1] „ICE Case Studies, Case Identifier: TIGRIS“ *Tevfik Emin Kor*, 1997 [online 2009-09-15]: <http://www1.american.edu/TED/ice/tigris.htm>
- [2] “Water, Crisis and War”, *Zee News Limited*, [online 2009-09-15]: <http://www.zeenews.com/sci-tech/eco-news/2009-03-22/516904news.html>
- [3] R. Bleier, “Israel's Appropriation of Arab Water: An Obstacle to Peace”, *Middle East Labor Bulletin*, Spring 1994, [online 2009-09-15]: <http://desip.igc.org/TheftOfWater.html>
- [4] “Water loss and other information” *Tullmin Consulting* [online 2009-09-15]: <http://www.corrosion-club.com/waterfigures.htm>
- [5] M. Eiswirth, L. S. Burn, “New methods for defect diagnosis of water pipelines”, –proc. *Water pipeline systems*, 2001, York, UK
- [6] “Time domain reflectometry theory”, *Hewlett-packard application note* 1304-2, 1988
- [7] D. J. Daniels, “Surface-penetrating radar”, *Electronics & Communication Engineering Journal*, 1996-08
- [8] J. O. Curtis, “Microwave Behaviour of Soils”, Report 3, Environmental Laboratory, Vicksburg, USA 1993

USING LIGHTWEIGHT DIRECTORY ACCESS PROTOCOL FOR SERVICE LEVEL SPECIFICATIONS ADMINISTRATION

Valentin Hristov

South- West University- Blagoevgrad, Bulgaria
T.+359738889131; E. v_hristov@swu.bg

Abstract

A directory service is a simplified database. The Lightweight Directory Access Protocol is a distributed directory service protocol, and is based on a client-server model and runs over TCP/IP. The LDAP allows to configure networks for supporting different levels of services.

The purpose of present paper is to propose a modified schema for supporting Service Level Specifications based on LDAP directories, and study its performance under variety of access patterns.

1. INTRODUCTION

The Lightweight Directory Access Protocol (LDAP) was originally intended to be a lightweight alternative protocol for accessing X.500 directory services through the widespread TCP/IP protocol stack. This model of directory access was borrowed from the DIXIE and Directory Assistance Service protocols.

LDAP is an application protocol for querying and modifying directory services running over TCP/IP [1]. A LDAP directory is a set of objects with similar attributes organised in a logical and hierarchical manner, i.e. the directory is a tree of directory entries. Each entry has a unique identifier, i.e. its Distinguished Name (DN). This consists of its Relative Distinguished Name (RDN) constructed from some attribute(s) in the entry, followed by the parent entry's DN. An attribute has a name (an attribute type or attribute description) and one or more values.

A client starts an LDAP session by connecting to an LDAP server. After that it sends an operation request to the server, and the server sends responses in turn. With some exceptions, the client need not wait for a response before sending the next request, and the server may send the responses in any order.

LDAP defines operations for querying and updating the directory. Operations are provided for adding and deleting an entry from the directory, changing an existing entry, and changing the name of an entry. Most of the time, LDAP is used to search for information in the directory.

The LDAP search operation allows some portion of the directory to be searched for entries that

match some criteria specified by a search filter. Information can be requested from each entry that matches the criteria.

The current Internet operates on a best-effort basis, in which all packets are treated equally. Thus, the improvement of network service models with mechanisms to provide multiple service levels to users is actual problem. Researchers in the DiffServ community have proposed storing these policies in a central or distributed policy repository administered and accessed using a directory service such as LDAP [3], [4]. In this scenario, the policy repository is updated when the network provider negotiates new Service Level Specifications, or renegotiates existing contracts, and also when the policies need to reflect changes in network topology or traffic levels. Network elements frequently access the policy database, and download the current set of rules according to which customer traffic is served.

The purpose of present paper is to propose a modified schema for the administration of Service Level Specifications (SLS) based on LDAP directories, and study its performance under variety of access patterns.

2. SCHEMA FOR SUPPORTING SERVICE LEVEL SPECIFICATIONS

Recently, there has been much interest in network service models with mechanisms to provide multiple service levels to users. The two main approaches under discussion are the integrated service model, which supports quality of service (QoS) levels by allowing per-flow resource reservation

using RSVP signaling, and the differentiated service model, which provides multiple service classes which are served using different per-hop behaviors. In either model, the network provider negotiates a service level specification with a customer, defining aspects of network behavior such as the type of service user packets will receive, and the constraints the user traffic must adhere to. The Service Level Specification (SLS) may be dynamically renegotiated, based on changes in the customer requirements or network conditions. The network access points and internal routers implement the classification, resource control, and administrative policies associated with SLSs.

In fig. 1 is depicted Generic SLA Architecture [6]. The Domain Manager (DM) generally manages the network domain. It communicates with the policy server that administrates policies, rules and actions for different services stored in a policy repository. In addition, the network provider provisions the network in order to provide the service contracted to customers. The provisioning is physical (adding or removing network elements) and logical (partitioning or configuring network elements).

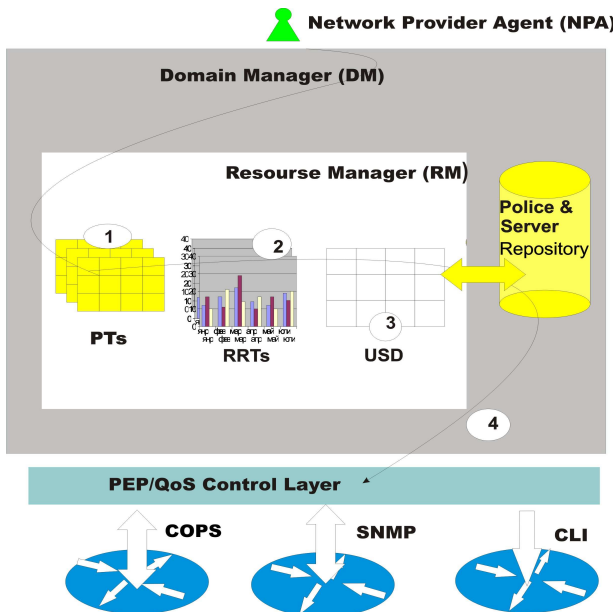


Fig. 1

The network configuration information may be maintained in LDAP directories, and downloaded periodically by routers. This allows the network provider to adjust configurations (for example, buffer space, or packet drop precedences) with a finer granularity in response to network usage feedback.

The architecture based on first approach provides immediate bandwidth reservation when ca-

capacity is available, as well as allows bandwidth resource to be reserved in advance (fig. 2).

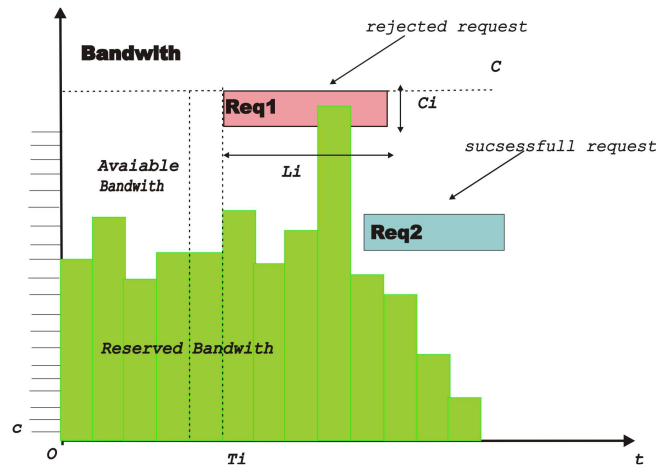


Fig. 2

A preliminary schema using LDAP for configuration of DiffServ networks has been proposed in [3]. The various aspects of a service, such as the traffic profile the user traffic must conform to in order to receive the service, and the forwarding rules for conforming traffic, are captured in a set of policies.

The Architecture of Network QoS Control Using LDAP consists of a management tool, a policy repository, a policy decision entity, and a policy enforcement entity. Fig. 3 shows the functional relations between these different entities. In the context of the service environment under consideration, the management tools are used by the network administrator to populate and maintain the LDAP directory with policies. Management tools may or may not reside on the same host as the directory server. Enforcement entities apply policy rules. A decision entity and enforcement entity are usually assumed to reside at each edge device, or network access point. The edge device is referred to by its location and would most likely be placed at the access point between a local subnet and the backbone network, or at the boundary between backbone networks of two service providers. At initialization, the edge device identifies its interface addresses. It determines the set of policies required for these interfaces, and downloads the corresponding classification policy rules from the LDAP server, as well as the service specifications referred by the policies. Subsequently, the edge device may poll the server periodically to learn of modifications to the directory, and download its set of policy rules if the directory is modified. If asynchronous mode operations are supported by the directory service, the downloading

of policy rules could also be triggered upon changes in the policy rules.

The decision entity downloads policy rules from the repository, through a LDAP client. The enforce-

ment entity queries rules from the decision entity and carries out packet handling and monitoring functions.

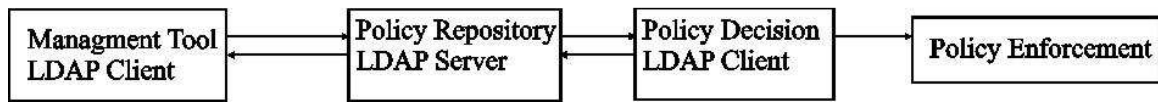


Fig. 3

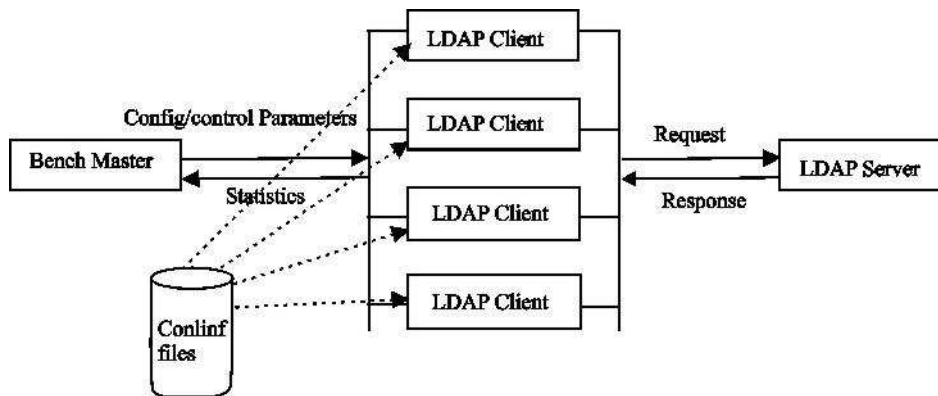


Fig. 4

A customer attaches to the network at one or more interfaces belonging to an edge device. Each interface is identified by an IP address. At each interface, one or more policies may be defined, and customer packets are monitored and processed according to these policies. Each policy is associated with a service level which defines actions on the part of network elements in handling customer packets. A policy may be applied on the basis of source/destination IP addresses, transport protocols, source/destination ports, and other parameters such as default port, URLs, etc.

Policy rules are stored in the LDAP directory as SLS PolicyRules objects (derived from the *Policy* class described in [3]). SLS PolicyRules objects may have attributes specifying the policy name, priority level of the rule, and the network interfaces to which the rule may be applied, as well as references to objects which specify the traffic profile, period of validity of the rule, type of RSVP service or DiffServ action, etc.

The directory structure of the LDAP directory used in proposed schema for supporting SLS is shown in Fig. 5.

Each *Customer* entry has a set of associated *Interface* entries. The *Policy* entry directly under the *Customer* specifies policy rules common to multiple interfaces belonging to the customer, while the *Policy* entry for each *Interface* specifies the policy

rules specific to customer traffic at that Interface. In general, the *Policy* entry refers to one or more of the *Service* entries in the directory to specify the service to be received by the corresponding traffic.

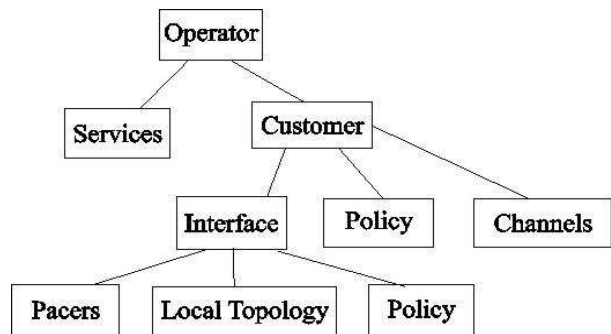


Fig. 5

The other entries shown in the LDAP directory include *Channel* and *Pacer* entries. A channel is a virtual pipe between an ingress edge device and an egress edge device. A pacer is the abstraction that limits the total amount of traffic that can be sent out into the backbone network at an access point.

The search filter for the search operation was constructed from the Interface address of interest, and the corresponding *Policy* object.

3. PERFORMANCE ANALYSIS OF SLS ADMINISTRATION SCHEME

Usually, the response delay at the LDAP server is obtained using the result of a nonpreemptive priority-based M/G/1 queue [2]. Thus, if we want to evaluate the response delay at the LDAP server, we only should consider the messages having higher priority than LDAP ones and ignore the lower

priority messages, but these assumptions are not quite realistic in common case. The response delay at the LDAP server can be estimated more precisely by proposed bellow simulation model. The simulator is created with GPSS (General Purpose Simulation System) World Student version.

The simulation model is represented by following GPSS– block diagram (fig. 6).

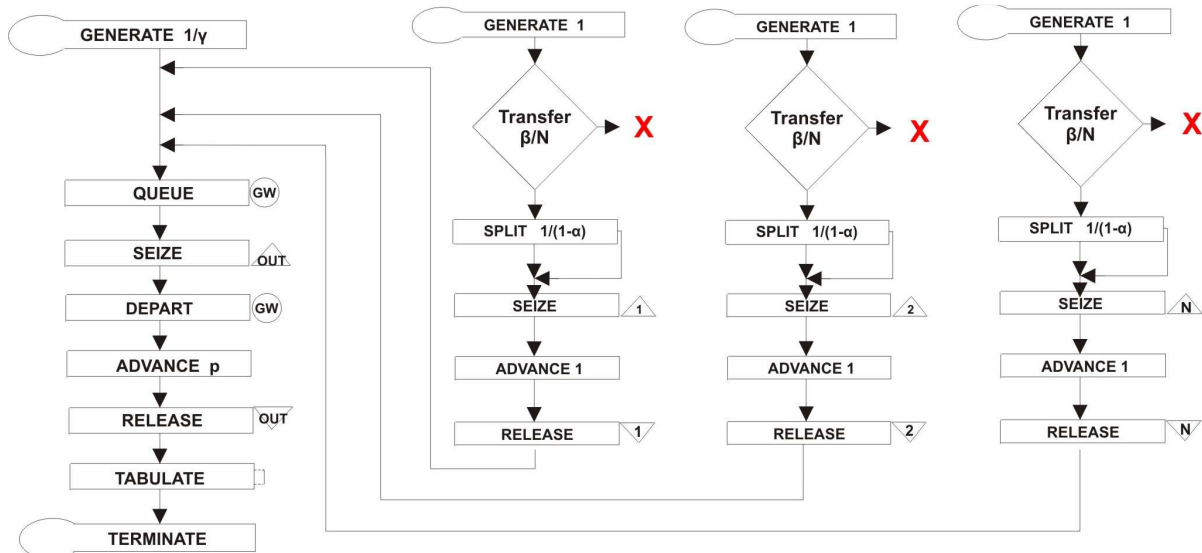


Fig. 6

There are N model segments which correspond to server processing of LDAP requests (in manner one thread one request) and one model segment which corresponds to the transmission (over communication channel) of LDAP as well as non- LDAP messages.

The number of LDAP clients (which generate requests) is N. Note that LDAP server can be multi-processor system with M processors and each processor can start L threads, i.e. $K=M.L$. If $N>K$, the model segments which correspond to processing of LDAP requests would be realized with only K facilities, e. g. duplicating model segments- 1,2,...k the necessary times.

The modeling process aims at getting the response delay for LDAP requests. The delay includes two components- search time and transmission delay (latency due transport over communication channel). The search time, or processing time due to bind (open the connection) and search in directory actually increases slightly at heaviest load. The time slot in this model is time that one thread processes one byte of the LDAP request.

The entry size for these simulations is random and realistic values in each data item, and the de-

fault directory size is 10 000 entries. We make the assumption that these entry sizes are geometrically distributed with mean value $1/(1-\alpha)=490$ bytes. The probability that the LDAP clients start a new request is denoted by β , therefore the probability that a client starts a new request is β/N . We assume $\beta=0.008$ and $N=10$.

The bandwidth of the communication channel (through Internet) is considered fixed, but only a fraction σ of it is available for the transmission of LDAP messages. The ratio between the transfer rate from LDAP server and the communication channel bandwidth is denoted by ρ . We assume $\rho=\{1, 2, 3, 4, 5\}$ and 10 Mbps channel.

The system load is:

$$\rho = \frac{\beta \cdot p}{\sigma(1 - \alpha)} \tag{1}$$

Also, we assume $\rho=0.4, 0.5, 0.65,$ and 0.98 and connection rate characteristics for the two type (LDAP as well as non- LDAP) messages. The load at the communication channel for non-LDAP message is generated by source (fig.6) with mean rate- γ , i.e:

$$\gamma = \left(\frac{1-\sigma}{\sigma} \right) \left(\frac{\beta}{1-\alpha} \right). \quad (2)$$

Thus, the desired values of load- ρ correspond to the values of γ (The latter is an adjustable parameter).

Table1 shows the LDAP response delay, or latency versus load generated by LDAP and non-LDAP messages.

Table1

Delay,us	$\rho=0,98$	0,65	0,5	0,4
$\rho=1$	48608	1869,5	953,1	639,58
2	48119	1857,8	948,93	637,51
3	47630	1845,7	944,44	635,18
4	47140	1833,4	939,81	632,74
5	46650	1820,9	935,12	630,25

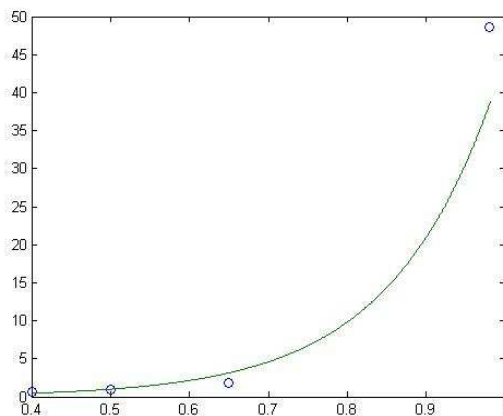


Fig. 7

Fig. 7 represents graphically first row of this table, as well as trendline for delay versus LDAP and non-LDAP load. Note, that the dimension of Y- axe is ms. As one can see the LDAP response delay increases with the system load, which is logical.

4. CONCLUSIONS

In this work, we propose a modified LDAP schema for supporting Service Level Specifications. This article also provides a study of response delay at the LDAP server, which is used to configure networks for supporting different levels of services.

In order to decrease LDAP response delay, or improve performance, the dual processor server could be deployed. The dual processor server shows similar performance at low loads, and the advantage increases to give roughly 40% smaller latency at higher loads for the total response time. The reduction in latency is observed mainly due to the reduction in the so-called connect time.

References

- [1] Chieng D., Marshall A., Parr G. SLA Brokering and Bandwidth Reservation Negotiation Schemes for QoS-aware Internet // eTrans. on Network and Service Management. — 2005. — 1st Q. ,pp. 39—49.
- [2] Fathi H., et al. Optimization of SIP Session Setup Delay for VoIP in 3G Wireless Networks, IEEE Transactions On Mobile Computing, Vol. 5, No. 9, September 2006, p. 1121
- [3] Handbook on Quality of Service and Network Performance. ITU-T, 2003.
- [4] Su H.K., Yau Z.Z., Wu C.S., Chen K.J. Session-Level and Network-Level SLA Structures and VoIP Service Policy over DiffServ-Based MPLS Networks // IEICE Trans. Commun. - 2006. - V. E89-B. - № 2, pp.. 383-391.
- [5] Ефимушкин В.А., Ледовских Т.В. Бизнес-модели SLA-отношений // В сб.: Технологии информационного общества: Тезисы докл. Московской отраслевой научно-технической конференции, 23—25 апреля 2007 г. , М.: Инсвязьиздат, 2007, с.13.
- [6] Ефимушкин В.А., Ледовских Т.В. Особенности управления SLA для обеспечения требований качества услуг в пакетных сетях, сп. Электросвязь No 10, 2008 г., с. 8- 11.

COMPARISON OF THE GAUSSIAN WINDOW AND WATER FLOW ALGORITHM FOR PRINTED AND HANDWRITTEN TEXT PARAMETERS EXTRACTION

D. Brodić¹ & Z. Milivojević²

¹University of Belgrade, Technical Faculty Bor
Vojske Jugoslavije 12, 19210 Bor, Serbia, e-mail: dbrodic@tf.bor.ac.rs

²Technical College Niš
Aleksandra Medvedeva 20, 18000 Niš, Serbia, e-mail: zoran.milivojevic@vtsnis.edu.rs

Abstract

In this paper two algorithms: Gaussian window and water flow algorithm for text parameters identification and extraction are presented. As a result of algorithms extended text area is formed. It is used for text parameters calculation and estimation. Using numerical methods such as least squares and interpolation, reference text line and skew rate are calculated, estimated and extracted.

Both algorithms are analyzed, examined and evaluated under different printed and "handwritten" text samples. Result from experiments pointed out their strengths and weakness. Finally, both algorithm results are given, compared and summarized.

Algorithms showed robustness for wide variety kinds of skewness.

1. INTRODUCTION

Sample printed text is usually well formed and characterized by strong regularity in shape. Different text lines have similar orientation. Hence, they have similar or equal skewness. Due to, their orientation hasn't variability on same text page. Descendants and ascendants from neighbour text lines are sufficiently apart from. So, they aren't mix up mutually. It means text distance between lines is big enough to regularly split up text lines. Similarly, word in text lines are formed regularly with pretty similar distance and inter word spacing is decent as well.

Unlike, handwritten text is fully or partially curvilinear text. It tends to be differently oriented and skewed. Text lines in the handwritten documents are primarily curvilinear and close to each other. Descendants and ascendants from neighbour text lines are occasionally mix up. Text distance between lines is close to each others. So, text lines get into each other. Word in text lines aren't formed regularly and their distance is different. But, similarly to printed text, handwritten text inter word spacing is tolerable. But, appearance of different orientation skewed lines and text lines close to each other made the handwritten text to be less readable.

Previous work on text line parameters identification and extraction can be categorized in few directions:

- Histogram analysis,
- K-nearest neighbour clustering,
- Projection profile,
- Fourier transform,
- Cross-correlation,
- Other models.

In [1] is mentioned proposed technique of reference line extraction based on identifying valleys of horizontal pixel density histogram. Method failed due to multi-skewed text lines.

K-nearest neighbour clustering method i.e. docstrum [2] is by product of a larger page layout analysis system, which assumed that only text is being processed. The connected components formed by the nearest neighbours clustering are essentially characters only. The method is suitable for finding skew angle. But, it is limited to Roman languages due to poor text line segmentation.

Another method proposed in [2, 3] deal with simple multi-skewed text. It uses as a basis simple type of Hough transform for straight lines. But, it is too specific.

The Fourier transform method is a representation in the Fourier domain of the projection profile method in the pixel domain. The results are mathematically identical, but Fourier transform is only different approach to the same text and document properties projection profile is based upon [2].

The cross-correlation method calculates both horizontal and vertical projection profiles and then compares the shift inter-line cross-correlation to

determine the skew rate. Although method can handle complex layout structure documents, applied range is limited to $(-10^\circ, 10^\circ)$ [2].

Algorithm proposed by [4] model text line detection as an image segmentation problem by enhancing text line structure using a Gaussian window and adopting the level set method to evolve text line boundaries. Author specified method as robust for different languages, but rotating text by an angle of 10° or more has an impact on reference line hit rate.

Method of identifying words contour area as a start of detecting baseline point proposed in [5]. But, the assumptions made on the definition of word elements are too specific.

Method [1] hypothetically assumed a flow of water in a particular direction across image frame in a way that it faces obstruction from the characters of the text lines. This method is adopted in [6]

In this paper, the base modification of methods proposed in [1] and [4] are implemented, analysed, examined and compared.

This paper is organized as follows: Section 2 includes brief description and information on proposed algorithms. In Section 3 text experiments are defined. Further, in Section 4 given results are examined, compared and discussed. In Section 5 conclusion is made as well as further investigation direction.

2. PROPOSED ALGORITHMS

Document text image identification procedure consists of three main stages as shown in Figure 1.

In preprocessing stage, algorithm for document text image binarization and normalization is applied. Now, preprocessing text is prepared for segmentation, feature extraction and character recognition.

During the processing stage, algorithms for text segmentation as well as for skew and reference text line identification are enforced. After that, reference text based on skew and stroke angle, is straightened and repaired. Finally, in postprocessing stage character recognition process is applied.

In this paper, elements of processing stage are employed i.e. feature extraction. A few assumptions should be made before defining algorithm. We suppose that there is an element of preprocessing and processing. After that document text image is prepared for feature extraction. Hence, it represents distinct entity consists of group of words.

Document text image is an input of text grey-scale image described by following intensity function:

$$I(l, k) \in [0, \dots, 255], \quad (1)$$

where $l \in [0, N-1]$ and $k \in [0, M-1]$.

After applying intensity segmentation with binarization, intensity function is converted into binary intensity function given by:

$$I_{bin}(l, k) = \begin{cases} 1 & \text{for } I(l, k) \geq I_{th} \\ 0 & \text{for } I(l, k) < I_{th} \end{cases} \quad (2)$$

where I_{th} is given by Otsu algorithm [8].

Now, separated and extracted text line is represented as digitized document image by $M \times N$ dimension matrix X . Each word in document image consists of black points i.e. pixels. Every point is represented by number of coordinate pairs such as:

$$X(i, j) \in [0, 1], \quad (3)$$

where $i = 1, \dots, N, j = 1, \dots, M$ of matrix X [9, 10].

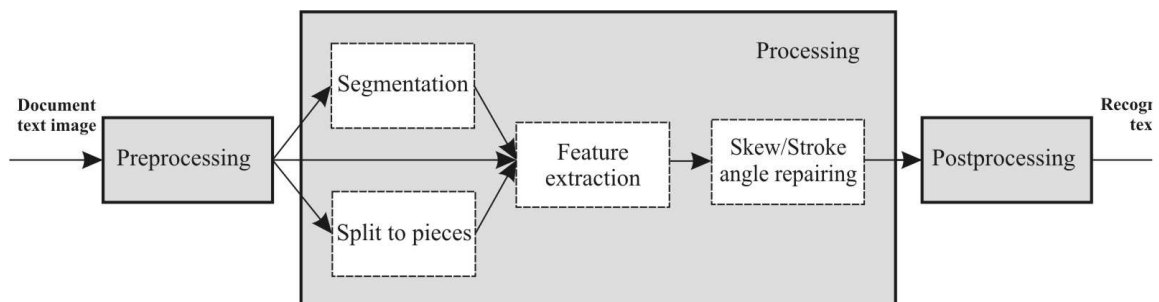


Fig. 1. Document text image identification procedure

2.1. Gaussian window algorithm

Algorithm using Gaussian window (GW) expands black pixel area by scattering every black pixel in its neighbourhood. Around every black pixel new pixels are dispersed. Those pixels have lower intensity of black i.e. level of greyscale. Its intensity depends on their position or distance from original black pixel. Our document image matrix is again greyscale. Hence, intensity pertains in level region [0-255]. Our black pixel of interest has coordinate X_{ij} and intensity of 255, while neighbour pixels have around coordinates and intensity smaller than 255 i.e. greyscale level.

After applying Gaussian window, equal to $2 \cdot K + 1$, on document image, text is scattered forming enlarged area around it.

Converting all non black pixels in the same area, as well as inverting image, forms the black pixel expanded areas. Expanded areas example is given in Figure 2.

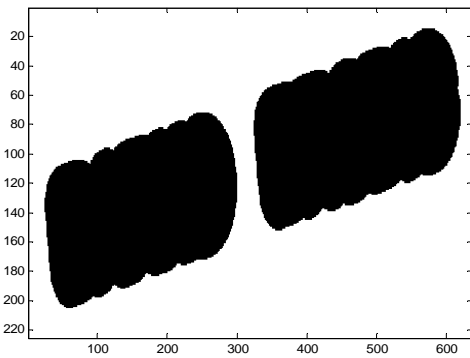


Fig. 2. Expanded text areas

2.2. Water flow algorithm

Original water flow algorithm (WF) assumes hypothetical water flows under only few specified angles of the document image frame from left to right and vice versa [1]. Previously, the definition of pixel type is needed (See Figure 3).

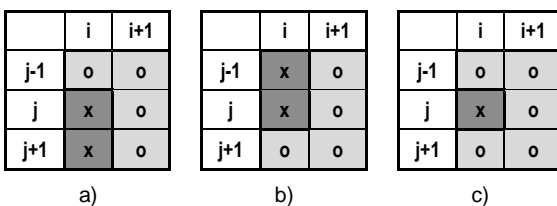


Fig. 3. a) Upper boundary pixel, b) Lower boundary pixel, c) Boundary pixel for additional investigation

Proposed algorithm verifies boundary pixel type in document text image. After verification, it makes unwetted areas around the words. Due to upper or lower pixel type, area slope is α or $-\alpha$. Specifically, additional verification is made on pixel for additional investigation. It can be lower, upper or no boundary pixel due to its neighbour area. Apart from [9] and [10] enlarged window $R \times S$ pixels is defined as a basis. For analysis, it is proposed $R = 5$ and $S = 7$ [6]. Position of window is backwards from pixel candidate for additional investigation. After additional investigation pixel type is designated [6]. Simplifying, unwetted areas algorithm draws area under specified angles. As a result words are bounded by unwetted dark stripes. These regions are pointed out by lines defined as:

$$y_{\alpha} = k * x, \tag{4}$$

where slope $k = \tan(\alpha)$. Lines defined by slope make connection in specific pixel creating unwetted area defined as grey region in Figure 4.

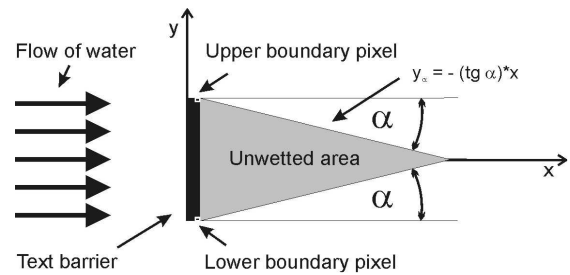


Fig. 4. Expanded text areas

Basic water flow algorithm is proposed with fixed water flow angles of: 14° , 18.4° , 26.6° and 45° applying distinct masks on original document image [1]. In [6] water flow algorithm is extended in its formulation. Still, making straight lines from boundary pixel type and connecting each others in specified point makes unwetted region as well. But, water flow algorithm is free to choose different α from 0° to 90° . Unfortunately, whole range of α can't employ due to words limitation to form connected text line regions.

2.3. Reference text line calculation

The reference line and skew angle identification is based on information obtained from black pixel expanded areas after applying algorithm. Created areas are corner stone of reference text line calculation, estimation and extraction. Defining reference text line means calculating specific average position

of only black pixels in every column of document image. Calculating reference text line is given by:

$$X_i = \frac{\sum_{j=1}^L Y_j}{L} \quad i = 1, \dots, K, \quad (5)$$

where X_i is point position of calculated reference text line, i is number of column position of calculated reference text, Y_j is position of black pixel in column j and L is sum of black pixel in specified column j of an image [1, 9, 10].

After calculation, image matrix with only one black pixel per column is obtained. Black pixel per column defines calculated reference text line and text line skewness. "Calculated" reference text line forms continuous or discontinuous line partly or completely "representing" reference text line. To form continuous reference text line from point's collection some numerical method could be used.

3. TEXT EXPERIMENTS

3.1. Printed text experiment

For the first experiment, sample printed text no.1 is rotated up to 45° by step of 5° around x-axis. Sample text no.1 is given in Figure 5. This sample text reference line is represented by:

$$y = a * x + b, \quad (6)$$

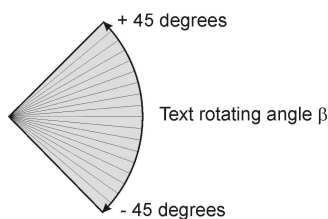


Fig. 5. Sample text no.1

After applying algorithm to sample text, reference text line is calculated by (5). To achieve continuous linear reference text line from point's collection, least square method is used. First degree polynomial function approximation is given by:

$$y = a' * x + b', \quad (7)$$

ndp (number of data points) is used and the slope a' , and the y-intercept b' are calculated as [10]:

$$a' = \frac{(\sum y) * (\sum xy) - ndp * (\sum xy)}{(\sum x)^2 - ndp * (\sum x^2)}, \quad (8)$$

$$b' = \frac{(\sum x) * (\sum xy) - (\sum y) * (\sum x^2)}{(\sum x)^2 - ndp * (\sum x^2)}. \quad (9)$$

Further, referent line hit rate ($RLHR$) is defined by:

$$RLHR = 1 - \frac{\beta_{ref} - \beta_{est}}{\beta_{ref}}, \quad (10)$$

where β_{ref} is arctangent of a (origin) from (6) as well as β_{est} is arctangent of a' (calculated i.e. estimated) from (7). RMS values are calculated by [11]:

$$RMS = \sqrt{\frac{1}{R} \sum_{i=1}^R (X_{ref} - X_{est})^2}, \quad (11)$$

where R is number of examined text rotating angles up to 45° , X_{ref} is $RLHR$ for β_{est} equal to β_{ref} , due to normalization equal to 1, and X_{est} is $RLHR$.

3.2. "Handwritten" text experiment

For further experiment, "handwritten" sample text no.2 is used. Example of "handwritten" text is given in Figure 6.

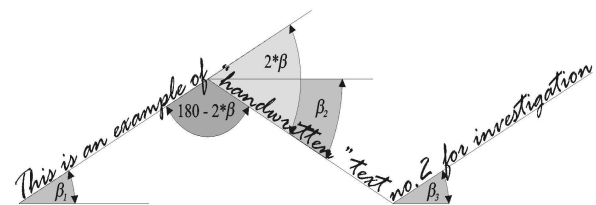


Fig. 6. Sample text no.2

$\beta_1 = \beta$, $\beta_2 = -\beta$ and $\beta_3 = \beta$ are angles of the first, second and third text line, respectively. It could be noticed, second and third text lines are rotated by $2 * \beta$ from "previous" reference text line at once. Hence, this example is rather extreme one. Sample text no.2 with β from $+5^\circ$ to $+25^\circ$ by step 5° and the water flow angle α from 10° to 30° by step 5° are examined.

4. RESULTS AND DISCUSSION

GW and WF algorithms $RLHR$ for sample text no.1 is given in Figure 7 and 8.

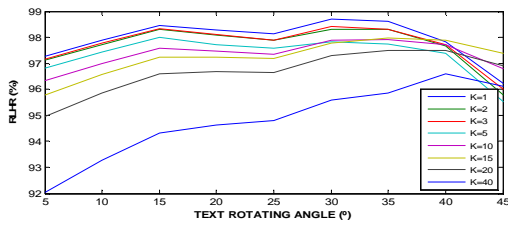


Fig. 7. Gaussian window (GW) RLHR

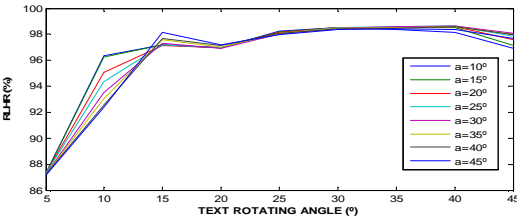


Fig. 8. Water flow (WF) RLHR

GW RLHR is in region 92%-98.5%. Using GW parameter K between 10 and 20 is smart enough due to better segmentation characteristics. This led to RLHR of 95%-97%. WF RLHR is in region 88%-98.5%. Using water flow angles bigger then 15° led to RLHR between 96%-98%. WF vs. GW algorithm RMS comparison is given in Figure 9.

Using bigger K in GW or bigger α in WF tend to wider deviation of results i.e. greater RMS. WF is superior in text rotation angles sub region 5° - 25° , but GW is better in whole region.

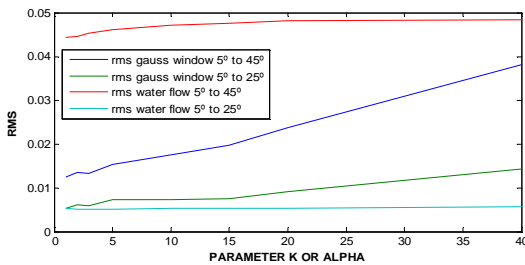


Fig. 9. RMS algorithm comparison

GW and WF RMS for fractured sample text no.2 is given in Figure 10 and 11.

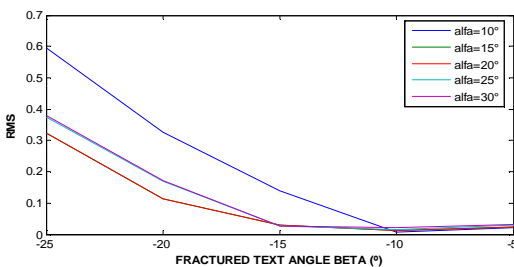


Fig. 10. Fractured text WF RMS

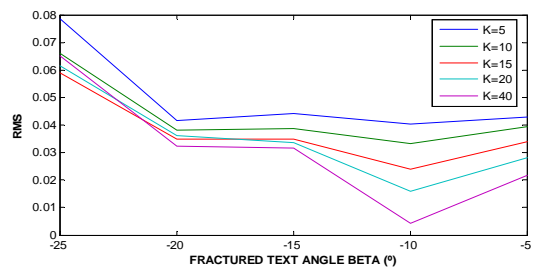


Fig. 11. Fractured text GW RMS

For β_i , ($i = 1, 2, 3$) up to 15° WF is still usable as such as GW. Insensibility to errors is strength of GW evident for bigger β_i . GW and WF fractured text mean RLHR of β_i is given in Figure 12 and Figure 13.

Still, previous noting is similar i.e. WF is better for smaller text rotation angle and GW is better for wider text rotation angle variation.

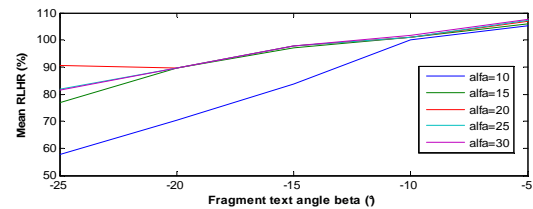


Fig. 12. Fractured text WF mean RLHR

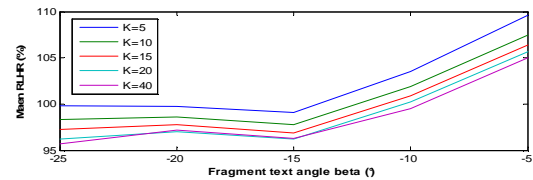


Fig. 13. Fractured text GW mean RLHR

5. CONCLUSION

In this paper, algorithms for reference text line and skew rate identification of printed and handwritten text is presented. It assumes creation of expanded text area based on water flow or Gaussian window algorithm. Both algorithms are analyzed and examined under printed and "handwritten" text samples. Water flow algorithm is well behaved for "smaller" text rotation angle up to 30° , while Gaussian window is more robust in wider rotation angle region. Further improvement of water flow algorithm should be made in creating "water" to follow text rotation angle.

References

- [1] S. Basu, C. Chaudhuri, M. Kundu, M. Nasipuri, D. K. Basu, "Text Line Extraction from Multi-Skewed Handwritten Documents", *Pattern Recognition*, Vol.40, pp. 1825-1839, 2006
- [2] A. Amin, Sue Wu, "Robust Skew Detection in mixed Text/Graphics Documents", *International Conference on Document Analysis and Recognition (ICDAR'05)*, 2005
- [3] G. Louloudis, B. Gatos, I. Pratikakis, C. Halatsis, "Text Line Detection in Handwritten Documents", *Pattern Recognition*, Vol.41, pp. 3758-3772, 2008
- [4] Yi Li, Yefeng Zheng, D. Doermann, S. Jaeger, "A New Algorithm for Detecting Text Line in Handwritten Documents", *18th International Conference on Pattern Recognition*, Vol.2, pp. 1030-1033, Hong Kong, 2006
- [5] Jiren Wang, Mazlor K.H. Leung, Siu Cheung Hui, "Cur-sive Word Reference Line Detection", *Pattern Recognition*, Vol.30, No.3, pp. 503-511, 1997
- [6] D. Brodić, Z. Milivojević, "Reference Text Line Identification Based on Water Flow Algorithm", *ICEST '2009*, SP-2 Sect., Veliko Tarnovo, Bulgaria, 2009
- [7] D. Brodić, Z. Milivojević, "Using Gaussian Window for Printed and Handwritten Text Parameters Extraction", *BALCOR '2009*, Constanca, Romania, 2009
- [8] I. V. Draganov, A. A. Popova, "Rotation Angle Estimation of Scanned Handwritten Cursive Text Documents", *ICEST '2006*, Sofia, Bulgaria, 2006
- [9] R. C. Gonzalez, R. E. Woods, *Digital Image Processing*, 2nd ed., New Jersey: Prentice-Hall, 2002, pp. 67-70
- [10] M. Sonka, V. Hlavac, R. Boyle, *Image Processing, Analysis and Machine Vision*, Toronto: Thomson, 2008, pp. 174-177
- [11] W. M. Bolstad, *Introduction to Bayesian Statistics*, New Jersey: John Wiley & Sons, 2004, pp. 40-44, 235-240

A THREE-DIMENSIONAL RADIO COVERAGE PREDICTION MODEL FOR URBAN OUTDOOR ENVIRONMENT USING PHYSICAL OPTICS AND PHYSICAL THEORY OF DIFFRACTION

A. Chrysostomou, I. Zorbas, E. Papkelis and P. Frangos

*Division of Information Transmission Systems and Materials Technology,
School of Electrical and Computer Engineering,
National Technical University of Athens
9, Iroon Polytechniou Str., 157 80 Zografou,
Athens, GREECE,
Tel. +30 210 772 3694 ; FAX +30 210 772 2281, E-mail pfrangos@central.ntua.gr*

Abstract

The objective of this paper is the presentation of a three-dimensional model which simulates the electromagnetic propagation in outdoor urban areas for GSM frequencies (900 - 1800 MHz), through the combination of separate propagation mechanisms. The simulation results of each propagation mechanism are analyzed in order to derive its contribution to the total received field. The simulation program is created using Matlab.

The mechanisms considered for evaluation are the Line-of-Sight, scattering and diffraction. The produced radiocoverage diagrams indicate the importance of scattering and diffraction as mechanisms of electromagnetic propagation in mobile telecommunications coverage in dense urban environments. They also provide a satisfactory radio coverage prediction for three-dimensional space taking into account the difference in height between the transmitter and the receiver.

1. INTRODUCTION

The goal of our research is to create tools which provide accurate predictions of the electromagnetic field in urban areas in order to reach a required level of coverage.

For the creation of these algorithmic tools we took into account three distinct propagation mechanisms, Line-of-Sight, scattering and diffraction. The computation of the scattered field from planar surfaces was achieved with the use of Physical Optics theory, whereas the computation of the diffracted field from three-dimensional wedges was achieved with the use of Physical Theory of Diffraction.

In the case of scattering, the calculation of reflections from the ground is based on Geometrical Optics, while the calculation of scattering from the finite building surfaces is based on Physical Optics. Our model takes into account not only first but also second order phenomena. Consequently, it computes the field that is reflected from the ground surface and then scattered from a building facet, and vice versa.

In the case of diffraction, Ufimtsev's Physical Theory of Diffraction is used to perform simulation in two-dimensional space and subsequently Mitzner's theory, in order to expand that simulation to three-dimensional space.

2. SIMULATION CONSIDERATIONS

The following assumptions are made for the simulations:

- The buildings are considerably taller than the position of the transmitter.
- All buildings have four wedges.
- Buildings' shape: not necessarily rectangular.
- Only first order wall scattering and diffraction are taken into account.
- Phenomena of depolarization are not being examined.

3. ALGORITHM SIMULATION STEPS

3.1. Step 1: Data Input

The data inserted by the user to the simulation program are:

- the electromagnetic characteristics of the incident field, i.e. frequency, polarization, intensity,
- the geometry of the scene,
- the location of the transmitter,
- the height of the receiver.

3.2. Step 2: Identification of the Shadow Region

Based on our assumption that the buildings are considerably taller when compared to the height of the transmitter, we can assume that the shadow region remains unaltered independently of the position of the receiver, and therefore it can be calculated in 2-D space. To achieve that, the simulator separates the given space into pixels and runs through all of them sequentially to determine which are illuminated by the transmitter. The result of this step is demonstrated in Figure 1.

The shadowing algorithm also returns matrices containing the illuminated facets (edges and vectors) and illuminated wedges of the buildings. These will be used as input to the algorithms that compute the scattered and diffracted fields respectively.

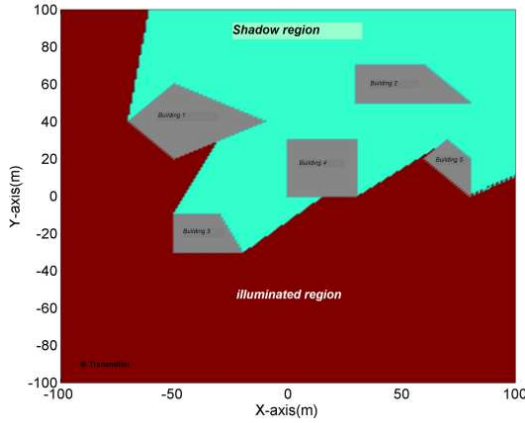


Fig. 1. Shadow region calculation

3.3. Step 3: Calculation of the LOS (Line-of-Sight) field

The LOS field is automatically calculated for all the pixels that the simulator determines as being illuminated by the transmitter. The following equation is used for the calculation:

$$E_{LOS-3D} = E_0 \frac{e^{-jkr}}{r} \quad (1)$$

where k is the propagation constant, E_0 is a constant related to the emitted power given in V/m and r is the propagation path length.

3.4. Step 4: Calculation of the Scattered field

The scattered field is computed as the sum of the complex vectors that arrive at the receiver antenna from the four paths, described in the following paragraphs.

In order to compute the scattered field, we used the 'Near to Far Field Transformation' method [4]. Specifically, we perform segmentation of the scattering surface into an appropriate number of small rectangles (cells), when the receiving antenna is located in the near or Fresnel zone of the scatterers. By such a subdivision of the electrically large scatterer, an observation point which is originally located in the near or Fresnel zone of the scatterer, is then transferred to the far region of the smaller cells.

3.4.1. First order ground reflection

In the case of first order ground reflection the Image Theory is applied, as demonstrated in Fig. 2.

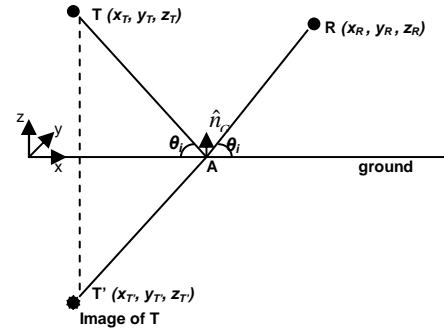


Fig. 2. First order ground reflection (T:Transmitter, R:Receiver)

The receiver field is:

$$E_R = E_T \cdot \bar{R} \cdot \frac{e^{-jk(T'R)}}{(T'R)} \quad (2)$$

where \bar{R} is the binary Fresnel reflection factor. The Fresnel reflection factor acquires the following value for horizontal polarization of the electromagnetic field (vertical to the plane of incidence):

$$R_{\perp}(\vartheta_i) = \frac{\sin(\vartheta_i) - \sqrt{\epsilon_c - \cos^2(\vartheta_i)}}{\sin(\vartheta_i) + \sqrt{\epsilon_c - \cos^2(\vartheta_i)}} \quad (3)$$

In the case of vertical polarization of the electromagnetic field (parallel to the plane of incidence), the Fresnel reflection value is:

$$R_{\parallel}(\vartheta_i) = \frac{\epsilon_c \cdot \sin(\vartheta_i) - \sqrt{\epsilon_c - \cos^2(\vartheta_i)}}{\epsilon_c \cdot \sin(\vartheta_i) + \sqrt{\epsilon_c - \cos^2(\vartheta_i)}} \quad (4)$$

where angle ϑ_i is the angle of incidence at the reflection surface, and $\varepsilon_c = \varepsilon_r - i60\sigma\lambda$. The factor ε_c depends both on the electrical characteristics of the surface and the frequency of the signal.

The steps followed for the simulation in this case are:

- Definition of the image of the transmitter
- Definition of the reflection point for every point of the receiver plane
- Calculation of the reflection angle from the ground
- Calculation of the Fresnel factor (equations (3) and (4))
- Calculation of received field (equation (2))

3.4.2.. First order building scattering

The geometry used for the calculation of the first order scattered field from a building facet is presented in Figure 3.

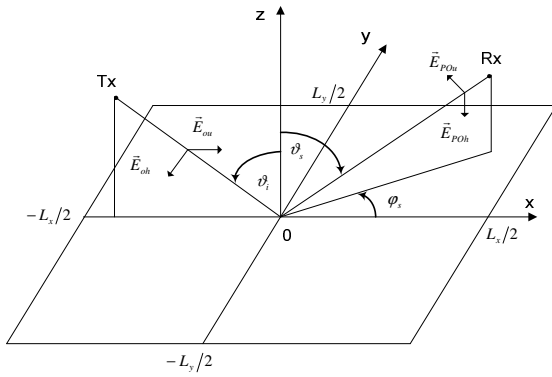


Fig. 3. Geometry for the calculation of scattered field from the building

The equation used for the calculation of the scattered field from a building facet is:

$$E_{PO} = E_0 \frac{jke^{jk(s'-s)}}{4\pi s's} [\cos(\vartheta_i)(1-\bar{R}) - \cos(\vartheta_s)(1+\bar{R})] \cdot L_x L_y \cdot \sin c[k(\sin(\vartheta_i) - \sin(\vartheta_s))\cos(\varphi_s)] \frac{L_x}{2} \cdot \sin c[k(\sin(\vartheta_s))\sin(\varphi_s)] \frac{L_y}{2} \quad (5)$$

where

$s = (T'S')$ is the distance of propagation between the transmitter and the scatterer,

$s' = (S'R)$ is the distance of propagation between the scatterer and the receiver,

\bar{R} is the binary reflection Fresnel factor,

k is the propagation constant, $k = 2\pi/\lambda$,

ϑ_i is the vertical angle of incidence,

ϑ_s is the vertical angle of scattering,

φ_s is the horizontal angle of scattering,

L_x, L_y are the dimensions of the scatterer,

E_0 is the emitted electric field (V/m)

\bar{R} is the binary Fresnel reflection factor, given by equations (3) and (4).

The distances s, s' and the angles of incidence and scattering, are measured from the center of the scatterer.

Equation (5) also contains the path loss for the examined case.

3.4.3. First order building scattering followed by ground reflection

Figure 4 presents the application of Image Theory in the case of first order scattering from a building facet followed by a second order reflection from ground.

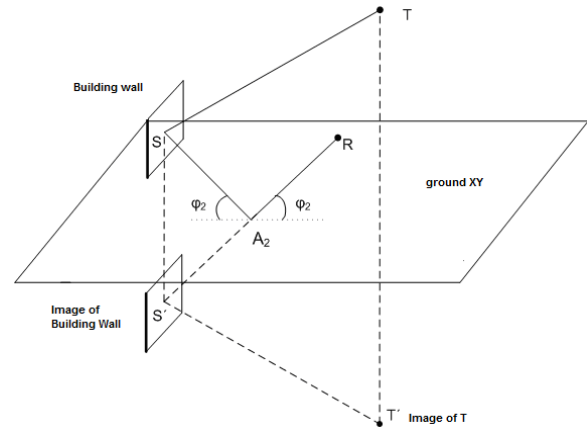


Fig. 4. Geometry for double reflection - Image Theory

Following the calculation of the scattered field from the building facet, the simulator multiplies that field with the Fresnel factor to derive the final received field.

In the case of second order scattering, we assume that the polarization of the incident wave on the ground is the same as that of the incident wave on the building facet, as we do not examine phenomena of depolarization.

3.4.4. First order ground reflection followed by building scattering

Figure 5 presents the geometry applied for first order ground reflection followed by second order scattering. In this case an image of the scattering

surface is not necessary, as the secondary source towards the scatterer is the ground surface.

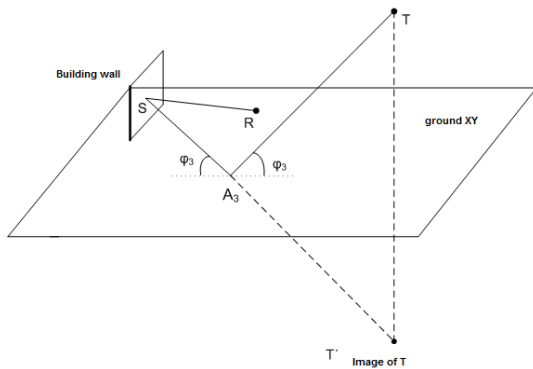


Fig. 5. Geometry for double reflection – Image Theory

Equation (2) is first applied to calculate the reflected field, and then equation (5) is applied to calculate the scattered field, where $s = (T'S)$ and $s' = (SR)$.

3.4.6. Simulation Examples

The following data were used for the simulation:

- Ground: $\epsilon_r=15, \sigma = 7 \text{ S/m}$
- Building: $\epsilon_{r_wall}=7, \sigma_{wall}=0,2 \text{ S/m}$
- Building Surface dimensions: $l_y=16\text{m}, l_z=12\text{m}$
- Building Surface Position: $x=15\text{m}, y=0\text{m}$
- Transmitter position: $x=100\text{m}, y=50\text{m}, z=6\text{m}$
- Receiver height: $1,5\text{m}$
- Frequency: 900MHz
- $E_0 = 5 \text{ V/m}$
- Area dimensions: $200\text{m} \times 200\text{m}$

In Figure 6, we observe the simulation results of the first case, where we take into account only first order ground reflection.

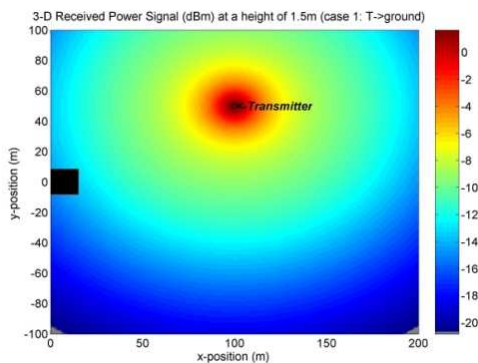


Fig. 6. First order scattering from the ground (Power density in dBm)

In Figure 7, we observe the simulated field that results from first order scattering on the building, and subsequent second order reflection from the

ground, for several positions of the transmitter. The building is coloured black, and we assume, for convenience, that there is no received field in the gray area behind the scattering surface.

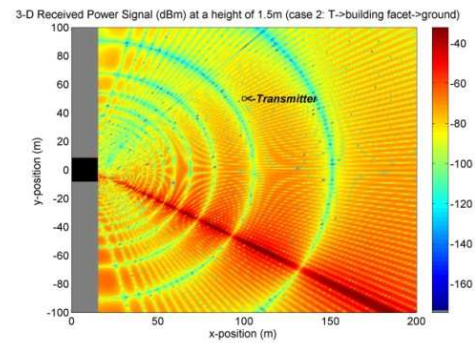


Fig. 7. First order scattering from the building followed by second order the ground reflection (Power density in dBm)

Figure 8 presents the case of first order ground reflection followed by scattering on a building. The results are similar to those of the previous case.

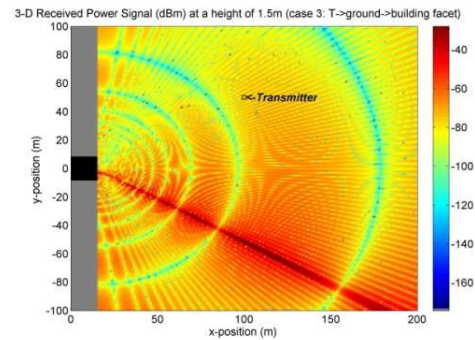


Fig. 8. Ground reflection followed by scattering from the building (Power density in dBm)

3.5. Step 5: Calculation of the Diffracted field

The diffraction algorithm is applied by the simulator on all those wedges returned by the shadowing algorithm, i.e. all those building wedges directly illuminated by the transmitter. It must be noted that only first order diffraction phenomena are taken into account. The simulation is based on Mitzner's theory, that uses Incremental Length Diffraction Coefficients (ILDC) to provide the approximation of the diffracted field by a wedge of any outline. According to this theory, the 3D diffracted field is given by the following expression [2,3]:

$$\overline{E}_d = 2E_0\psi_0 dt \left[\begin{array}{l} (D_{\perp} - D'_{\perp})\hat{e}_{\perp}^s \cos \gamma - (D_{\parallel} - D'_{\parallel})\frac{\sin \beta}{\sin \beta'} \hat{e}_{\parallel}^s \sin \gamma \\ -(D_x - D'_x)\frac{\sin \beta}{\sin \beta'} \hat{e}_{\perp}^s \cos \gamma \end{array} \right] \quad (6)$$

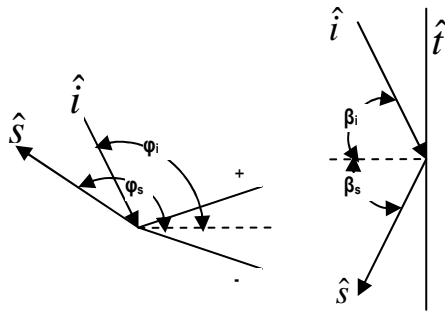


Fig. 9. Presentation of the angles for wedge diffraction in Mitzner's ILDC theory [2,3]

where the diffraction coefficients D_{\perp} , D_{\parallel} , $D_{\perp\perp}$, D'_{\perp} , D'_{\parallel} , $D'_{\perp\perp}$ are given by Mitzner's theory, and include special step functions which set on and off the respective diffraction physical optics coefficients depending on the facet of the wedge that is illuminated.

Figure 10 presents the diffracted field in the case where both facets of a rectangular wedge are illuminated.

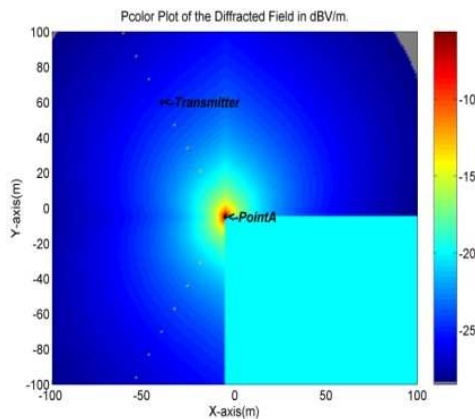


Fig. 11. Diffracted field in the case of illumination of both facets of the wedge (dBV/m)

3.5. Calculation of Total Field

The total received field is computed as the vector sum of the LOS, the scattered and the diffracted field :

$$E_{tot} = E_{LOS} + E_{PO_scattered} + E_{PTD_diffracted} \quad (7)$$

This computation is performed by the simulator for each pixel into which the space is segmented. In every case the simulator takes into account the specific contributions by each propagation mechanism and applies the corresponding values to the sum of the received field in the specific pixel, generating the simulation diagram for a specific height (which is the height of the receiver).

The corresponding path loss in dB is:

$$L_{3-D} = -20 \cdot \log_{10} \left(\frac{\lambda}{4\pi} \cdot \frac{|E_{tot}|}{E_0} \right) \quad (8)$$

4. CONCLUSION

On the basis of the aforementioned prediction data, concerning the simulated radio coverage derived through the combination of the particular contributions of LOS, scattered and diffracted field, we can conclude that scattering and diffraction mechanisms play a vital role in urban telecommunications. In environments with dense architectural structures it is not easily achievable to obtain an unobstructed propagation. In such circumstances, an accurate prediction of the received field under specific conditions is of paramount importance, as it eliminates the need for practical measurements. That kind of prediction is readily available through the use of the algorithmic tools described in this paper.

References

- [1] E. Papkelis, I. Psarros, I. Ouranos, Ch. Moschovitis, K. Karakatselos, E. Vagenas, H. Anastassiou and P. Frangos, A Radio Coverage Prediction Model in Wireless Communication Systems based on Physical Optics and Physical Theory of Diffraction, *IEEE Antennas and Propagation Magazine*, Vol. 49, No. 2, pp. 156 - 165, April 2007.
- [2] K. M. Mitzner, Incremental Length Diffraction Coefficients, Tech. Rep. No. AFAL-TR-73-296, April 1974
- [3] E. F. Knott., "The relationship between Mitzner's ILDC and Michaeli's equivalent currents," *IEEE Trans. Antennas Propagat.*, vol.AP-33, pp. 112-114, January 1985
- [4] E. Papkelis, H. Anastassiou and P. Frangos, 'A time - efficient near - field scattering method applied to radio - coverage simulation in urban microcellular environments', *IEEE Trans. Antennas and Propagation*, Vol. 56, No. 10, pp. 3359 - 3363, October 2008

FDTD ANALYSIS OF A CONICAL MICROSTRIP ANTENNA ON EBG SUBSTRATE

G. S. Kliros, G. Kyritsis and D. Touzloudis

*Hellenic Air-Force Academy, Department of Aeronautical Sciences
Division of Electronics and Communication Engineering
Dekeleia Air-Force Base, Attica GR-1010, Greece
gskmsma@hol.gr*

Abstract

In this paper, the finite difference time domain method in spherical coordinates is used to analyze a microstrip conical antenna with a dielectric electromagnetic band-gap (EBG) structure as substrate. The voltage standing wave ratio, matched impedance, maximum gain as well as far-field radiation patterns, are presented. Our study suggests that the microstrip conical antenna on EBG substrate holds sufficient potential as a low-profile antenna with very wideband and high gain characteristics. A time domain study has shown that the antenna distorts the excitation pulse in a moderate way. These features make the proposed antenna suitable for both ultra-wide band systems and as wind-band scan antenna.

1. INTRODUCTION

The need of ultra-wideband (UWB) antennas is increasing for both military and commercial applications [1]. The UWB radio technology promises high resolution radar applications, sensor networks with a large number of sensors as well as high data rate communication over short range for personal area networks. With a need for antennas with the characteristics of broad bandwidth and small electrical size, conical antenna structures have been a focus of research [2,3]. Moreover, microstrip conical antennas are of significant importance due to conformal capability attributed to their low profile structure [4].

Microstrip conical antennas on uniform dielectric substrates have been proposed and analysed [5]. Dielectric or magnetic conical substrate enables making the antenna electrically smaller and more rugged but cannot improve the radiation efficiency and gain of the antenna. Electromagnetic band-gap (EBG) structures are periodic metallic or dielectric materials that can control the propagation of electromagnetic waves whatever the direction of propagation is. They gained a growing interest in the antenna domain since they have been used as substrates or superstrates in order to improve planar antenna performances [6,7]. Recently, EBG structures have been used as ground planes to produce a uni-directional beam from wideband dipoles with good gain [8].

In this study, a microstrip conical antenna on a dielectric EBG substrate and placed above a

ground plane, is investigated numerically. A FDTD in-house code in spherical coordinates is developed to simulate this novel conical microstrip antenna. Results concerning VSWR, input impedance, maximum gain and far-field radiation patterns are presented. For evaluating waveform distortions, a time-domain study is also presented.

2. ANTENNA DESIGN AND SIMULATION METHOD

The geometry of the proposed conical microstrip antenna on EBG substrate is illustrated in Fig. 1 and is described by the following parameters: the semi-cone angle (flare angle) θ_0 , the free-space semi-cone angle θ_{free} , the length of the antenna's arm ℓ_{ant} and the substrate length ℓ_{sub} . The EBG substrate is made of cylindrical shells with alternating high (Rogers-TMM4: $\epsilon_r = 9.8$) and low (RT-Duroid, $\epsilon_r = 2.2$) permittivity materials with their thickness equal to $\lambda_g/4$ (designed at the central frequency of operating band). The antenna is fed at the tip of the cone by a coaxial cable. It is a rotationally symmetric and is excited by rotationally symmetric source. In order to analyse and optimize the antenna for UWB radio technology, a FDTD code in spherical coordinates is implemented in Matlab following the lines of Ref. [9].

Since the antenna has rotational symmetry about the z-axis, there are no azimuth angle dependencies and therefore, there are three field components: E_r , E_θ and H_ϕ . Using the FDTD me-

thod on a modified Yee cell [9], a set of discrete field equations is obtained:

$$E_r^{n+1}(i, j) = C_a(i) E_r^n(i, j) + \frac{C_b(i)}{(i+1/2)\Delta\theta} \times \left[\frac{\sin((j+1/2)\Delta\theta)}{\sin((j-1/2)\Delta\theta)} H_\phi^{n+1/2}(i, j) - H_\phi^{n+1/2}(i, j-1) \right] \quad (1)$$

$$E_\theta^{n+1}(i, j) = C_a(i) E_\theta^n(i, j) + C_b(i) \cdot \left[H_\phi^{n+1/2}(i-1, j) - \left(\frac{i+1/2}{i-1/2} \right) \cdot H_\phi^{n+1/2}(i, j) \right] \quad (2)$$

$$H_\phi^{n+1/2}(i, j) = D_a(i) H_\phi^{n-1/2}(i, j) + \frac{D_b(i)}{(i+1/2)\Delta\theta} \times \left[\frac{\sin((j+1)\Delta\theta)}{\sin(j\Delta\theta)} E_r^n(i, j+1) - E_r^n(i, j) \right] - D_b(i) \left[\left(\frac{i+1}{i} \right) E_\theta^n(i+1, j) - E_\theta^n(i, j) \right] \quad (3)$$

where,

$$C_a(i) = \frac{1 - \frac{\sigma_i \Delta t}{2\varepsilon_i}}{1 + \frac{\sigma_i \Delta t}{2\varepsilon_i}}, \quad C_b(i) = \frac{\frac{\Delta t}{\varepsilon_i \Delta r}}{1 + \frac{\sigma_i \Delta t}{2\varepsilon_i}}, \quad (4)$$

$$D_a(i) = \frac{1 - \frac{\sigma_i^* \Delta t}{2\mu_i}}{1 + \frac{\sigma_i^* \Delta t}{2\mu_i}}, \quad D_b(i) = \frac{\frac{\Delta t}{\mu_i \Delta r}}{1 + \frac{\sigma_i^* \Delta t}{2\mu_i}} \quad (5)$$

and, Δr and $\Delta\theta$ represent the step size in the r - and θ -directions, respectively. Superscript n signifies that the quantities are to be evaluated at $t = n\Delta t$, and, i and j represent the point $(i\Delta r, j\Delta\theta)$ in the spherical grid. The half-time steps indicate that the fields are calculated alternately. The maximum time step is limited by the stability Courant's criterion:

$$\Delta t \leq \min \frac{r(\Delta r)(\Delta\theta)}{c_0 \sqrt{(\Delta r)^2 + (r\Delta\theta)^2}} \quad (6)$$

where c_0 is the velocity of the light in free space.

The base of the antenna is driven by a voltage signal $V_s(t)$ with internal resistance R_s through a coaxial line with inner and outer conductor's diameters a and b respectively. The electric driving field E_θ , resulting from the input voltage, can be written in FDTD form as

$$E_\theta^n(i, j) = -\frac{V_s(n\Delta t) - R_s I_{in}^{n-1/2}(i, j)}{b \sin(j\Delta\theta) \ln(b/a)} \quad (7)$$

where the current through the source is given by

$$I_{in}^{n-1/2}(i, j) = 2\pi(i\Delta r) \sin((j+1/2)\Delta\theta) \times H_\phi^{n-1/2}(i+1/2, j+1/2) \quad (8)$$

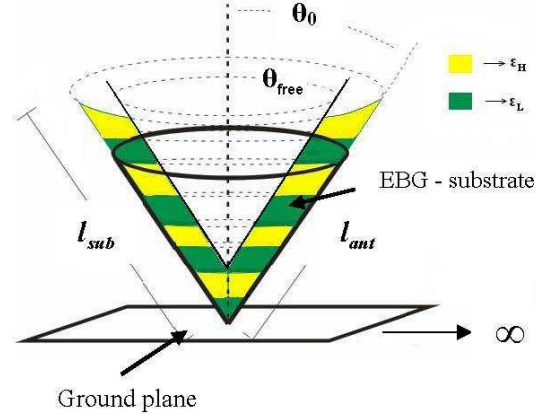


Fig. 1. Geometry of the proposed antenna

Finally, Berenger's perfectly matched layer (PML) is applied as absorbing boundary condition where a parabolic conductivity profile in the spherical PML-region is used [10]. The formulas given above, involve only the electro-magnetic fields within the spherical-FDTD simulation space; in order to calculate radiation patterns, far-fields transfer functions as well as impulse response, the provided near field data have to be transformed to far-field data according to surface equivalence theorem.

3. RESULTS AND DISCUSSION

Parametric studies concerning both impedance and radiation characteristics of the designed antenna, were performed using the above described spherical-coordinate FDTD method. The FDTD cell dimensions are $\Delta r=3$ mm and $\Delta\theta=1^\circ$. The antenna sits on top of a perfectly conducting ground plane that extends 360° in all directions for a distance of $R_m=10 \ell_{ant}$. Just before the maximum radial distance R_m is reached, the simulation space is terminated in a PML section of thickness $20\Delta r$. The maximum reflection coefficient at normal incidence is chosen to be $R(0)=10^{-14}$. An UWB Gaussian pulse (with FWHM = 64 ps) modulated by a continuous sine wave carrier of frequency $f_c=6.85$ GHz, is used in our simulations. The time step is taken $\Delta t = 0.2$ ps, sufficient to satisfy Courant's criterion.

To verify the FDTD steady-state calculations, time-domain fields are transformed to the frequency domain by a Fast Fourier transform routine. The

code was run for a wide range of antenna's parameters combinations in an effort to find the antenna with the best match to a 50 Ω SMA-connector. With the antenna's arm length chosen to be $\ell_{ant}=21$ mm substrate length $\ell_{sub}=33$ mm and $\theta_{free}=10^\circ$, we present results for the voltage standing wave ratio (VSWR), real part of impedance and maximum gain for different flare angles θ_0 of the conical antenna. The free-space angle $\theta_{free}=10^\circ$ corresponds to $\ell_{ant}\theta_{free} \ll \lambda_g$, so that, the microstrip type of the antenna is preserved.

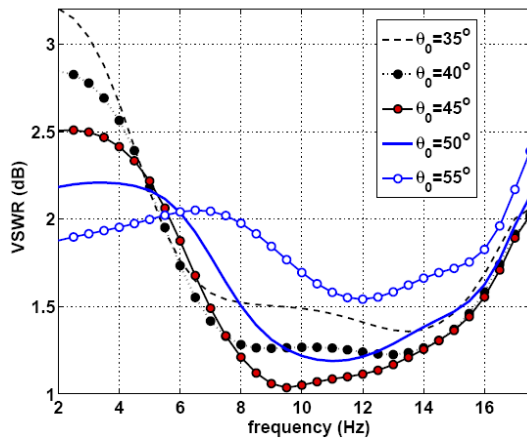


Fig. 2. Simulated VSWR for various flare angles

Fig. 3 shows the VSWR as a function of frequency where for $\theta_0=45^\circ$ the maximum range with $VSWR < 1.5$ is obtained. The corresponding real part of input impedance (Fig. 3) varies with the flare angle, as expected. It is observed that the optimum flare angle $\theta_0=45^\circ$ corresponds to 50 Ω matched impedance in a frequency band from about 5.5 to 15.5 GHz.

Therefore, the designed antenna can provide more than 100% impedance bandwidth.

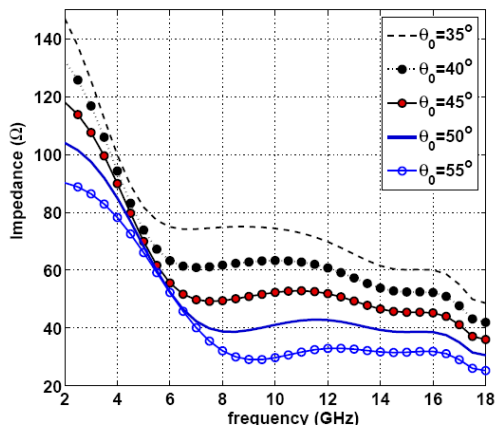


Fig. 3. Real part of input impedance for various flare angles

Fig. 4 shows the evolution of maximum gain in the elevation plane versus frequency. Gain gradu-

ally increases with frequency from 10 dBi to about 14 dBi in the frequency range from 5.5 to 7.5 GHz and ranges from 14 to 15 dBi in the frequency range from 7.5 to 15.5 GHz. Furthermore, the radiation patterns in the elevation plane (vertical polarization E_θ) are calculated in the above frequency range, although for brevity, only the patterns at 6.5, 8 and 10 GHz are shown in Fig. 5. Obviously, the radiation patterns are quite omni-directional but gradually degrade with increasing frequency due to the fact that the antenna's electrical size increases with frequency.

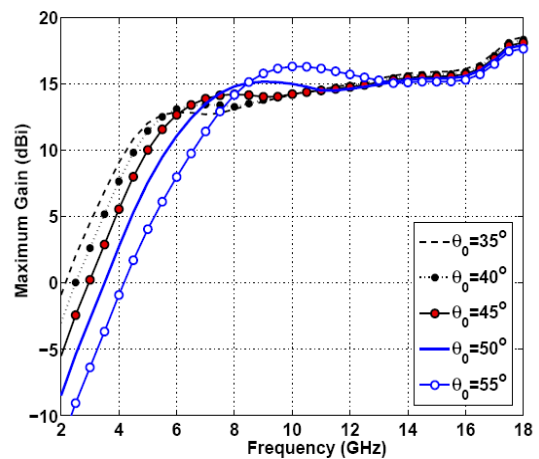
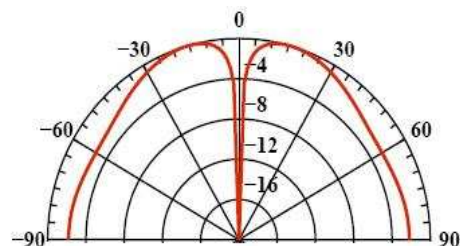


Fig. 4. Maximum gain for various flare angles

For evaluating the waveform distortions caused by the antenna, we examine the degree of similarity between source pulse and received pulse waveforms in several propagation directions. Fig. 6 shows that the radiated pulse, in several radiation angular directions θ_v , is not very different from the excitation signal and therefore, antenna's fidelity in the time domain has been achieved.

The received pulse is a bit larger due to the fact that the antenna has filtered all frequencies outside the impedance bandwidth. For directions $\theta_v > 60^\circ$, a late-time ringing is observed that reveals a non-linearity of far-field phase. However, for a more rigorous study of pulse distortion, the linearity of far-field phase and group delay over the frequency bandwidth, should be evaluated [11,12].



(a)

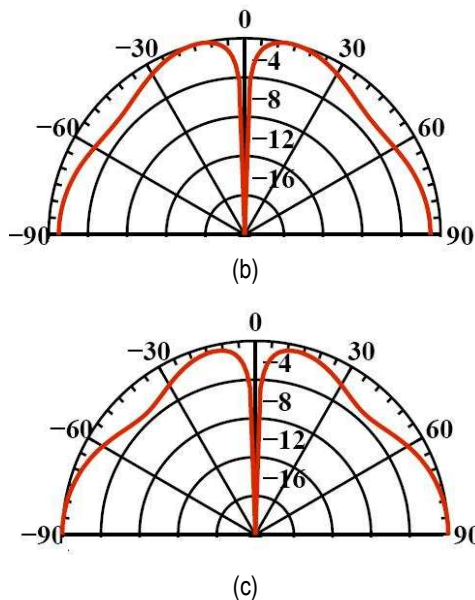


Fig. 5. Computed radiation pattern in the elevation plane at (a) $f=6.5$, (b) $f=8.0$ and (c) $f=10.0$ GHz.

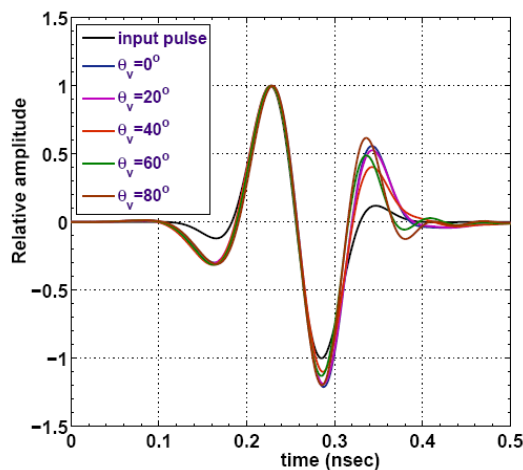


Fig. 6. Excitation and radiated pulses in different propagation directions

4. CONCLUSION

In this paper, a microstrip wideband conical antenna with a dielectric EBG substrate is proposed and analysed. A FDTD code in spherical coordinates is developed to simulate its radiation characteristics. Parametric studies lead to the optimum values of cone's arm length $\ell_{ant}=21$ mm, length of substrate $\ell_{sub}=33$ mm and flare angle $\theta_0=45^\circ$ for 50Ω matched impedance. This design achieves an impedance bandwidth from 5.5 to 15.5 GHz, with stable radiation patterns and a high gain of 10 to 15 dBi at the maximum radiation direction over this bandwidth. The radiation patterns are monopole-like and their frequency dependence is small in the whole UWB frequency band. A time domain study

has shown that the antenna distorts the excitation pulse in a moderate way.

Consequently, our FDTD simulation suggests that a conical microstrip antenna with an EBG-substrate holds sufficient potential as a low-profile antenna with wideband and high gain characteristics.

References

- [1] L. Carin and L. B. Felsen, *Ultra-Wideband Short-Pulse Electromagnetics*, New York, Plenum, 1995, vol.2.
- [2] Y. K. Yu and J. Li, Analysis of electrically small size conical antennas, *Prog. Electromag. Res. Lett.*, vol. 1, 2008, pp 85-92.
- [3] S. Zhou, J. Ma, J. Deng, and Q. Liu, A low-profile and broadband conical antenna, *Prog. in Electromag. Res. Lett.*, vol. 7, 2009, 97-103.
- [4] Y. Lin and L. Shafai, Analysis of biconical microstrip antennas, *IEE Proc.-H*, vol. 139, pp. 1992, 483-490.
- [5] S. Chai, D. Yao, N. Yuan, A conical microstrip antenna with uniform substrate, *Int. J. Infr. Millim. Waves*, Vol.18,1299-1306, 1997.
- [6] G. S. Kliros, K. Liantzas, A. Konstantinidis, Modeling of Microstrip Patch Antennas with Electromagnetic Bandgap Superstrates, *19th IEEE Int. Conf. on Appl. Electrom. and Commun.*, Sept. 2007, Croatia, pp. 181-185.
- [7] G. S. Kliros, K. Liantzas, A. Konstantinidis, Radiation Pattern Improvement of a Microstrip Patch Antenna using EBG Substrate and Superstrate, *WSEAS Trans. on Commun.*, Vol. 6, pp. 45-52, 2007.
- [8] L. Akhondzadeh-Asl, D. Kern, P. Hall, D. Werner, Wideband Dipoles on Electromagnetic Bandgap Ground Planes, *IEEE Trans. Ant. Propag.* vol. 55, 2007, pp. 2426-2434.
- [9] G. Liu, C. Grimes, Spherical-coordinate FDTD analysis of conical antennas mounted above finite ground planes, *Microwave Opt. Techn. Lett.*, Vol. 23, pp 78-82, 1999.
- [10] J.P. Berenger, Perfectly Matched Layer for the FDTD Solution of Wave-Structure Interaction Problems, *IEEE Trans. Ant. Propag.*, Vol. 44, no. 1, pp 110-117, 1996.
- [11] H. Ghannoum, S. Bories, C. Roblin, A. Sibille, Biconical Antennas for intrinsic characterization of the UWB channel, *Proc. IEEE Int. Workshop on Antenna Technology*, pp. 101-104, 2005.
- [12] A. Sibille, C. Roblin, S. Bories and A. C. Lepage, A Channel-Based Statistical Approach to Antenna Performance in UWB Commun., *IEEE Tran. Ant. Propag.*, Vol. 54, no. 11, pp. 3207-3215, 2006.

WAVEGUIDE-FED BACKFIRE ANTENNAS FOR LOW-TERAHERTZ FREQUENCIES

H. D. Hristov¹, M. S. Leong², M. B. Perotoni³, G. S. Kirov⁴, and W. Grote¹

¹Department of Electronics, UTFSM,
Valparaíso, Chile, hristo.hristov@usm.cl

²Department of Electrical and Computer Engineering, NUS,
Singapore 119077, msleong@nus.edu.sg

³Department of Information Engineering, UFABC,
Brazil CEP 09210-170, Marcelo.Perotoni@cst.com

⁴Department of Radiotechnics, Technical University,
Varna, Bulgaria, 9010, gkirov@abv.bg

Abstract

Two X-band backfire antenna designs, proposed and studied years ago by the first and second co-authors, have been re-designed and examined numerically for the low-terahertz (THz) frequency range of 200-300 GHz. For the same gain and transverse aperture, the waveguide-fed backfire antennas, the long (LBFA) and short (SBFA) are very compact in length compared to the optimally designed classical horn. It was found that the presence of dielectric rod element in the LBFA can diminish considerably antenna gain and radiation efficiency. The SBFA is extremely compact and possesses a superior gain and input match bandwidth. Up to 500-600 GHz the miniature backfire antennas can be easily produced by means of precise micromachining technologies.

1. INTRODUCTION

Long backfire antenna (LBFA) originated from the endfire antenna (EFA) by setting the EFA between two plane reflectors: small or endfire and large or backfire [1], [2]. The classical microwave LBFA is fed by a dipole plus small reflector assembly, which launches the surface wave (SW) along the EFA structure. The large reflector acts as a plane mirror that turns the surface wave backward, and thus forcing it to traverse the antenna length multiple times. As a result, the LBFA is acting as an open-end radiating resonator, similar to the Fabry-Perot laser cavity. Thus, the dominant LBFA mode is a standing wave along the SW structure. For centimetre and millimetre waves the backfire antenna with a waveguide-fed SW structure is more natural choice [3]-[5].

If the distance between the large and small reflectors is only about a half wavelength the SW structure becomes redundant. Such antenna is called short backfire (SBFA). Depending on its resonant frequency the SBFA is fed by either a dipole between the reflectors, or by an open-ended waveguide at the side of the large reflector [5], [6]-[8]. With a radiation aperture of about two wavelengths as a rule and an axial length of about a half wavelength the dipole-fed LBFA is very compact

and highly efficient radiator with a gain of about 14-17 dB.

Two X-band backfire antenna constructions proposed and studied experimentally years ago by the first [4] and second [8] co-authors are re-designed and examined numerically for the low-terahertz (THz) frequency range of 200-300 GHz by means of the CST Microwave Office electromagnetic solver [9].

The terahertz waves occupy a relatively unfamiliar portion of the electromagnetic spectrum between the infrared and microwave bands (100-10000 GHz). The frequency band from 100 GHz to 3000 GHz is normally called a low-terahertz or millimetre-wave band. The terahertz waves are of particular interest for imaging of biological objects because of their non-ionizing nature, which renders them as non hazardous for human, unlike X-rays, for instance. Until now, they have been used mainly for space, military and astronomy applications. New application areas found in medicine, the environmental and biological sciences, as well as in security and quality control-have emerged only recently. These drive terahertz research towards cheaper, room-temperature components, including focusing/imaging lenses and antennas, and hence pave the way for terahertz short-range wireless communication systems.

2. LONG BACKFIRE ANTENNA WITH WAVEGUIDE-FED DIELECTRIC ROD

2.1. Antenna geometry and dimensions

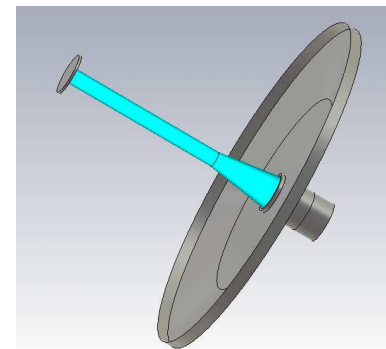
The antenna are fed by a circular TE_{11} -mode waveguide with an inner diameter of 0.97 mm, inserted through the big reflector and terminated by an input flange.

Fig. 1 shows the simulation model of a five wavelengths long LBFA designed at a frequency of 240 GHz (or at a wavelength of $\lambda_0 = 1.25$ mm). It is fed by a round waveguide 1.06 mm in diameter. Through a conical portion of 1.875 mm the rod diameter is decreased to 0.339 mm for producing a loose surface wave along the rod. The large rimmed reflector is plane-conical in shape with an outer diameter of 9.43 mm ($7.54 \lambda_0$). The small reflector is a disk 1.1 mm in diameter. LBFA antenna length (or the distance between reflectors) is equal to 6.26 mm ($5.0 \lambda_0$). The plane area of large reflector has a diameter of 5.63 mm ($7.54 \lambda_0$), and its cut-cone section is 0.31 mm (roughly $0.25 \lambda_0$) in length. The same size (width) has the reflector rim.

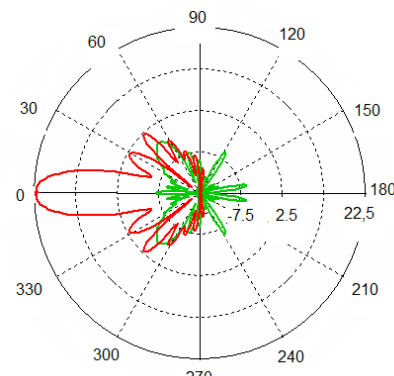
2.2. Numerical results for LBFA

In this section are shown the essential radiation and input antenna characteristics found by means of numerical simulation [9] of the LBFA design, shown in Fig. 1(a). Fig. 1(b) illustrates the co- and cross-polarization gain patterns for the LBFA antenna simulated as an ideal construction made of lossless metal with a conductivity $\sigma = \infty$ and dielectric with a relative permittivity $\epsilon = 2.1$. The co-polar gain pattern (line with a dot at the pattern maximum) shows a peak directive gain of about 22.5 dBi, while the first and second sidelobes are 20 dB down. Since the large rimmed reflector overshadows the rear hemisphere the back co-polar pattern level is very small- less than 40 dB down to the peak gain.

Theoretically the HE_{11} hybrid SW wave in the dielectric rod fed by the TE_{11} -mode metal waveguide is notable by its quasi-plane transverse-field structure. In addition, the LBFA reflectors do not change the radiation field polarization considerably. For the rather tiny antenna size the LBFA has a low cross-polar pattern with a level of about 30 dB down to the peak co-polar gain.



(a)



(b)

Fig. 1. Waveguide-fed LBFA with plane-conical large reflector: (a) LBFA design model, and (b) 45-degree cut plane co-polar (line with big main lobe of 22.5 dBi) and cross-polar pattern (low-level pattern) of LBFA made of idealized (lossless) metal and dielectric

Fig. 2 shows the frequency peak gain variation of the idealized (upper line) and real (lower line) LBFA models within 200-250 GHz frequency range. The upper and lower lines correspond to the directive gain and input gain respectively. The input gain includes losses of the construction materials (metal and dielectric) and is smaller than the aperture directive gain. For the studied LBFA it is assumed that all metal components (waveguide, large and small reflectors) are golden (conductivity $\sigma = 4.1 \cdot 10^7$ S/m) and the SW dielectric rod is made of Teflon (complex permittivity $\epsilon = 2.1 - j0.05$).

Fig. 2(a) shows that in the frequency band 200-250 GHz the studied LBFA exhibits two gain maximums: at around 216 GHz and 238 GHz. The second gain maximum of the lossless antenna is 22.4 dBi high, which corresponds to an aperture radiation efficiency of 60%. The first maximum is by 2.6 dB lower than the second one and could be ignored. Thus, only the antenna behavior around 238 GHz will be discussed. It is found that the -3 dB gain bandwidth around the optimum frequency of 238 GHz is about 8.3 GHz (or 3.5%) for both LBFA models: ideal and real. In conclusion, judg-

ing by the gain bandwidth the LBFA is a narrow-band antenna.

Fig. 2(b) illustrates zoomed in the gain graph pieces close to the optimum frequency of 238 GHz for four material scenarios, specified in the figure's legend. Lines 1 and 4 correspond to the upper and lower graphs in Fig. 2(a), respectively. The two VSWR curves in Fig. 3 illustrate the input match properties of the examined antenna for a lossless (ideal) model (upper graph) and for a real model made-up by metal (gold) and dielectric (Teflon), (lower graph). For VSWR less than 2.0 the LBFA exhibits a frequency bandwidth input frequency range of 10.7 GHz, or 4.5 % relative to the optimum gain frequency of 238 GHz. At the same frequency the real antenna model has VSWR=1.7, which corresponds to a small mismatch loss of 0.3 dB. From Fig. 2 and Fig. 3(a) can be concluded that (i) at the optimum frequency of 238 GHz the total gain loss is about 0.65 dB, from which only less than 0.05 is produced by the metal loss. In other words, at the low-terahertz frequencies both dielectric and mismatch loss are of importance for the realized input antenna gain.

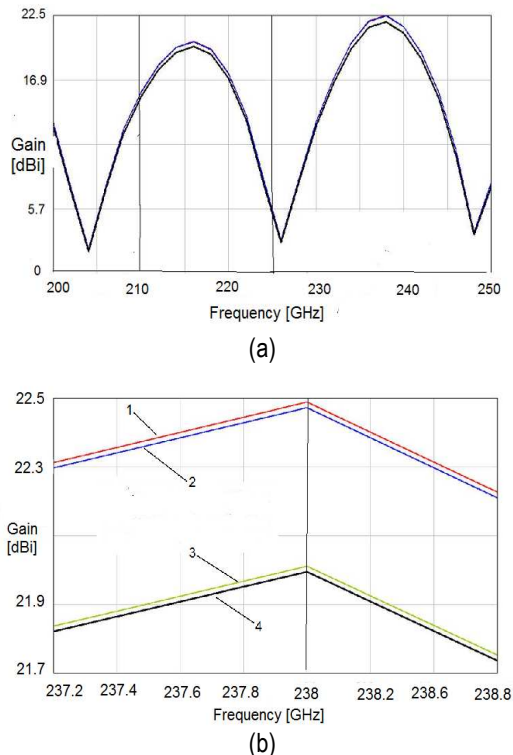


Fig. 2. LBFA gain vs frequency: (a) normal scale graphs for lossless antenna model (upper graph) and for antenna construction made of genuine metal (gold) and dielectric (Teflon), (lower graph); (b) zoomed in pieces of graphs for four material scenarios: 1-lossless metal and dielectric (idealized case), 2-genuine gold and lossless dielectric, 3-lossless metal and genuine dielectric (Teflon) and 4- genuine gold and Teflon (authentic case)

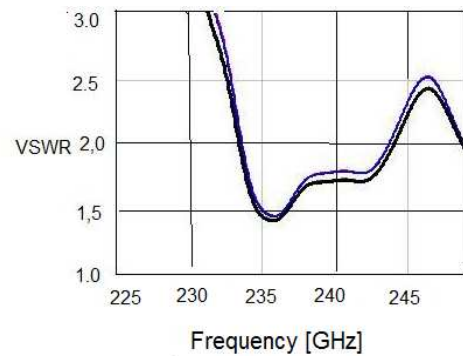


Fig. 3. LBFA input VSWR vs frequency for lossless antenna model (upper graph) and for antenna made of real metal (gold) and dielectric (Teflon), (lower graph)

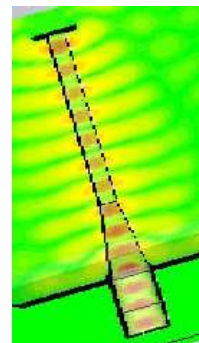


Fig. 4. LBFA: picture of inner standing-wave field distribution

By both gain and input match criteria the LBFA is classified as a narrowband antenna with a relative bandwidth of about 3-4 %. This is due to the antenna standing-wave field density structure inside and outside the dielectric rod as illustrated in Fig. 4. Ten half-wave field maxima (and minima) along the antenna axis are counted between the big and small reflectors, which corresponds to the five-wavelength antenna length. Regardless of its narrowband categorization the low-terahertz frequency LBFA can work in a big frequency range of about 10 GHz and possesses a great signal communication capacity.

3. WAVEGUIDE-FED SBFA

3.1 Antenna design

Fig. 5(a) is a 3D artistic view of waveguide-fed SBFA with a slightly-conical large reflector. The actual SBFA construction, described in this paper, is illustrated in Fig. 5(b) by its axial cross section, where the antenna aperture is covered by a thin Teflon disk (radome), 0.15 mm in thickness, the large reflector rim is extended to the radiation aperture and the waveguide input flange is ignored in this drawing.

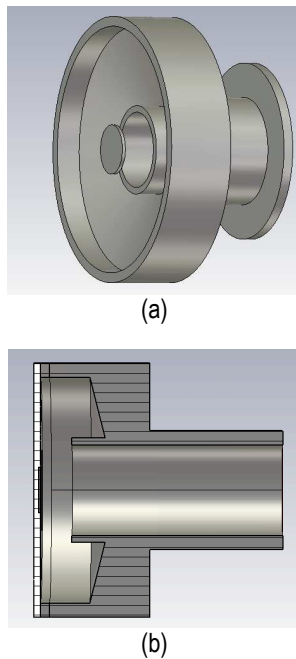


Fig. 5. Waveguide-fed SBFA design with conical large reflector, (a) 3D antenna picture, and (b) axial plane-cut section with dielectric-covered aperture

The studied SBFA is two-and-half wavelengths, or 3.2 mm, in diameter. The small reflector is a disk with diameter of 0.64 mm, and SBFA is just a half-wavelength (0.62 mm) long. The antenna is fed by a circular TE_{11} -mode waveguide with an inner diameter of 1.26 mm. The feed waveguide is inserted through the big reflector, and terminated by a round input flange. This SBFA somewhat differs from the original configuration described in [8], where a rectangular waveguide is utilized.

3.2. Numerical results

The SBFA consist basically from metal (golden) elements. The dielectric cover disk is too thin and practically lossless. Our computer simulation has proved that the dielectric and metal losses jointly make very small reduction of antenna gain (less than 0.1 dB in the 220-270 GHz range of interest). From this follows that the input antenna gain will be roughly equal to its directive gain (directivity) in case of very good input match, or if VSWR is near to less than 1.5.

From Fig. 6(a) is calculated that the studied SBFA has a maximum directive gain of about 17 dBi at a slightly higher optimum frequency of 245 GHz. The SBFA gain bandwidth, calculated at levels -3 dB down to the maximum directive gain is about 16 %.

Besides, the input match bandwidth, calculated from the VSWR vs frequency curve in Fig. 6(b) at the level VSWR=2 is 14.7 % or it is very similar to the directive gain bandwidth.

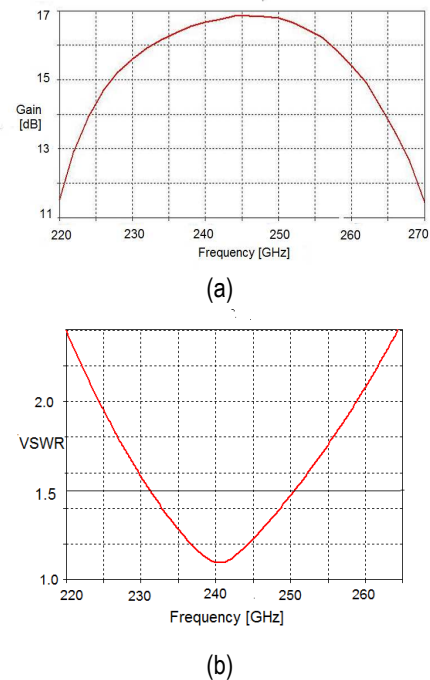


Fig. 6. SBFA directive gain (a) and input VSWR (b) versus frequency

Fig. 7 illustrates both E-plane (a) and H-plane (b) SBFA directive gain radiation patterns.

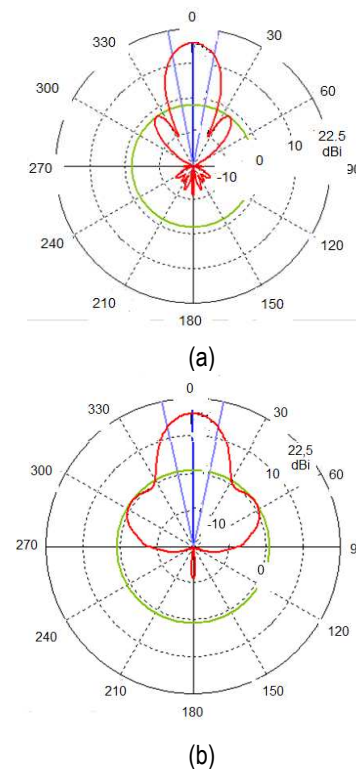


Fig. 7. Co-polar directive gain patterns of SBFA: (a) E-plane cut and (b) H-plane cut

For a very good match (say for VSWR < 1.2) the realized input gain for the frequencies close to the SBFA resonant frequency is practically equal to the antenna directive gain. The studied SBFA configuration has a high radiation aperture efficiency of about 80 %.

In addition, the antenna is extremely compact. Compared to a standard conical horn with the same gain and radiation aperture diameter, the studied SBFA is about 7-8 times shorter.

4. COMPARISON BETWEEN LBFA AND SBFA

Next LBFA and SBFA are contrasted by their dimensions (Table 1) and basic electromagnetic characteristics (Table 2).

In Table 1 are listed D_{BFA} (the aperture diameter) and L_{BFA} (the antenna length) relative to the corresponding BFA wavelength λ_0 . In addition, the ratios between L_{Con} and L_{BFA} are given, where L_{Con} is the length of the conical antenna having an aperture diameter and directive gain equal to those of the corresponding backfire antenna (LBFA or SBFA).

Table 1. Contrast of dimensions

	$\frac{D_{\text{BFA}}}{\lambda_0}$	$\frac{L_{\text{BFA}}}{\lambda_0}$	$\frac{V_{\text{BFA}}}{\lambda_0^3}$	$\frac{L_{\text{Con}}}{L_{\text{BFA}}}$
LBFA	7.5	5.0	220	2.6
SBFA	2.5	0.6	2.9	7.3

Table 2. Comparison of main antenna parameters

	Gain [dBi]	SL [dB]	BL [dB]	Xpol [dB]
LBFA	22.5	-20	-40	-30
SBFA	16.9	-17	-27	-17

Table 2. (Continuation)

	Band width [%]	Eff _a [%]	Eff _t [%]
LBFA	3.5	60	52
SBFA	14.5	80	79

In Table 2 are compared the following LBFA and SBFA parameters: SL (side lobe level), BL (back lobe), Xpol (max 45-deg cross polar level), Eff_a (aperture efficiency) and Eff_t (total efficiency, which includes material losses).

5. CONCLUSIONS

Two backfire antennas, the LBFA and SBFA, have been studied as possible candidates for the low-terahertz band. It was found that the dielectric rod element in the LBFA is the major source of loss and can diminish considerably the antenna gain and radiation efficiency. The SBFA is extremely compact and possesses a superior gain and input match bandwidth. Up to 500-600 GHz the miniature backfire antennas can be easily produced by means of precise micromachining technologies.

6. ACKNOWLEDGMENTS

H. D. Hristov and W. Grote acknowledge the support by the Chilean Conicyt Agency under the Fondecyt Project 1095012 / 2009.

References

- [1] H. W. Ehrenspeck, "The backfire antenna-a new type of directional line source", *Proc. IRE*, vol. 48, pp. 109-110, 1960
- [2] J. Zucker, "The backfire antenna: qualitative approach to its design", *Proc. IEEE*, vol. 53, pp. 746-747, July 1965
- [3] H. D. Hristov and D. Taylor, "Rectangular backfire antenna with dielectric surface wave structure", *Electronics Letts.*, vol. 6, pp. 163-165, March 1972
- [4] A. Kumar, and H. Hristov, "Long backfire antenna with dielectric surface wave structure", *Int. J. Electronics*, vol.43, pp. 309-312, 1977
- [5] A. Kumar and H. D. Hristov, *Microwave Cavity Antennas*, Artech House, 1989
- [6] A. C. Large, *The application of a waveguide feed to a short backfire antenna*, ASWE Techn. Report TR-73-16, Portsmouth, UK, April 1973
- [7] M. S. Leong, and P. S. Kooi, "Rectangular waveguide-excited short backfire antenna with corrugated rim", *Electronics Letts.*, vol. 15, pp. 533-535, Aug. 1979
- [8] M. S. Leong and P. S. Kooi, "Performance of a rectangular-waveguide-excited short backfire antenna employing a conical main reflector", *Electronics Letts.*, vol. 20, No 18, Aug. 1984
- [9] © 2009 CST MICROWAVE STUDIO AG

ON A METHOD TO INCREASE THE EFFECTIVENESS OF CABLE VOD SYSTEMS

Lidia T. Jordanova¹, Jordan I. Nenkov²

1. Faculty of Telecommunications, Technical University, Kliment Ohridski 8, 1756 Sofia Bulgaria

2. Faculty of Telecommunications, Technical University, Kliment Ohridski 8, 1756 Sofia Bulgaria

e-mail 1: jordanova@tu-sofia.bg

e-mail 2: Jordan_n2002@yahoo.com

Abstract

The paper deals with the special features of the VoD service provided over now-a-days CATV networks. A VoD system of the hybrid type is studied, two implementations being considered: the first one making use of proxy servers to redirect the video traffic from the core network to the distribution hubs and the second one using no proxy servers. A concept for the design of CATV networks supporting the VoD service is given. It refers to the choice of: architecture, movie content distribution algorithm, routing protocol to determine the path of the chosen video stream from the server to the subscriber. Movie content distribution strategies based on the Pareto distribution are discussed that take into consideration the subscribers' preferences and refer to the hybrid-type system. Such strategies aim to decrease both the video traffic across the core network and the cost of the network equipment involved.

1. INTRODUCTION

The contemporary VoD systems implementation is based on the intelligent approach, i.e. on the system managers. The system managers coordinate the video content distribution on the VoD servers according to subscribers' preferences and they decide the VoD stream path according to the chosen routing protocol. They can perform the system self-test and the system blocking prevention too.

Depending on the interaction degree, a VoD system can be categorized as follows [1]:

Quasi-Video-on-Demand (QVoD): In this case the users are grouped based on their interests. A user can choose between different programmes by changing user teams.

Near-Video-on-demand (NVoD): The same programme is retransmitted in fixed time slots thus enabling functions such as forward and reverse play.

True-Video-on-Demand (TVoD): The user has full control over the presentation of the programme. The T-VoD fully simulates a VCR (Video Cassette Recorder) enabling functions such as forward and reverse play, freeze and random positioning.

Adaptive-Video-on-Demand (AVoD): In this case the user submits a request for a movie and the decision is made through a routing algorithm.

In this paper the hybrid type VoD system is present, which is a mix between the QVoD, TVoD and AVoD models. The existing CATV system is used for the VoD system realization. The aim of the re-

search is choosing the more appropriate network architecture, video content distribution algorithm and routing protocol determining the video stream root in its transfer between the video server and the subscriber.

2. BUILDING CONCEPT VOD ARCHITECTURE

VOD systems can be deployed in one of three fundamental architectures – centralized, distributed and hybrid [2-3]. The investigations here described are based on the hybrid VoD architecture, which operational diagram is illustrated on Figure 1. In the following approach the biggest VoD platform that is supplied with a large library of movies and program content is installed at the head-end. The smaller VoD servers are located at the distribution hubs (DHUBs) and are limited in both size and storage only for the most popular movie selections.

The realization of the contemporary hybrid type VoD systems is based on the hierarchical approach, as the number of hierarchical levels is commonly three [4-5].

The edge VoD servers are located on the third hierarchical level, which holds the most frequently requested movies for the corresponding subscribers' group. The video stream transfer is performed from these servers to subscribers. These servers can perform proxy servers' functions, which redirects the video stream from another server, which holds the requested movie to the subscriber. On the second hierarchical level the VoD servers with the

most saved requested movies for the corresponding region are located. Between them and the edge VoD servers, an information which contains the number of requests for the corresponding region is exchange periodically. The number of requests is different for each separate group. The Edge nodes are updated periodically according to the subscribers' preferences. On the first hierarchical level is located the Head-End (HE) which coordinates all system performance.

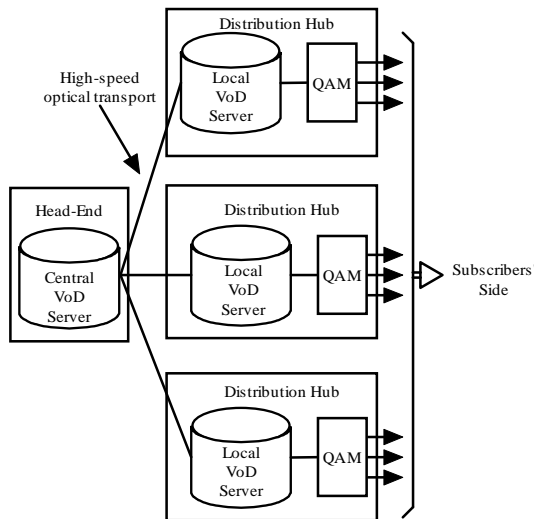


Fig. 1. Hybrid VoD system architecture

With the contemporary VoD systems realization, two main approaches are applied – direct and indirect, which nature is described on the Figure 2 and Figure 3.

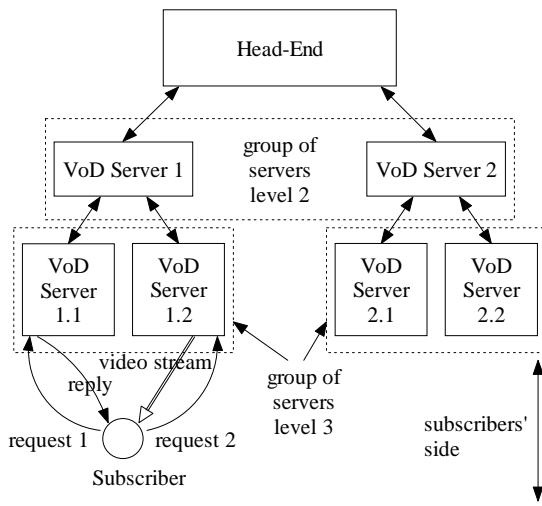


Fig. 2. Direct VoD transfer

The operational algorithm of the model, which is shown on the Figure 2, is following: The request for movie is sent from subscriber to server 1.1. The request arrives at server 1.1 and gets forwarded to

its manager (server 1). Server 1 finds that server 1.2 holds a copy of the movie and has an acceptable load. Server 1 then replies to 1.1 which replies to the user that server 1.2 is capable of playing the movie. Server 1 then informs server 1.2 that it is expected to receive a request from the user to get the movie, and server 1.2 reserves (for a limited period) the necessary resources for the request. Eventually, the user opens a connection with server 1.2 and gets the service directly from it. After the user request is done, which consist of the movie name and VCR commands, the video stream transfer can be performed.

In the Figure 3, the operational diagram is present, where the requested movie is not located in the local region, or all local servers that hold a copy are overloaded. However, server 1.2 which holds the requested movie is overloaded, but it can still serve as a proxy yet. The manager (server 1) forwards the request to its parent (in this case the HE). The HE observes that a copy of the requested movie can be played from server 2 and informing server 2 for this action. Server 2 finds that server 2.1 is capable of playing the movie, i.e., it has a copy of the movie, it has a connection to the private network and its load is acceptable. Finally, the user contacts server 2.1 and requests it to play the movie through server 1.2 (proxy server).

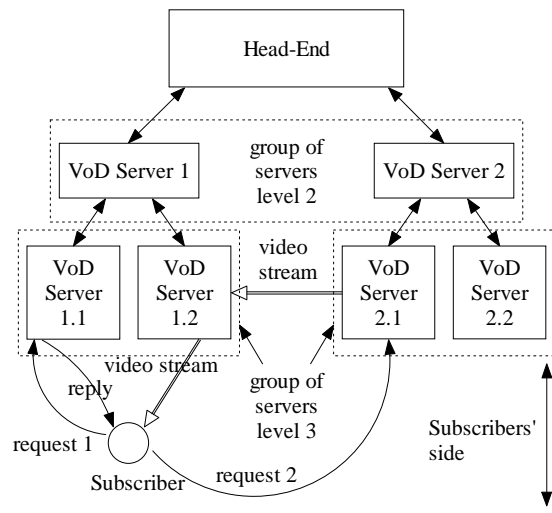


Fig. 3. VoD transfer via proxy

3. ALGORITHMS FOR VIDEO CONTENT DISTRIBUTION

In this work two algorithms which are based on the subscribers' preferences are described which automatically distributes the video content from the head-end to the distribution hubs. The two algo-

rithms are distinguished in terms of using stage the local servers' disk capacity and the requested movie delivering method from video server to the respective subscriber, when the requested movie is missing from the local server. For these algorithms the following abbreviations are introduced: FDUCCA (Full Disk Using Content Distribution Algorithm) and PDUCCA (Partial Disk Using Content Distribution Algorithm).

The diagram on Figure 4 illustrates the algorithms operation.

The DHUBs are set apart in logical zones each one containing one or more DHUBs and serving the subscribers whose video preferences are similar [6]. Initially, the whole video information is recorded onto the central server, then duplicated onto the local servers but only for the movies that are supposed to be most preferred. After that the algorithm keeps on self-learning with the existing data in the network so that the video content in the distribution hubs is updated automatically through specified time period (from one to up to several days, according to the requests intensity).

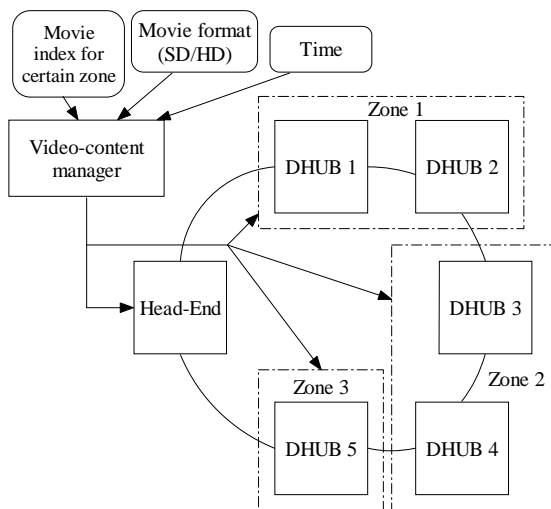


Fig. 4. Operational diagram of the algorithms for video content distribution

The update should be done at a given moment to avoid the risk of blocking the system. The morning period is chosen between 5 AM and 6 AM, when the video traffic intensity is at its minimum for the local servers updating. The update consists of deleting some of the old video content and recording a new one, data about the popularity of each movie being taken into consideration.

It is important to note that to compensate for the different transmission bit rate of the movies in Standard Definition (SD) and High Definition (HD) format the HD format movie index must be multi-

plied by four. Besides, HD-formatted films have a bigger file size if compared with SD movies though their duration in minutes is still the same. Because of that reason the percentage of HD movies with respect to the overall number of films should be considered when the necessary disk space is scheduled.

Information about the movie index is collected and updated case-by-case for each zone. If a movie is requested but the video session duration is less than 20 minutes its movie index is not changed.

When the index of the old video content in the local servers is less than a given threshold it will be deleted and replaced by a new one whose index is above the threshold. The threshold depends on the local servers capacity (the disk space in GBytes).

As it is seen from the analysis in [3] the local servers capacity, in terms of FDUCCA using, has to be chosen in a way not to be less than 23% of the central server capacity at the head-end. With this approach it is guaranteed that at least 80% of the requested movies will be available in the local servers of each zone. If the local servers capacity has not been properly calculated the system would not function efficiently. Smaller capacity causes both a video traffic increase and a risk of system blockage, but on the other hand huge capacity leads to increased equipment expenses.

The local servers' capacity in terms of PDUCCA using is chosen to be 25 % larger for each local server, compared to local server's capacity in terms of FDUCCA using. This 25 % additional disk capacity is reserved for recording the requested movies from other serving zones. In this way the risk of system blockage is decreasing, but the largest disk capacity leads to increased equipment expenses.

The PDUCCA operates as follows: If a movie, which is not recorded at the local server, is requested by the user, this movie is downloading from the other local servers through Peer-to-Peer (P2P) protocol. On that way the multiple information streams with low bit rate are used which leads to minimizing the risk of system blockage compared to proxy server using with high video stream bit rate (3,75 Mbps for SD and about 12,5 Mbps for HD video).

During the movie downloading (this time can be minimized to some minutes with the contemporary high-speed optical transport usage), the subscriber waits. After the video session ends, the movie is deleted from the local server.

In case the local server contains films whose index is equal to 1 or more than 1 (e.g. movies re-

requested at least once), small space of this server will be unused. Onto this unused space the operator will record random films with a zero index. This case is possible in the initial phase of the algorithm operation when the video information gathered is still not enough.

After the local servers is updated with new video content the system must decrease the traffic through the central distribution network in order to reduce the blockage risk.

When a subscriber requests a movie and meets the access conditions the movie transfer starts by the nearest point. Firstly, the system checks for the requested film within the local server, after that in the other DHUBs and finally in the head-end.

The decision for the transfer route depends on the routing protocol. This protocol takes into consideration the number of the points to the movie location and to the subscriber, as well as the traffic into the different system parts.

The video-content manager block can be realized as a software application that will automatically copy and delete movies on the local servers. In that case a criterion must be developed in order to minimize possible mistakes and system blockage. For example, during an existing video session to a certain subscriber the chosen movie must not be deleted. During the video-content update the transfers to subscribers must be avoided. During the server update process the server operates as a transit unit which redirects the requests to the DHUBs or to the head-end in terms of FDUCDA using.

4. ROUTING PROTOCOLS USING IN VOD SYSTEMS

Routing protocols are used in CATV networks for the chosen video stream path determination with its transfer from the video server to subscriber. After the routing protocol takes a decision for the requested video stream path determination, a record in routing table of each router on the video stream path is made.

There are two main types of routing protocols [7-9]:

1) Centralized – the choice for route is made from the main controller, which is located in the HE. This controller updates routing tables of all routers, located in different nodes. The advantage of this type protocols is decreasing the risk of system blockages but disadvantage is their impossibility for large geographic area deployment.

2) Distributed – the main controller is not necessary and the needed information about the route choosing is adopted from other routers through the messages exchange with their adjacent routers. This type routing protocols are realizable in large scale CATV networks. They are the more applicable for the contemporary network realizations.

In terms of CATV networks routing protocol composing, it is needed to take place in account with their three-and-branch topology. The suitable routing protocol realization over the CATV network is illustrated on the Figure 5. It is typical for this protocol that the route choosing is made by each router through sending the requested messages to adjacent router in upstream direction.

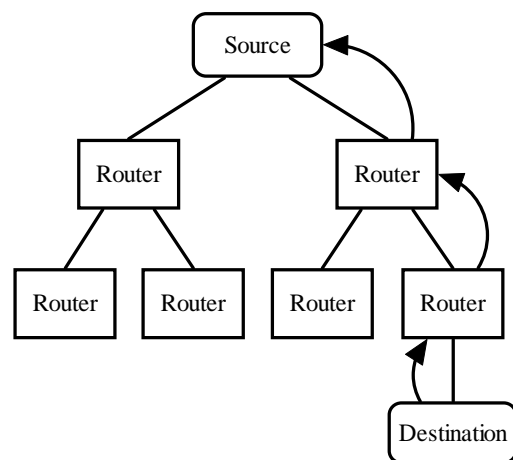


Fig. 5. Routing protocol realization over the CATV networks

The felicitous reason is using the routing protocols as a Border Gateway Protocol (BGP), which can be realized over the large scale networks as a contemporary CATV networks.

These types of routing protocols enable managing as the direct information between two adjacent routers as a transit traffic generating with the proxy servers using.

5. CONCLUSION

In this paper is presented a method for increasing the effectiveness of VoD system, realized over the CATV network. This method consists of optimization the network architecture, video content distribution algorithm and routing protocol.

Two video content distribution algorithms are proposed – FDUCDA and PDUCCA. From their comparison the following conclusions can be made:

1) FDUCDA require smaller local servers' disk capacity for its realization which make this protocol more inexpensive but it is increasing the traffic

across the central transport network, i.e. the risk of system blockage increase too.

2) PDUCCA requires 25 % additional disk capacity, compared to FDUCDA. The advantage is higher reliability, i.e. the lower probability of system blockage but disadvantages are the higher price compared to FDUCDA and more time is needed when subscriber waits for the requested video passing.

It is present a routing protocol building concept over the CATV network, ensuring effective transmission of the requested video streams from the VoD server to subscribers.

References

- [1] C. Bouras, J. Garofalakis, P. Petridis and G. Tzimas, The performance of queuing theoretic video on demand algorithms, 2007.
- [2] Fujitsu Network Communications Inc., Fujitsu Gigabit Ethernet VOD Solutions, USA, 2004. [Online]. Available at: http://www.fujitsu.com/downloads/FNC/Whitepapers/VOD_wp.pdf.
- [3] L. Jordanova, J. Nenkov, Distribution of Video-on-Demand Service over Cable Television Networks, *Journal Radio engineering*, Volume 18, Number 2, June 2009.
- [4] Al Hamra, E. Biersack, G. Urovoy-Keller, Architectural Choices for Video-on-Demand Systems, 2003. [Online]. Available at: <http://2003.iwcw.org/papers/alamra.pdf>
- [5] Roytman, DVS: A System for Distribution and Management of Global Video on Demand Services., Israel Ben-Shaul, Israel Cidon, 1999.
- [6] M. Pasquinilli, S. Nakrani, The Benefits and Challenges of Deploying Large Regional VOD Asset Libraries, *NCTA Technical Papers*, 2008.
- [7] <http://www.cse.buffalo.edu/~qiao/cse620/fall04/adaptive.ppt>.
- [8] Abdullah M. S. Alkahtani, M. E. Woodward and K. Al-Begain, An Overview of Quality of Service (QoS) and QoS Routing in Communication Networks , University of Bradford, UK, 2003.
- [9] <https://cisco.hosted.jivesoftware.com/servlet/JiveServlet/download/4770-2-4102/cisco-360-IGP-Data-Sheet.pdf>.

SPEAKER TRACKING MOBILE ROBOT AUDIO VISUAL SYSTEM FOR SURVEILLANCE APPLICATIONS

Alexander Bekiarski, Snejana Pleshkova-Bekiarska

Technical University – Sofia, Bulgaria
Kliment Ohridski, 8
Tel.: +359 965 3300; E-mail: snegpl@tu-sofia.bg

Abstract

In the mobile robots for security and video surveillance applications exists an audio and visual tracker system. Combining visual and audio data from video cameras and microphones is a more realistic model similar to the human system of seeing and hearing. The proposed method for audio and visual speaker tracking used the results of human body shape determination and audio information from sound localization as direction of sound arrival. An appropriate filter is proposed to combining and integration of audio and visual information to efficiently apply the specifics of audio and visual features.

1. INTRODUCTION

The mobile robot perceives the speaker sounds, process them and determine the speaker localization or the direction of arrival (DOA) of sound [1]. Another complicated task is the speech recognizing or speaker identification, performed from the robot to identified or recognized the talker and then to choose the moving direction [2], [3]. To realize this task it is possible to merge the available audio and video information. For this purpose both audio and video information must be available to avoid the limitations in terms of tracking performance. The sensors providing input data are a video camera for speaker position finding and separation and two microphones for sound from speaker localization. This combination gives as the result better localization and tracking of speaking persons or speakers if it is performed by a decision filter.

2. AUDIO VISUAL MOBILE ROBOT SYSTEM

2.1. System architecture

In the Fig.1 is presented general view of the proposed and tested audio visual robot system for speaker tracking purposes in a surveillance application.

Audio system consists of a microphone array with two microphones M1, M2 and Audio Processing block. Audio Processing block using a Direction of Arrival (DOA) estimation algorithm to determine the speaker sound wave direction in relation of robot position.

The video robot system consists of a single TV camera seeing the speaking person in area of robot

observation and a Video processing block. The Video Processing block perform the decision of the speaker co-ordinates (x_v, y_v) .

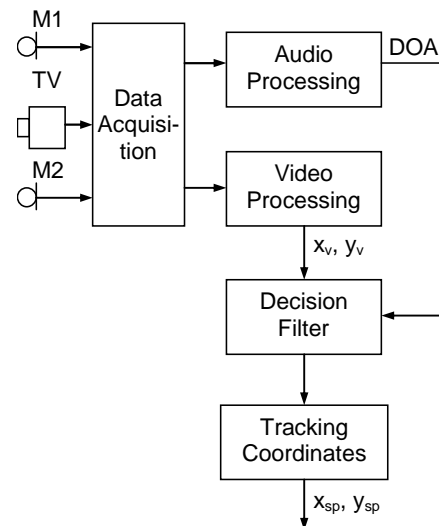


Fig. 1

The information for the speaker from Audio and Video Processing blocks is sent to a Decision Filter, in which it is decided whether or not the values of the pair DOA and (x_v, y_v) are right or correct speaker position.

2.2. Audio Processing

The microphone array gives an estimation of the audio source or speaker location in term of angle θ , which is explained in Fig. 2.

The speech signals $s_1(t)$ and $s_2(t)$ from two spatially separated microphones M1 and M2 are picked up from source signal $s(t)$ corresponding to

the speech wave from the speaker in the presence of noise and can be mathematically written as:

$$s_1(t) = s(t) + n_1(t) \quad (1)$$

$$s_2(t) = \alpha s(t + D) + n_2(t), \quad (2)$$

where:

$n_1(t)$ and $n_2(t)$ are added in the place of microphones M1 and M2, respectively;
 α – amplitude coefficient of attenuation;
 D – time delay between two microphone signals $s_1(t)$ and $s_2(t)$.

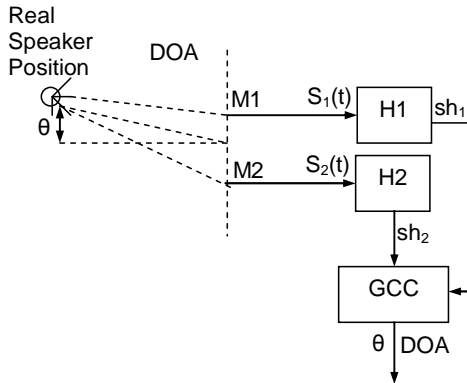


Fig. 2

Let suppose that all signals belong to a set R , the noise signals are random processes and source speech signal $s(t)$ is uncorrelated with noise $n_1(t)$ and $n_2(t)$:

$$s(t), n_1(t) \text{ and } n_2(t) \in R \quad (3)$$

In most of the existing methods determination of the delay D or time offset τ is computed as the cross-correlation or expectation E between two microphone signals $s_1(t)$ and $s_2(t)$:

$$R_{s_1s_2}(\tau) = E[s_1(t)s_2(t - \tau)] \quad (4)$$

For example, if the speech signals can be treated as ergodic processes, the equation (4) can be written as:

$$R_{s_1s_2}(\tau) = \frac{1}{T_2 - T_1} \int_{T_1}^{T_2} s_1(t)s_2(t - \tau)dt, \quad (5)$$

where:

$T_2 - T_1$ is the observation time interval, which for joint audio and video speaker localization must be equal to the video frame period T_{Fr} , related to the frame frequency f_{Fr} :

$$T_2 - T_1 = T_{Fr} = \frac{1}{f_{Fr}}, \quad (6)$$

With the pre-filters, H1 and H2, shown in Fig. 2 the equations for the cross-correlation can be modified as Generalization of Cross-Correlation (GCC):

$$R_{sh_1sh_2}(\tau) = \int_{-\infty}^{+\infty} \psi_g(f) G_{s_1s_2}(f) e^{j2\pi\tau} df, \quad (7)$$

where:

sh_1 and sh_2 are the microphone signals after pre-filters H1 and H2;

$G_{s_1s_2}(f)$ - cross power spectral function between $s_1(t)$ and $s_2(t)$;

$\psi_g(f)$ - general frequency weighing:

$$\psi_g(f) = H_1(f)H_2^*(f) \quad (8)$$

and $H_1(f), H_2(f)$ are the response of the two pre-filters in frequency area.

From the equation (8) is seen, that $\psi_g(f)$ depend on pre-filter $H_1(f), H_2(f)$ transform. Different pre-filtering transforms exists, but one of them phase transform (PHAT) is most used in the applications of DOA estimation and speaker localization. For PHAT transform $\psi_g(f)$ is described as:

$$\psi_g(f) = \frac{1}{|G_{s_1s_2}|} = \frac{1}{|S_1(f)S_2(f)|}. \quad (9)$$

The described Audio Processing block show the necessary operations to achieve the satisfactory precision of the DOA estimation from the robot audio system.

2.3. Video Processing

In the similar way the speaker position (x_{sp}, y_{sp}) is calculated from the TV camera information. This calculation start with the motion detection, separation of binary image mask of the speaker and ended with the pair of co-ordinates (x_v, y_v) calculation as the center of gravity of human body. All of these operations are included in the Video Processing block in the Fig.1.

2.4. Decision filter

Both results (DOA or θ) and (x_v, y_v) from Audio and Video Processing blocks are shown in Fig.1 as input information of Decision Filter, which is chosen as a particle filter. A particle filter represents the unknown probability density function by a set of m-

random samples sp_1, \dots, sp_m . In the case of a speaker tracking system in a 2D area of robot observation each particle sp_i is represented as a hypotheses of speaker location (x_i, y_i) . The particles are considered as the vectors in state space associated with an individual weight W_i , and combined with the real audio and video observation DOA or θ and (x_v, y_v) in a way to decide and estimate the more probably connected observation to the real speaker co-ordinates (x_{sp}, y_{sp}) . The decision particle filter performs two main steps:

- the prediction step to generate new particles from the set of particles in the previous time instance;

- the measurement step to adjust the weights W_i of new particles with respect of current observations DOA_i or θ_i and (x_v^i, y_v^i) .

The continuous execution of these steps is accompanied with calculations of current weights:

$$w_i = c_A \cdot p(A_t / sp_i) + c_V \cdot p(V_t / sp_i), \quad (10)$$

where:

c_A and c_V are dynamic mixture weights;

A_t and V_t – the current audio and video observations, i.e. DOA or θ and (x_v, y_v) , respectively.

The dynamic mixture weights c_A and c_V can be interpreted as confidence measures for the audio and video robot system:

$$c_A = 1 / \sqrt{(\sigma_x^A)^2 + (\sigma_y^A)^2} \quad (11)$$

$$c_V = 1 / \sqrt{(\sigma_x^V)^2 + (\sigma_y^V)^2}, \quad (12)$$

where:

$\sigma_x^A, \sigma_x^V, \sigma_y^A$ and σ_y^V denote the standard deviation of the particle set's x- or y- components, weighted with audio or video scores, respectively.

In order to generate the final speaker tracking output (x_{sp}, y_{sp}) it is used a $m \times m$ window to scan the x,y area of observation and to find the highest accumulated particle scores, which is chosen as final decision of the speaker position (x_{sp}, y_{sp}) .

3. RESULTS OF SIMULATIONS AND CONCLUSION

The proposed algorithm is simulated and tested with a set of audio and video sequences chosen to reveal the properties, advantages and errors with using only video, only audio or combined video and

audio information. The results are summarized in comparative way in Table1. and on the Fig.3 with calculated speaker co-ordinates (x_{sp}, y_{sp}) .

The analysis of the results gives the reason to conclude that the proposed algorithm of speaker tracking robot audio visual system work with an appropriate efficiency and gives little percentage of miss classification.

Table 1

Tracking mode	Missed speakers classification
Video only	14,3 %
Audio only	22,6%
Video + Audio	5.1%

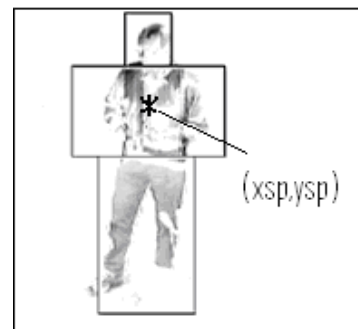
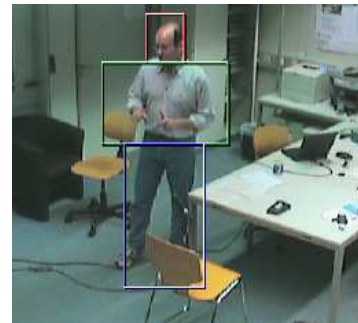


Fig. 3

ACKNOWLEDGMENT

This work was supported by National Ministry of Science and Education of Bulgaria under Contract BY-I-302/2007: "Audio-video information and communication system for active surveillance cooperating with a Mobile Security Robot".

References

- [1] H. Savada, R. Mucai, S. Araki, "Direction of arrival estimation for multiple source signals using independent component analysis", Proc. ISSPA, Paris, France, 2007.
- [2] J. M. Valin, F. Michaud, B. Hadjoui, "Localization of simultaneous moving sound sources for mobile robot using a frequency-domain steered beam former approach", IEEE Proc. Robotics and Automation, pp.236-242, 2006.
- [3] Master, "Speech spectrum modeling from multiple sources", Master Thesis, Cambridge University, Engineering Department Cambridge, England, 2008.

MOVING OBJECTS TRACKING ALGORITHM DESIGN AND TESTING FOR MOBILE ROBOTS

Alexander Bekiarski

Technical University – Sofia, Bulgaria
 Kliment Ohridski, 8
 Tel.: +359 965 3300; E-mail: aabbv@tu-sofia.bg

Abstract

Mobile robot object tracking is a popular method for testing the level of intelligence of a mobile robot. The robot visual system is the means for a mobile robot to interact intelligently and effortlessly with a moving object or a human inhabited environment. The goal here is to design and testing a mobile robot tracking algorithm capable of interfacing intelligently with an object or human in the robot environment or area of observation.

1. INTRODUCTION

Currently one of the most active application in robotic is to observing some moving objects or people in the area of the robot. [1] The proposed algorithm starts with creating a certain background model, subtracting this model from each frame of tracking sequence to find the potential regions of movements [2]. These regions are treated as possible parts of the objects being tracked. Each of these regions is matching with the other regions to define the real place of the object or human tracking from the robot.

2. MOVING OBJECTS TRACKING

The objects in the robot area of observation are usually moving persons in applications like video surveillance [3]. The tracking algorithm of moving person consists of three main parts: motion detection, human body separation, person tracking.

2.1. Motion Detection Algorithm

The first step – motion detection algorithm is presented in the Fig.1.

The current input image frame is $IFr(n)$. One Frame Time delay block is necessary to store the previous image frame $IFr(n-1)$ in a frame memory. Then is calculated Image Absolute Difference IAD between of current and previous frame as:

$$IAD = |IFr(n) - IFr(n-1)| \quad (1)$$

The space and temporal person movements are in the range of low space and temporal frequencies

[2], so the next step in the algorithm presented on the Fig.1 is mark as Low Pass Filter. It is designed as a sliding local $M \times N$ windows with central element i, j moving in the Image Absolute Difference frame IAD with N_x and N_y - the horizontal and vertical image size. The goal is to calculate a value of absolute difference $VAD(i, j)$:

$$VAD(i, j) = \sum_{k=1}^M \sum_{l=1}^N IAD(i-k, j-l) \quad (2)$$

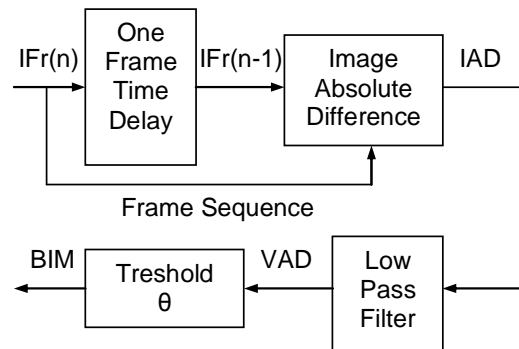


Fig.1. Algorithm for motion detection

The calculated values are compared with a chosen Threshold θ :

$$BIM(i, j) = \begin{cases} 0 & \text{if } VAD < \theta \\ 1 & \text{if } VAD \geq \theta \end{cases} \quad (3)$$

The result is a binary image mask BIM containing values "0" for pixels belonging to the static image regions and values "1" for pixels belonging to the moving image regions.

2.2. Image Frame Pre-filtering

The algorithm on Fig.1 work well if there is not the image intercity changes caused from the fast illumination drifts, noise etc. These changes can lead to some errors of false moving object detection. To overcome these negative effects it is proposed to perform a pre-filtering of each frame $IFr(n)$ using a filter structure presented on the Fig.2.

The goal of the proposed pre-filtration in the Fig.2 is to avoid false motion detection by fast illumination existing in each image frame $IFr(n)$ as a composition of an illumination i and reflectance r :

$$IFr(n) = iIFr(n) + rIFr(n). \quad (4)$$

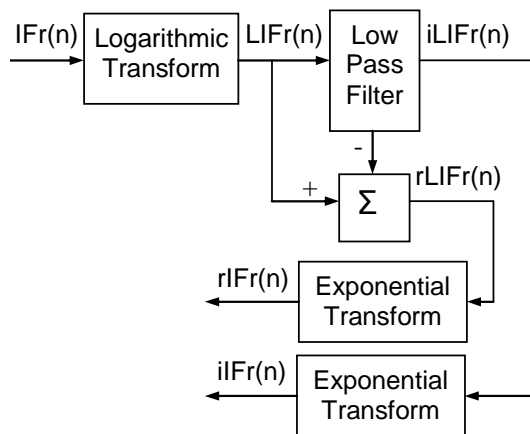


Fig. 2. Frame pre-filtering

An Logarithmic Transform to (4):

$$\begin{aligned} LIFr(n) &= \log IFr(n) = \log(iIFr(n) + rIFr(n)) = \\ &= iLIFr(n) + rLIFr(n). \end{aligned} \quad (5)$$

show that components $iLIFr(n)$ for illumination and $rLIFr(n)$ for reflection are mixed. They can be separated with a Low Pass Filter and a block of addition Σ , using the property of the luminance component $iLIFr(n)$ to contain only the low frequency spectral components:

$$rLIFr(n) = LIFr(n) - iLIFr(n). \quad (6)$$

The separated illumination $iLIFr(n)$ and reflection $rLIFr(n)$ are put under inverse Exponential Transform to output them as two separate components $iIFr(n)$ and $rIFr(n)$.

Only the reflected part $rIFr(n)$ carry the information for the moving objects or persons in the

images. Only this part $rIFr(n)$ is applied as input of the motion detection algorithm on the Fig.1.

2.2. Object or Human Body Separation

The binary image mask BIM, determined as the output in Fig.1. is used in the separation of moving person in area of robot observation. The binary mask in this step is processed with Freeman chain code to describe the object boundary as a set of points with their co-ordinates $x(p)$ and $y(p)$, combined as a complex number:

$$z(p) = x(p) + jy(p), \quad (7)$$

for $p = 0, 1, \dots, P$.

Each closed boundary is with perimeter P .

The discrete Fourier transform of $z(p)$ is given by:

$$a(k) = \frac{1}{P} \sum_{n=0}^{P-1} z(p) \cdot e^{-j2\pi kp/P} \quad (8)$$

for $k = 0, 1, \dots, P-1$.

The complex coefficients $a(k)$ represent the Fourier description of the corresponding boundary. They can be processed to make them invariant of object position and site. The invariant properties are considered as translation, rotation and scaling. The independence of translation and rotation can be achieved by removing DC-components $a(0)$ and by using only magnitude of each $a(k)$ spectral coefficient. The scale invariance is realized by dividing all $a(k)$ by the magnitude of $a(1)$. Also it is made a subtractions of the phase $e^{j\phi_1}$ of coefficient $a(1)$, weighted with "k". This removes the starting point variance. Finally the set of coefficients representing a corresponding boundary with removed variances are:

$$ai(k) = \frac{|a(k)|}{|a(1)|} \cdot e^{-j\phi_1 k} \quad (9)$$

for $k = 2, 3, \dots, P-1$.

There is an other way to boundary representation as the distance $d(p)$ of the boundary points $x(p)$, $y(p)$ to the objects or person centre of gravity (x_c, y_c) :

$$d(p) = \left((x(p) - x_c)^2 + (y(p) - y_c)^2 \right)^{1/2}. \quad (10)$$

Using Fourier transform for the distance $d(p)$ gives:

$$b(k) = \frac{1}{P} \sum_{p=0}^{P-1} d(p) e^{-j2\pi kp/P} \quad (11)$$

for $k = 0, 1, \dots, P-1$.

The advantage of second method is the real value of $d(p)$ in equation (10), which gives the possibility to calculate and use only half of description $b(k)$ from equation (11). Also the subtraction of the centre of gravity represent the position of the shape, i.e. the distance $d(p)$ is invariant to translation. The other invariance properties are achieved in a similar way (equation (9)) to the first method:

$$bi(k) = \frac{|b(k)|}{|b(0)|} \quad (12)$$

for $k = 0, 1, \dots, P-1$.

For the moving objects or persons detection and tracking it is sufficiently to use only low frequency components from (9) or (12), for example first 10 coefficients in the object or person classification task.

2.3. Classification of Moving Object

For a precise separation only of moving human body from all moving objects it is performed an object classification with an appropriate feed-forward neural network, which is proposed and tested as a four layers type for the neural network.

The network consists of four layers:

- input layer with number of chosen fetures;
- two hidden layers with number of neurons chosen in the time of testing as seven neurons;
- one output layer with one neuron per class of the objects.

The activation function is chosen as a sigmoid and the training algorithm is well known back-propagation method.

3. EXPERIMENTAL RESULTS AND CONCLUSION

The proposed algorithm of moving object or human, tracking with a mobile robot is simulated and tested with some chosen images with objects like cars, persons, and landscape, shown in Fig.3.

The experiments are carried out with the described algorithm of moving objects detection and their classification with the four layer neural network. The network is trained with the set of objects type: human, cars and landscapes, shown in Fig.3, which are divided as training and testing images.

The simulation gives the correct classification. Each objects, as it is shown in fig.3, is separated with a rectangle to show the correct classifications for the chosen types of moving objects human and cars. The landscape type is rejected, which is also an example of the ability of the proposed algorithm to recognize false moving objects.



Fig.3. The separated human, vehicle and rejected false moving objects

The results in the Table 1 are summarized and shown as a compartment of two methods for invariant properties (equations 9 and 12).

The great percentage of correct moving object classification is a guaranty of the efficiency of using and future improvements of the developed and tested algorithm.

Table 1

Method	Equation (9)		Equation (12)	
	human	vehicle	human	vehicle
Number of objects	777	463	773	456
Correct Classification	745	452	672	436
Miss Classification	32	11	101	20
Correct %	96	98	87	96

ACKNOWLEDGMENT

This work was supported by National Ministry of Science and Education of Bulgaria under Contract BY-I-302/2007: "Audio-video information and communication system for active surveillance co-operating with a Mobile Security Robot".

References

- [1] J. Fritsch, M. Kleinhagenbrock, S. Lang "Audiovisual person tracking with a mobile robot", in Proc. Int. Conf. on Intelligent Autonomous System, pp. 898-906, IOS Press, 2004.
- [2] T. Aach, A. Kaup, and R. Mester. Statistical model-based change detection in moving video. *Signal Processing*, 31(2):165-180, 2008.
- [3] Taneva L., Development system with microcontroller MSP430F149 for education, FMNS, 2005, Blagoevgrad, Vol. 1, pp. 175 – 180.

RADIATION OF ELECTRIC AND MAGNETIC DIPOLES IN UNIAXIAL MAGNETIC CRYSTAL MEDIA

Seil Sautbekov* and Panayiotis Frangos**

*Euroasian National University, ,
5, Munaitpassova Str. 010008 Astana, Kazakhstan, E-mail: sautbek@mail.ru

**Division of Information Transmission Systems and Materials Technology,
School of Electrical and Computer Engineering,
National Technical University of Athens
9, Iroon Polytechniou Str., 157 80 Zografou,
Athens, GREECE,
Tel. +30 210 772 3694 ; FAX +30 210 772 2281, E-mail pfrangos@central.ntua.gr

Abstract

The problem of radiation of arbitrarily distributed currents in boundless uniaxial magnetic crystal media is considered through the method of generalized solutions of the system of Maxwell's equations in an exact form. The solution resolves into two independent solutions. The first corresponds to the isotropic solution for currents directed along the crystal axis, while the second corresponds to the anisotropic solution when the currents are perpendicular to the axis. Through the use of the expressions for current density of the point magnetic and electric dipoles using delta-function representations, the formulae for the radiated electromagnetic waves, as well as the corresponding radiation patterns, are derived. The obtained solution in the anisotropic case yields the well – known solutions for the isotropic case as a limiting case. Furthermore, the numerical calculation of the solution of Maxwell's equations shows that it satisfies the energy conservation law, i.e. the time average value of energy flux through the surface of a sphere with a point dipole placed at its center remains independent of the radius of the sphere. The obtained generalized solutions of the Maxwell's equations are valid for any values of the elements of the permeability tensor, as well as for sources of the electromagnetic waves described by discontinuous and singular functions.

1. INTRODUCTION

Anisotropic materials have found wide application in the microcircuits working on ultrahigh frequencies. Thin films from monocrystals are effectively used as waveguide's systems.

The problem of radiation of an elementary electric dipole in uniaxial infinite crystal was considered in Ref. [1] with the help of the theory of the generalised functions. The present work is continuation for a case of a magnetic dipole. There are the electromagnetic field and the directivity diagrams of the point magnetic dipole is considered.

2. SOLUTION OF MAXWELL'S EQUATIONS FOR UNIAXIAL ANISOTROPIC MEDIUM

Maxwell's equations for uniaxial anisotropic electromagnetic media of stationary processes are:

$$\begin{cases} \text{rot } E - i\omega \cdot B = 0, \\ \text{rot } H + i\omega \cdot D = j, \end{cases} \quad (1)$$

which is possible to be presented in matrix form:

$$\mathbf{M}\mathbf{U} = \mathbf{J}, \quad (2)$$

where

$$\mathbf{M} = \begin{pmatrix} -i\omega\epsilon\epsilon_0\mathbf{I} & \mathbf{G}_0 \\ \mathbf{G}_0 & i\omega\hat{\mu}\mu_0 \end{pmatrix}, \quad \mathbf{U} = \begin{pmatrix} E \\ H \end{pmatrix},$$

$$\mathbf{E} = \begin{pmatrix} E_x \\ E_y \\ E_z \end{pmatrix}, \quad \mathbf{H} = \begin{pmatrix} H_x \\ H_y \\ H_z \end{pmatrix}, \quad \mathbf{J} = \begin{pmatrix} j \\ \mathbf{0} \end{pmatrix},$$

$$\mathbf{j} = \begin{pmatrix} j_x \\ j_y \\ j_z \end{pmatrix}, \quad \mathbf{0} = \begin{pmatrix} 0 \\ 0 \\ 0 \end{pmatrix}, \quad \hat{\mu} = \begin{pmatrix} \mu & 0 & 0 \\ 0 & \mu & 0 \\ 0 & 0 & \mu_1 \end{pmatrix},$$

where ω is the constant frequency of electromagnetic field, \mathbf{M} is Maxwell's operator, \mathbf{I} is a identity matrix 3x3, \mathbf{E} , \mathbf{H} are the intensity of electric and magnetic fields, \mathbf{J} is vector of current density.

In magnetically anisotropic media the relation between induction and intensity of the magnetic field is:

$$\mathbf{B} = \mu_0\hat{\mu}\mathbf{H}$$

and vector of electric induction:

$$\mathbf{D} = \epsilon\epsilon_0\mathbf{E}.$$

3. SOLUTION OF THE PROBLEM

A method based on the theory of the generalized function of the Fourier transformation is used for solving the matrix equation (2) [1]:

$$\begin{aligned}\tilde{\mathbf{E}}(\mathbf{k}) &= \mathbf{F}[\mathbf{E}(\mathbf{r})] = \int_{\mathbf{R}^3} \mathbf{E}(\mathbf{r}) \exp(-i\mathbf{k}\mathbf{r}) dV \\ \mathbf{F}^{-1}[\tilde{\mathbf{E}}(\mathbf{k})] &= \frac{1}{(2\pi)^3} \int_{\mathbf{R}^3} \tilde{\mathbf{E}}(\mathbf{k}) \exp(i\mathbf{k}\mathbf{r}) d^3k\end{aligned}$$

where

$$d^3k = dk_x dk_y dk_z.$$

By means of direct Fourier transformation we write down the system of equations (1) or (2) in matrix form:

$$\tilde{\mathbf{M}}\tilde{\mathbf{U}} = \tilde{\mathbf{J}}. \quad (3)$$

The solution of this problem is reduced to the solution of the system of the linear algebraic equations (4), where $\tilde{\mathbf{U}}$ is defined by means of inverse matrix $\tilde{\mathbf{M}}^{-1}$:

$$\tilde{\mathbf{U}} = \tilde{\mathbf{M}}^{-1}\tilde{\mathbf{J}}. \quad (4)$$

By introducing new functions according to

$$\begin{aligned}\tilde{\Psi}_0 &\stackrel{\text{def}}{=} \frac{1}{k_0^2 - k_x^2 - k_y^2 - k_z^2}, \\ \tilde{\Psi}_1^m &\stackrel{\text{def}}{=} \frac{1}{k_n^2 - k_x^2 - k_y^2 - \frac{\mu_1}{\mu} k_z^2}, \\ \tilde{\Psi}_2^m &\stackrel{\text{def}}{=} \left(\frac{\mu_1}{\mu} - 1 \right) \tilde{\Psi}_1^m \tilde{\Psi}_0\end{aligned} \quad (5)$$

the components of the electromagnetic field after transformations in image space can be written as follows:

$$\tilde{\mathbf{E}} = -\frac{i}{\varepsilon\varepsilon_0\omega} (k_0^2 \{ \tilde{\mathbf{j}} \tilde{\Psi}_0 + [\mathbf{k}, \mathbf{e}_z [\mathbf{k}, \tilde{\mathbf{j}}_\perp]_z] \Psi_2^m \} - \mathbf{k}(\tilde{\mathbf{k}}\tilde{\mathbf{j}}) \tilde{\Psi}_0), \quad (6)$$

$$\tilde{\mathbf{H}} = i(k_z - \mathbf{k})k_z [\mathbf{k}, \tilde{\mathbf{j}}_\perp]_z \tilde{\Psi}_2^m + i\mathbf{e}_z [\mathbf{k}, \tilde{\mathbf{j}}_\perp]_z (\tilde{\Psi}_0 - \tilde{\Psi}_1^m) - i[\mathbf{k}, \tilde{\mathbf{j}}] \tilde{\Psi}_0, \quad (7)$$

where

$$\begin{aligned}\tilde{\mathbf{j}}_0 &= (0, 0, \tilde{j}_z), \quad \tilde{\mathbf{j}}_\perp = (\tilde{j}_x, \tilde{j}_y, 0), \\ k_0^2 &= \omega^2 \varepsilon_0 \varepsilon \mu \mu_0, \quad k_n^2 = k_0^2 \mu_1 / \mu.\end{aligned}$$

After the inverse Fourier transformations from (6) and (7) we obtain:

$$\mathbf{E} = -\frac{i}{\varepsilon_0 \varepsilon \omega} ((k_0^2 + \text{grad div}) \mathbf{j} * \Psi_0 - k_0^2 \text{rot}(\mathbf{e}_z (\mathbf{e}_z \text{rot} \mathbf{j}_\perp)) * \Psi_2^m), \quad (8)$$

$$\mathbf{H} = (k_0^2 \mathbf{e}_z + \frac{\partial}{\partial z} \text{grad}) \text{rot}_z \mathbf{j}_\perp * \Psi_2^m - \text{rot} \mathbf{j} * \Psi_0. \quad (9)$$

This solution can be written in the form of the sum of two solutions:

$$\mathbf{E} = \mathbf{E}_1 + \mathbf{E}_2, \quad \mathbf{H} = \mathbf{H}_1 + \mathbf{H}_2.$$

It should be noted that the first of them is the 'isotropic' solution. It is defined by Green's function Ψ_0 and the density of the current \mathbf{j}_0 directed endwise the axis z (of the anisotropy):

$$\begin{cases} \mathbf{E}_1 = -\frac{i}{\varepsilon_0 \varepsilon \omega} (\text{grad div} + k_0^2) (\Psi_0 * \mathbf{j}_0), \\ \mathbf{H}_1 = -\text{rot}(\Psi_0 * \mathbf{j}_0), \end{cases} \quad (10)$$

where the Green's function Ψ_0 can be defined from (5) by inverse Fourier transformation [1]

$$\Psi_0 = \mathbf{F}^{-1}[\tilde{\Psi}_0] = -\frac{1}{4\pi} \frac{\exp(ik_0 r)}{r}, \quad (11)$$

$$r = \sqrt{x^2 + y^2 + z^2}.$$

The second solution can be written by using the component of the density of the current \mathbf{j}_\perp perpendicular to axis z and the Green's functions Ψ_0 and Ψ_2^m :

$$\begin{cases} \mathbf{E}_2 = -\frac{i}{\varepsilon_0 \varepsilon \omega} ((k_0^2 + \text{grad div}) \mathbf{j}_\perp * \Psi_0 - k_0^2 \text{rot}(\mathbf{e}_z \text{rot}_z \mathbf{j}_\perp) * \Psi_2^m), \\ \mathbf{H}_2 = (k_0^2 \mathbf{e}_z + \frac{\partial}{\partial z} \text{grad}) \text{rot}_z \mathbf{j}_\perp * \Psi_2^m - \text{rot} \mathbf{j}_\perp * \Psi_0. \end{cases} \quad (12)$$

$$\Psi_1^m = -\frac{1}{4\pi} \sqrt{\frac{\mu}{\mu_1}} \frac{\exp(ik_n r')}{r'}, \quad (13)$$

$$r' = \sqrt{x^2 + y^2 + \frac{\mu}{\mu_1} z^2},$$

$$\Psi_2^m = (\mu_1 / \mu - 1) \Psi_0 * \Psi_1^m \quad (14)$$

or

$$\Psi_2^m = \frac{1}{i8\pi k_0} [e^{ik_0 z} (\text{Ci}(k_0(r-z)) + iS i(k_0(r-z))) + e^{-ik_0 z} (\text{Ci}(k_0(r+z)) + iS i(k_0(r+z))) - e^{ik_0 z} (\text{Ci}(k_n r' - k_0 z) + iS i(k_n r' - k_0 z)) - e^{-ik_0 z} (\text{Ci}(k_n r' + k_0 z) + iS i(k_n r' + k_0 z))],$$

where integral cosine and sine are defined by formulae's:

$$\text{Ci}(z) = \gamma + \ln z + \int_0^z \frac{\cos t - 1}{t} dt,$$

$$\text{Si}(z) = \int_0^z \frac{\sin t}{t} dt - \frac{\pi}{2}$$

and Euler's constant $\gamma = 0,5772$.

4. RADIATION PATTERNS OF HERTZIAN RADIATOR

The moment of point electric dipole is given by

$$\mathbf{p} = n p e^{-i\omega t} \quad (\mathbf{p} = \mathbf{p}_0 + \mathbf{p}_\perp), \quad (15)$$

where p is a constant. It corresponds to the current density defined by means of the Dirac delta-function:

$$\mathbf{j} = -i\omega \cdot \mathbf{p} \delta(\mathbf{r}). \quad (16)$$

The expression of the electromagnetic field for electric radiator will take the following form as for isotropic medium, when the direction of the dipole moment is parallel to the axis z ($\mathbf{p} = \mathbf{p}_0$) (Fig.1):

$$\begin{cases} \mathbf{E}_1 = -(\varepsilon_0 \varepsilon)^{-1} (\text{grad div} + k_0^2) (\Psi_0 \mathbf{p}_0), \\ \mathbf{H}_1 = i\omega \cdot \text{rot}(\Psi_0 \mathbf{p}_0). \end{cases}$$

Also when the direction of the dipole moment is perpendicular to the axis z , we obtain ($\mathbf{p} = \mathbf{p}_\perp$) (Fig. 2):

$$\begin{cases} \varepsilon_0 \varepsilon \mathbf{E}_2 = k_0^2 \text{rot}(\mathbf{e}_z \text{rot}_z \mathbf{p}_\perp \Psi_2^m) - (k_0^2 + \text{grad div})(\mathbf{p}_\perp \Psi_0), \\ \mathbf{H}_2 = (k_0^2 \mathbf{e}_z + \frac{\partial}{\partial z} \text{grad}) \text{rot}_z (\mathbf{p}_\perp \Psi_2^m) - \text{rot}(\mathbf{p}_\perp \Psi_0). \end{cases}$$

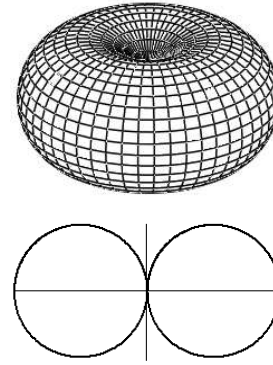


Fig. 1. Directional diagrams (DD). The dipole moment is parallel to the axis z ($\mathbf{p} = \mathbf{p}_0$).

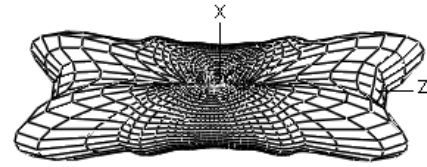


Fig. 2. DD. The axis of electric dipole is perpendicular to axis z ($\mathbf{p} = \mathbf{p}_\perp$), $\mu_1 / \mu = 9$.

5. RADIATION PATTERN OF POINT MAGNETIC DIPOLE MOMENT

On the basis of the obtained results, we consider now radiation of point magnetic dipole moment. For a point radiator with the oscillating magnetic dipole moment, similarly to the electric dipole case, we have:

$$\mathbf{m} = n m \exp(-i\omega \cdot t)$$

$$(\mathbf{m} = \mathbf{m}_0 + \mathbf{m}_\perp, m = \text{const})$$

the electric current density is defined by using Dirac's delta-function:

$$\mathbf{j} = -[\mathbf{m}, \nabla] \cdot \delta(\mathbf{r}). \quad (17)$$

(i) Case $\mathbf{m} = \mathbf{m}_0$:

Relation between density of the electric current j_\perp and the magnetic dipole moment is defined as following, in the case that the magnetic dipole moment \mathbf{m} is directed lengthwise z -axis:

$$\mathbf{j}_\perp = m_0 \left(\mathbf{e}_x \frac{\partial}{\partial y} - \mathbf{e}_y \frac{\partial}{\partial x} \right) \delta(\mathbf{r}). \quad (18)$$

It should be noted that the following useful formulae hold:

$$\text{div } \mathbf{j}_\perp = 0, \quad \mathbf{j}_0 = 0. \quad (19)$$

Taking into account Eq. (19), intensities of the electromagnetic field by the magnetic dipole moment are defined from the solutions (12) in this case, as following:

$$\begin{cases} \mathbf{E} = \frac{k_n^2 m_0}{i \varepsilon \varepsilon_0 \omega} \text{rot}(\mathbf{e}_z \Psi_1^m), \\ \mathbf{H} = m_0 \Delta \Psi_1^m + m_0 \left(\frac{\mu_1}{\mu} - 1 \right) \frac{\partial^2}{\partial z^2} \Psi_1^m - \\ m_0 \frac{\mu_1}{\mu} \frac{\partial}{\partial z} \text{grad } \Psi_1^m. \end{cases} \quad (20)$$

(ii) Case $\mathbf{m} = \mathbf{m}_\perp$:

For the point magnetic dipole moment \mathbf{m}_\perp which is perpendicular to axis z we define intensities of electromagnetic field as following (Fig. 4):

$$\begin{cases} \mathbf{E} = i \frac{k_0^2}{\varepsilon \varepsilon_0 \omega} \left\{ \frac{\partial}{\partial z} ([\mathbf{m}_\perp, \mathbf{e}_z] \frac{\mu_1}{\mu} \Psi_1^m - \text{grad}_\perp \right. \\ \left. \text{rot}_z(\mathbf{m}_\perp \Psi_2^m) \right) - \mathbf{e}_z \text{rot}_z(\mathbf{m}_\perp \Psi_0) \}, \\ \mathbf{H} = (k_0^2 \mathbf{e}_z + \frac{\partial}{\partial z} \text{grad}) \frac{\partial}{\partial z} \text{div } \mathbf{p}_\perp \Psi_2^m - \\ \text{rot rot}(\mathbf{p}_\perp \Psi_0). \end{cases} \quad (21)$$

Directional diagrams are represented in Figs. 3, below :

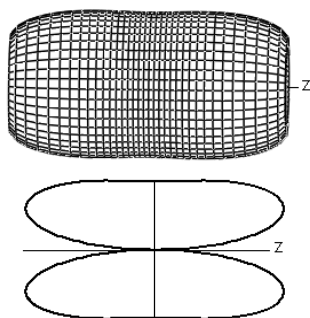


Fig. 3. DD. The axis of magnetic dipole is parallel to axis z ($\mathbf{m} = \mathbf{m}_0$).

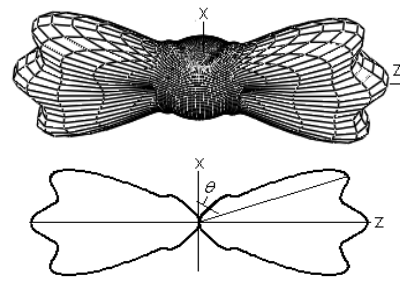


Fig. 4. DD. The axis of magnetic dipole is perpendicular to axis z , $\mu_1 / \mu = 7$.

6. CONCLUSION

The numerical calculation of the solution of Maxwell's equations satisfies the energy conservation law. Numerical computation shows that time average value energy flux on a surface of sphere from a point dipole remains independent from its radius.

As shown in the electric dipole directional diagrams, medium becomes isotropic for such radiator if its moment is directed along anisotropy axis. The dipole pattern in isotropic media is shown in Fig. 1 and directional diagram itself possesses the rotation symmetry. However, the point magnetic moment does not possess such property.

References

- [1] Sautbekov S., Kanymgazieva I., Frangos P. The generalized solutions of Maxwell equations for the uniaxial crystal // *Journal of Applied Electromagnetism (JAE)*. – 2008. – Vol. 10, No. 2. – P. 43–55.
- [2] Vladimirov V.S. The equations of mathematical physics, Nauka. – 1988.
- [3] Alekseyeva L.A. and Sautbekov S.S. Fundamental Solutions of Maxwell's Equations // *Diff. Uravnenia*. – 1999. – Vol. 35, No. 1. – P. 125-127.
- [4] Alekseyeva L.A. and Sautbekov S.S. Method of Generalized Functions For Solving Stationary Boundary Value Problems For Maxwell's Equations // *Comput. Math. and Math. Phys.* – 2000. Vol. 40, No. 4. – P. 582-593.

NOISE REDUCTION AND ENHANCEMENT OF COMPUTED TOMOGRAPHY IMAGES

Veska M. Georgieva

Faculty of Telecommunication, Technical University of Sofia, Bulgaria
1000 Sofia, "Kl. Ohridsky" str.8

T. (+359 2) 965-3998; E-mail: vesg@tu-sofia.bg

Abstract

Computed tomography (CT) presents images of cross-sectional slices of the body. The quality of CT images varies depending on penetrating X-rays in a different anatomically structures. This noise is not independent of the signal. It's Poisson distributed and independent of the measurement noise.

In the paper is proposed a new and effective approach for CT image enhancement. The complex processing has an effect of contrast enhancement, noise reduction and contours determination for selected ROI of different parts of diagnostic CT images. The implemented studying and obtained results by using of real images attempt to make diagnostic more precise.

1. INTRODUCTION

CT images have a lower resolution as X-ray images, typically 512x512 pixels in digital format. The quality of CT images varies depending on penetrating X-rays in a different anatomically structures. The noise problem arises from the fundamentally statistical nature of photon production. The quantum noise is dominant and comes from the quantization of energy into photons. This noise is not independent of the signal. It's Poisson distributed and independent of the measurement noise [1]. We cannot assume that, in a given pixel for 2 consecutive but independent observation intervals of length T , the same number of photons will be counted. The measurement noise is additive Gaussian noise and usually negligible relative to the quantum noise. It comes from the motion of patient [1].

Image enhancement is one of the categories of image processing, attempt to make diagnostic more obvious. In this work is presented an approach for selecting regions of interest, increasing the image contrast for selected ROI and noise suppression and detail preservation abilities of the selected ROI, based on morphological processing and wavelet transformations. By properly choosing of opening, closing filtration and top & bottom hat filtration and suitable form of structuring element, local structures can be eliminated or local geometry of the investigated object can be modified [2]. The reduction of noise components is made on the base of 2D wavelet packet transformations. To improve the diagnostic quality of the selected object are optimized some

parameters of the wavelet transforms such as: determination of the wavelet packet function, determination of best shrinkage decomposition, threshold of the wavelet coefficients and value of the penalized parameter of the threshold. In the paper are analyzed some quantitative estimation parameters: Coefficient of noise reduction (CNR), Signal to noise ratio in the noised image (SNR_Y), Signal to noise ratio in the filtered image (SNR_F), Effectiveness of filtration (E_{FF}), Peak signal to noise ratio (PSNR) [3].

2. STAGES FOR CT IMAGES PROCESSING

Image enhancement techniques are applied to real digital grayscale CT images of the head and abdominal tissues that exhibited diverse pathology.

In this paragraph are presented the three basic stages of the algorithm, used to improve image quality.

The first stage in CT image processing is to define a ROI from the image. It can be selected in interactive procedure from the operator. The result of ROI image is written in a file format that can be used in next processing.

The second stage is increasing the contrast. For that step is necessary first to increase the gray level contrast between the pixels, using gamma correction. This procedure can be applied to Y component of the selected image that is processing in YUV system. The next step in the processing included morphological operators: opening, closing and top & bottom hat filtering, which are used to enhance

contrast in the image. The morphological operators are compared together and one of them is estimated as a most effective method. The top & bottom hat method is a well-suited. It increased the contrast of the object by means of increasing the details in the dark regions and near by contours. The top & bottom hat filtering extracts the original image from the morphologically closed version of the image. For this operation is used a disk-shaped structuring element.

The third stage of the algorithm is noise reduction. It is based on the wavelet packet methods. The wavelet packet analysis is a generalization of wavelet decomposition that offers a richer image analysis. Based on the organization of the wavelet packet library, it can be determinate the decomposition issued from a given orthogonal wavelets. A signal of length $N = 2^L$ can be expand in α different ways, where α is a number of binary sub trees of a complete binary tree of a depth L . The result is $\alpha \geq 2^{N/2}$ [4]. As this number may be very large, it is interesting to find an optimal decomposition with respect to a conventional criterion. The classical entropy-based criterion is a common concept. It's looking for minimum of the criterion from three different entropy criteria: the energy of the transformed in wavelet domain image, entropy by Shannon and the logarithm of the entropy by Shannon [5]. By looking for best shrinkage decomposition to noise reduction two important conditions must be realized together [6]. The conditions (1) and (2) are following:

$$E_K(S) = \min, \text{ for } K = 1, 2, 3, \dots, n \quad (1)$$

where E_K is the entropy in the level K for the best tree decomposition of the image s

$$s_{ij} \geq T \quad (2)$$

where s_{ij} are the wavelet coefficients of S in an orthonormal basis, T is the threshold of the coefficients.

By determination of the threshold it is used the strategy of Birge-Massart [7]. This strategy is flexibility and used spatial adapted threshold that allows to determinate the threshold in three directions: horizontal, vertical and diagonally. In addition the threshold can be hard or soft. The noise reduction is applied on Gaussian and Poison distributed noise components.

3. EXPERIMENTAL RESULTS

The formulated stages of processing are realized by computer simulation in MATLAB environment by using IMAGE PROCESSING TOOLBOX and WAVELET TOOLBOX. In analysis are used 20 grayscale CT images of the head and abdominal tissues that exhibited diverse pathology.

The obtained average results from simulation are presented in Table1.

The best results are obtained by noise reduction of Poisson noise on the base of WP transformation. The CNR is minimum (0.3) and shows that the noise is three times reduced. The values of PSNR and Effectiveness of filtration (E_{FF}) are more sufficient.

Table 1. Simulations results

CT image Processing	PSNR [dB]	SNR _y [dB]	SNR _F [dB]	E _{FF} [dB]	CNR
Contrast increasing and morph filtering	20.7803	17.4120	18.0297	0.6177	0.8423
Gaussian noise reduction with WPT	30.4624	18.0297	19.6728	1.6431	0.5321
Poisson noise reduction with WPT	32.2139	18.0297	20.2342	2.3442	0.3435

The graphical presentations of the obtained results for PSNR are shown on Figure 1.

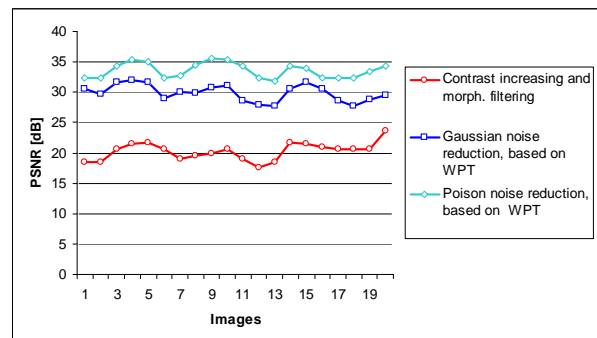


Fig. 1. The graphical presentation of PSNR for investigated CT images

The graphical presentations of the obtained results for E_{FF} are shown on Figure 2.

The graphical presentations of the obtained results for CNR are shown on Figure 3.

On Figure 4 is illustrated the original CT image of size 832x659 pixels.

Figure 5 presents selected ROI from the original CT image of size 196x152 pixels. In Figure 6 is

shown the selected ROI with contrast increasing. In Figure 7 is presented the result from the following wavelet filtration of Gaussian noise. Figure 8 illustrates the following wavelet filtration of Poison noise.

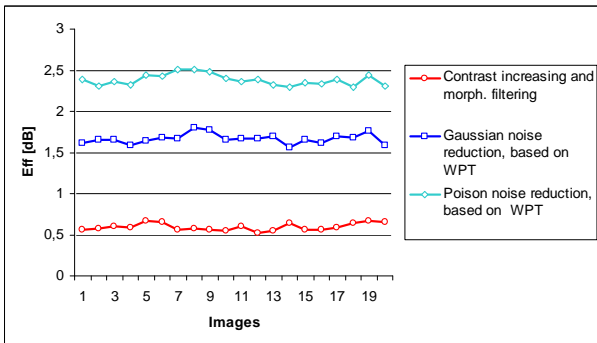


Fig. 2. The graphical presentation of E_{FF} for investigated CT images

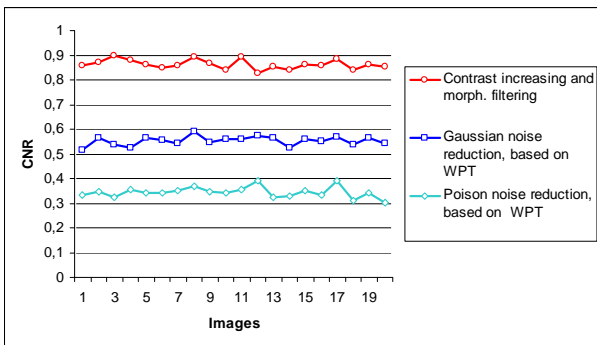


Fig. 3. The graphical presentation of CNR for investigated CT images

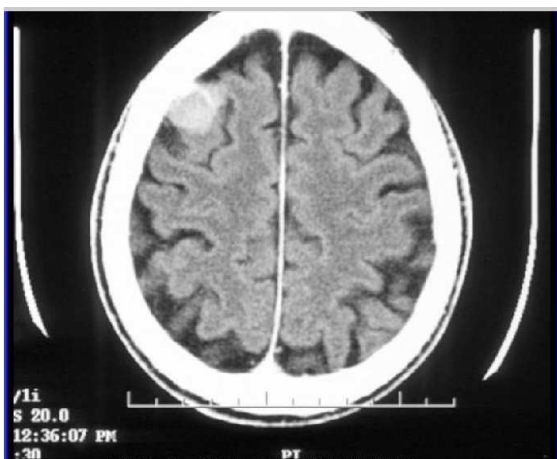


Fig. 4. The original CT image



Fig. 5. The ROI of CT image



Fig. 6. The ROI of CT image with increased contrast

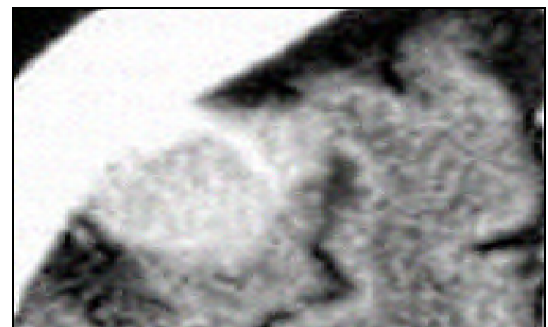


Fig. 7. The ROI of CT image after Gaussian noise reduction



Fig. 8. The ROI of CT image after Poison noise reduction

The obtained result shows that this approach is more effectiveness by image enhancement and noise reduction of Poison noise.

4. CONCLUSION

In the paper is proposed a new and effective approach for CT image enhancement and noise reduction of different type of noises. The complex processing has an effect of contrast enhancement, noise reduction and contours determination for selected ROI of different parts of diagnostic CT images. The implemented studying and obtained results by using of real images attempt to make diagnostic more precise. The proposed approach can be demonstrated by studying of medical image processing in engineering and medical education.

5. ACKNOWLEDGMENTS

I acknowledge to physicians from Medical center PanSanus, Sofia for providing of all CT images data used in experiments and shown also in Figure 4.

References

- [1] M. Smith, A. Docef, "Transforms in telemedicine applications", Kluwer Academic Publishers, 1999.
- [2] T. Athanasiadis, M. Wallace, K. Kapouzis, S.Kollias," Utilization of evidence theory in the detection of salient regions in successive CT images", Oncology reports, Vol.15, 2006, pp.1071-1076
- [3] R.Gonzalez, R. Woods, Digital Image Processing, Addison Wesley Publishing, 1992.
- [4] D.Donoho, I. Johnston, "Adapting to unknown smoothness via wavelet shrinkage", Am. Stat. Assoc., 1995, 90:1200-1224
- [5] R. Coifmann, M. Wickerhauser, "Entropy based Algorithms for best basis selection", IEEE Transaction on information theory, Vol.38, 1992, pp.713-718.
- [6] V.Georgieva, R. Kountchev, "An influence of the wavelet packet decomposition on noise reduction in ultrasound images", Proceedings of ICEST'06, Sofia, Bulgaria, 2006, pp.185-188.
- [7] MATLAB, User's Guide, www.mathwork.com

GUI FOR MORPHOLOGICAL PROCESSING OF MEDICAL IMAGES

Veska M. Georgieva

Faculty of Telecommunication, Technical University of Sofia, Bulgaria
1000 Sofia, "Kl. Ohridsky" str.8
T. (+359 2) 965-3998; E-mail: vesg@tu-sofia.bg

Abstract

In the paper is presented software for morphological processing of medical images and its graphic user interface (GUI). It works in the MATLAB environment and uses IMAGE TOOLBOXES defined functions. Different morphological operators and types of structuring elements with different sizes can be used, regarding to process different medical modalities of the images. The software can realize repeatedly a nonlinear filtration, by using the same operation. The GUI proposes also an interactive option to choose the type of the morphological operation, the type of the structuring element and also its parameters.

The proposed GUI can be applied to real medical images attempt to make diagnostic more precise. The presented GUI is suitable also to engineering education for studying of this processing.

1. INTRODUCTION

The most popular technologies are ultrasound (US), X-rays, Computed tomography (CT) and Magnetic resonance imaging (MRI). These images provide important anatomical information to physicians and specialist upon which can be made diagnoses [1]. The goals of medical image morphological processing include improvement of the visibility and perceptibility of the various regions and tasks such as cleaning the medical image from specific types of noise.

By properly choosing of different type of operation such as: erosion, dilatation, opening, closing, motion blur filtration and top & bottom hat filtration, and suitable form of structuring element, local structures can be eliminated or local geometry of the investigated object can be modified [2].

The software is created in MATLAB 6.5 environment by using IMAGE PROCESSING TOOLBOX.

The graphic user interface consists of checkboxes, buttons, edit boxes, pop-up controls, which make it easy to use. Users enter or choose input data in a single form, because input information changes and visualizations are easier and faster in this way.

The applied algorithm calculates also some objective quantitative estimation parameters as: Coefficient of noise reduction (CNR), Signal to noise ratio in the noised image (SNR_Y), Signal to noise ratio in the filtered image (SNR_F), Effectiveness of filtration (E_{FF}), Peak signal to noise ratio (PSNR)

[3]. On the base of their analysis can be selected the most suitable morphological operator, type of the structuring element and its characteristics. It determinates more precise processing and enhancement of the different medical modalities images.

The processed image can be saved on the disk and so can be used to another processing or its visualization.

2. THE GUI FOR MORPHOLOGICAL PROCESSING OF MEDICAL IMAGES

The Fig.1 shows the GUI for morphological filtering of medical images. It is divided in several areas, where the user applies different settings, concerning morphological operators and their characteristics.

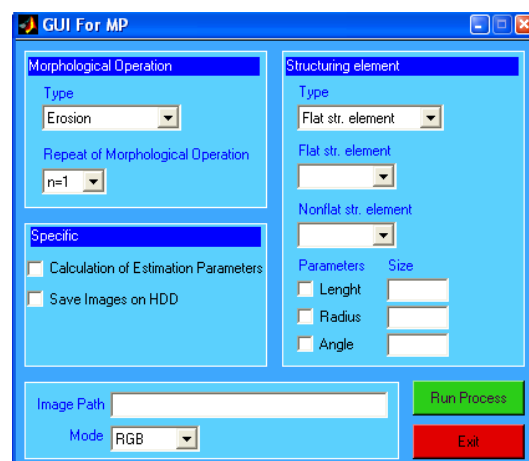


Fig. 1. GUI for morphological processing of medical images

The area "Image Path" is for entering an image file name, but without an image file extension. For example, if the file name is "pic1.jpg", the user should write "pic1". The image file for morphological processing must be in the same directory (folder), where the main program and the rest modules are. The image processing is made in two modes – RGB and YUV, chosen through the pop-up menu, default value is RGB.

The morphological operator's settings are selected in area "Morphological operation", shown in Fig. 2.



Fig. 2. Area "Morphological Operation"

Two parameters can be selected: Type of operation and the repeat of morphological operation. The repeat of morphological operation must be positive integer. Recommended values for "Repeat" from 1 to 10, because bigger values cause more noise components removal, but losing more useful parts of the image. The type of operation can be selected such as: erosion, dilatation, opening, closing, motion blur filtration and top & bottom hat filtration and is shown on Fig. 3.

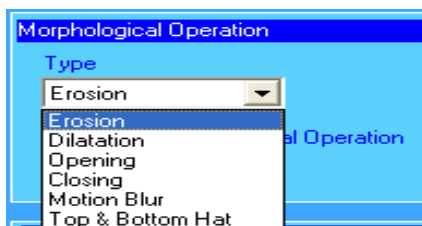


Fig. 3. Type of Morphological Operation

Selecting appropriate structuring element is an important part in morphological processing of medical images. It can be selected in area "Structuring element", shown in Fig. 4.

There are two types of structuring elements: flat or nonflat [4]. By creating of flat structuring element for morphological filtering can be used many common shapes, such as line, diamond, octagon, pair, rectangle, square and disk, shown in Fig.5. The goal is to choose the suitable form of structuring element, according to modality of medical diagnostic image. The most used elements for medical applications are: diamond, line and disk [5].

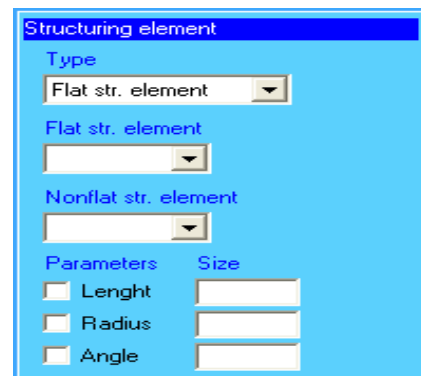


Fig. 4. Area "Structuring element"

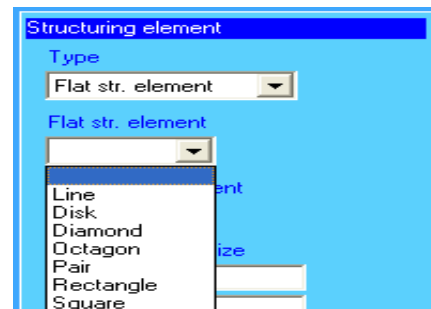


Fig. 5. Type of flat structuring element

If the structuring element is nonflat, the user can select one from two types: arbitrary or ball. In addition the size of the structuring element can be also selected: length, angle and radius. The length of the line is approximately the distance between the centers of the structuring element members at opposite ends of the line, for example LENGHT=5. The angle (in degrees) of the line is measured in a counterclockwise direction from the horizontal axis, for example DEG=0 (DEG=45) [4]. By selecting of disk or diamond-shaped structuring element, the user must determinate its radius R, where R specifies the distance from the structuring element origin to the points of the disk or the diamond.

The area "Specific" gives an opportunity to save results in image files in 'jpg' format if 'Save Images' is checked and estimate morphological processing if "Calculate of estimation parameters" is checked, as shown in Fig. 6. On the base of analysis of some objective quantitative estimation parameters can be selected the form and size of the structuring element. The condition is: minimum value for CNR and maximum values for PSNR and E_{FF} .

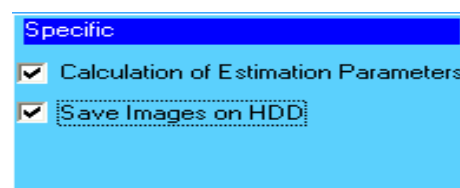


Fig. 6. Area "Specific"

After choosing all input information the procedure of morphological processing begins, when the user clicks on button 'Run'. Then the final result is shown – original image, and processed image. When button "Exit" is pressed the user is asked whether he wants to quit the program. If he chooses 'Yes', the program can be closed, if he chooses 'No', he continues working with the program.

3. TASKS CARRIED OUT FROM THE MAIN PROGRAM

The basic algorithm that works behind is shown in Fig. 7.

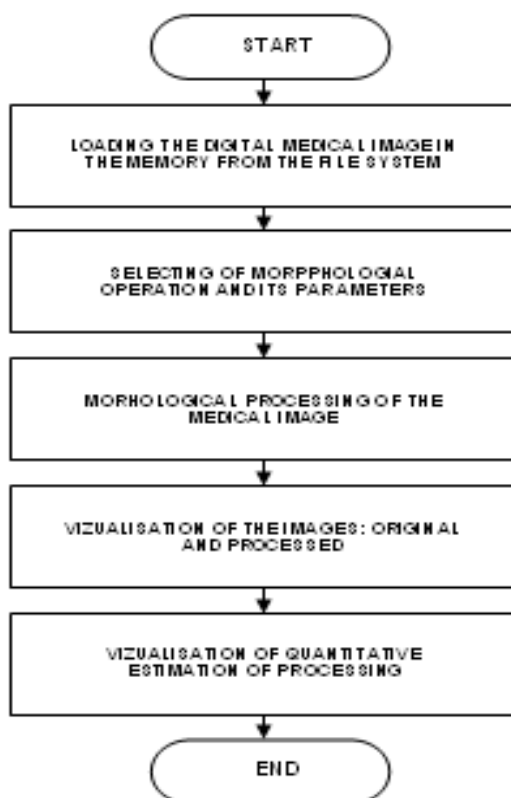


Fig. 7. Block diagram of the algorithm

By acting of component from GUI can be implemented a callback-function from the main program [6]. Every graphic component can be treated to object. Every object can be referred to handle. The objects referred a complex of attributes, which can be manipulated from the software. The multifarious attributes can be leaved for using in MATLAB environment, such as "Enabled", "Value", "Visible", "On", "Off" etc.. Every attribute can be enable in the presence of corresponding handle or reference to the object. Every graphic component can be reiterated to a cycle of events for the MATLAB environment by initialization of the graphic application. It

submits addresses of the callback –functions, associated to a given event, which are important. By its identification can be called out a corresponding callback-function.

One of the important tasks that the main program has is input data validation. The execution is canceled if an error concerned with wrong information occurs. Another essential purpose of the main program is presenting the input information in appropriate data structures [6]. It is necessary for the next steps in the processing strategy, In this step the processing is made with appropriate input data. Wrong information prevents morphological processing from carrying out or may lead to wrong output.

The applied algorithm calculates also some objective quantitative estimation parameters as: Coefficient of noise reduction (CNR), Signal to noise ratio in the noised image (SNR_Y), Signal to noise ratio in the filtered image (SNR_F), Effectiveness of filtration (E_{FF}), Peak signal to noise ratio (PSNR) [3]. On the base of their analysis can be selected the most suitable morphological operator, type of the structuring element and its characteristics. It determinates more precise processing and enhancement of the different medical modalities images.

In Fig. 8 are shown respectively the visualizations of original CT images of size 256x256 pixels from the brain and it's modifications by processing of erosion, opening and $n=8$ times closing with disk structuring element by $R=3$.

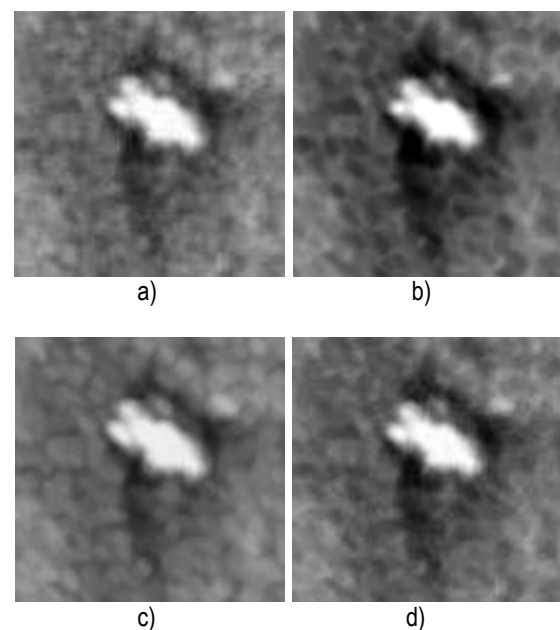


Fig. 8. CT images: a) original; b) after erosion; c) after opening; d) after closing $n=8$

4. CONCLUSION

In the paper is presented a GUI for morphological processing of medical images. It uses MATLAB defined function and works in MATLAB 6.5 environment. The pre-processing can realize a nonlinear filtration by using of different type of operators and its parameters. The GUI can be used in engineering education for studying this pre-processing. It can be used also in real time to provide important anatomical information to physicians and specialist upon which can be made diagnoses of different diseases.

References

- [1] M. Smith, A. Docef, "Transforms in telemedicine applications", Kluwer Academic Publishers, 1999.
- [2] T. Athhanasiadis, M. Wallace, K. Kapouzis, S.Kollias," Utilization of evidence theory in the detection of salient regions in successive CT images", Oncology reports, Vol.15, 2006, pp.1071-1076
- [3] R.Gonzalez, R. Woods, Digital Image Processing, Addison Wesley Publishing, 1992.
- [4] MATLAB, User's Guide, www.mathwork.com
- [5] M. Schulze, "Biomedical Image Processing with Morphology-based nonlinear Filter, Ph.D. Dissertation, University of Texas, USA,1994.
- [6] V. Georgieva, "An Influence of the Structuring Element on Morphological Filtering for Medical Image Enhancement", Proceedings ICEST'2009, Vol.2, pp. 435-438, V. Tarnovo, Bulgaria, 2009.

DESIGN OF SYSTEM FOR THERAPY WITH RUNNING LOW FREQUENCY MAGNETIC FIELD

Sasho Guergov*, Dimiter Dimitrov*, Atanas Dimitrov*, Miglena Dontschewa**

*Technical University of Sofia, Bulgaria
1000 Sofia, "Kl. Ohridsky" str.8

Tel. (+359 2) 965-3246; e-mail: sguergov@tu-sofia.bg

Tel. (+359 2) 965-2278; e-mail: dcd@tu-sofia.bg

**FH Vorarlberg University of Applied Sciences – Dornbirn, Austria
Hochschulstrasse 1, 6850 Dornbirn

Tel(+43) 557220336730, e-mail: miglena.dontschewa@fhv.at

Abstract

A visualisation of space configuration of low frequency static and running magnetic field is done in the paper. The requirements for design of system for running magnetic field in magneto-therapy is presented. Some mechanical solutions for system for running magnetic field are described In the paper, also.

1. INTRODUCTION

The space configuration of low frequency magnetic field, created by two coils can be obtained using computer simulation. This simulation is on the base of appropriate algorithms [1,2]. A space configuration of a pair coils can be seen on fig.1. Different colors are used for different values of magnetic induction's module. The visualizations has been done for the values of magnetic induction's module from $1,07\mu T$ to $30,89 mT$. The lines of magnetic induction in different points in the plane of axis Z are done by segments. The changes of the value and lines of magnetic induction between the two coils are too small. Therefore the magnetic field between two coils can be described as homogeny. The value of the coil in two inductors is $2 A$.

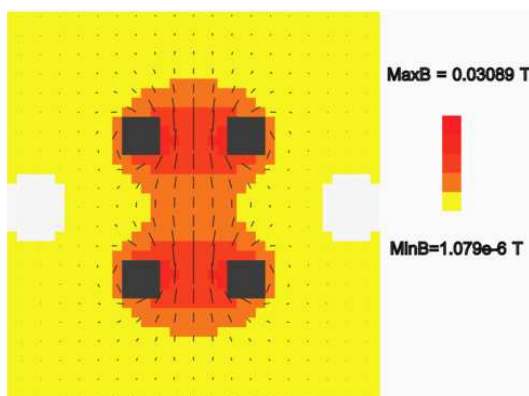


Fig. 1. Space configuration of low frequency magnetic field created by two coils

2. DESIGN OF THE BED FOR THERAPY BY RUNNING MAGNETIC FIELD

The method for computer simulation of space configuration of low frequency magnetic field of pair coils can be used for computer simulation of space configuration of magnetic field in the case of running magnetic field, also. In this case the coils can be as one or two sequences on the bed Fig. 2.

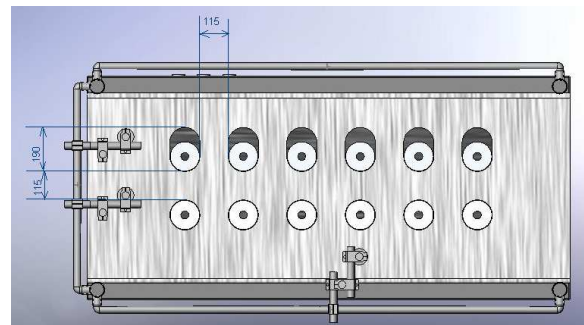


Fig. 2. The disposition of coils on the bed in the case of running magnetic field

The materials of the bed should be non magnetic. An appropriate plastic can be used. This plastic should has enough mechanical strong. For instance can be used material Polipa PA6. This materials has high mechanical hardness, high chemical steady, high steady for wear out, good skid, high electrical steady, good absorption of hits.

The patients should be recumbent on the coil's sequence on the bed. The mutual disposition of two sequence coils and patient's body can be seen on fig. 3.

On the patient's body should be one or two mobile coils depend of the number of coil's sequences. The coils on the bed should be on when they are under mobile coils.

The mechanical construction of system for running magnetic field can be seen on Fig. 4.

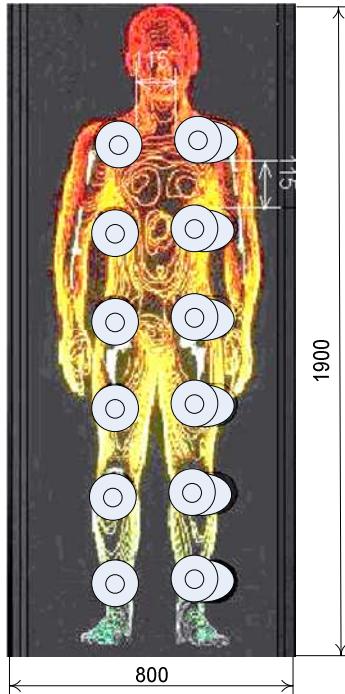


Fig. 3. Mutual disposition of two sequence coils and patient's body

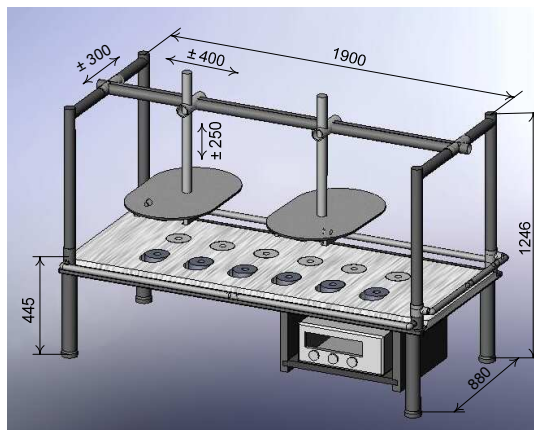


Fig. 4 Mechanical construction of system for running magnetic field

The "movement" of low frequency magnetic field can be obtained by mechanical running of two mobile coils. The space distribution of the magnetic induction's module can be seen on fig. 5. If every pair of coils on the bed are on when they are under the mobile pair coils. The space distribution of magnetic induction's value of running magnetic field (fig. 5) has been done for different position of mobile coils.

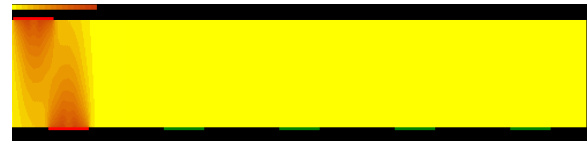


Fig. 5a



Fig. 5b



Fig. 5c



Fig. 5d

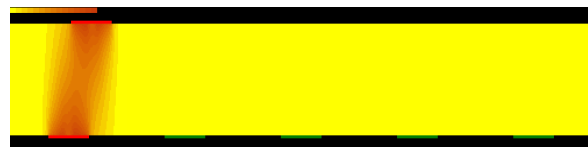


Fig. 5e

Fig. 5. Space distribution of magnetic induction's value of running magnetic field

It's clear that the running magnetic field can be obtained not only by mechanical movement of two coils. It can be provided by electronic switching, also. In this case on the place of mobile coils should be situated the same two sequences of coils as these on the patient's bed. The all coils should be connected to the outputs of apparatus for magneto-therapy. In every moment only two pairs of coils should be on, one pair on the bed and one pair of "mobile" coils. The advantages of electronic switching of coils are clear. There are some disadvantages, also – the price of the system for running magnetic field will be increased because of increasing of number of coils, because of more complicated apparatus for magneto-therapy and because of more complicated mechanical construction.

The signals for the coils of running magnetic field can be created by apparatus for magnetotherapy (Fig. 6) All coils can be connected to the outputs of this apparatus.



Fig. 6. Apparatus for magneto-therapy

4. CONCLUSION

1. A computer simulation of space distribution of magnetic induction' values of pair coils depending of the value of electrical current have been donning in the paper.

2. A computer simulation of space distribution of magnetic induction' values in the case of running magnetic field are presented in the paper.

3. One mechanical construction of system for magneto-therapy with running magnetic field has been done.

References

- [1] D.Tz. Dimitrov, Computer Simulation of Space Configuration of Low Frequency Magnetic Field in Magnetotherapy, p.28-32, Electronics and Electrical Engineering, ISSN 1392-9631, 2005, -No.3(59),
- [2] Д.Ц.Димитров, Изследване на пространствената конфигурация на нискочестотно магнитно поле в магнитотерапията. стр.38-43. "Електроника и Електротехника", No.9-10, 2005
- [3] Bekiarski Al., Sn. Pleshkova – Bekiarska. Simulation of Audio Visual Robot Perception of Speech Signals and Visual Information. Proceedings of International Conference on Communications, Electromagnetic and Medical Applications (CEMA'08), Athens, Greece, 6th-8th November, 2008, pp. 19 – 24.
- [4] Bekiarski Al., Sn. Pleshkova – Bekiarska. Visual Design of Mobile Robot Audio and Video System in 2D Space of Observation. Proceedings of International Conference on Communications, Electromagnetic and Medical Applications (CEMA'08), Athens, Greece, 6th-8th November, 2008, pp. 14 – 18.
- [5] Pleshkova-Bekiarska Sn., Al. Bekiarski, Speech Localization and Video Control for Audio and Visual Robot Systems. International Conference Computer Science'2008, 17 - 19 September pp.26-30, 2008, Kavala, Greece,
- [6] Docheva L., Al. Bekiarski. Analogue neural network comparative simulation by means of MATLAB and PSPICE software products. XXXVIII International Scientific Conference Information Communication and Energy Systems and Technologies, vol.№1, pp. 270-272, 2003.
- [7] Ахмед Алхадж Али, А. Б. Бекярски. Филтър за отделяне на движещи се обекти с използване на дискретно преобразуване на Фурие. Електротехника и Електроника, бр. 9-10, София, 1994 г., стр. 21-24.
- [8] The paper is published with the financial support of the National Science Fund, Contr. № ДО 02-211/08.

DESIGN OF GIRDLE COIL FLEXIBLE SYSTEM FOR MAGNETOTHERAPY

Sasho Guergov,* Dimiter Dimitrov*, Miglena Dontschewa**

*Technical University of Sofia, Bulgaria
1000 Sofia, "Kl. Ohridsky" str.8

Tel. (+359 2) 965-3246; e-mail: sguergov@tu-sofia.bg

Tel. (+359 2) 965-2278; e-mail: dcd@tu-sofia.bg

**FH Vorarlberg University of Applied Sciences – Dornbirn, Austria

Hochschulstrasse 1, 6850 Dornbirn

Tel(+43) 557220336730, e-mail: miglena.dontschewa@fhv.at

Abstract

An investigation of space configuration of low frequency magnetic field generated by girdle coil is described in the paper. The results of preliminary mathematical calculation and computer simulation of low frequency magnetic field of girdle coil has been done together with histograms of space distribution of module of magnetic induction in the girdle coil in the case of static activation. Some mechanical solutions for Girdle Coil Flexible System for Magnetotherapy are described in the paper, also.

1. INTRODUCTION

A girdle coil system, which is used in magnetotherapy now can be seen on Fig. 1.



Fig. 1. An ordinary girdle coil system

It's well known that the space configuration of low frequency magnetic field in the patient's area is very important in the process of magnetotherapy [1,2]. Therefore the precise calculations of low frequency magnetic field as well as an easy-to-understand visualization of field distribution over the patient's area are of great importance for the reliability and predictability in the process of experimental measurement of magnetic induction of the constructed electromagnetic device. A magnetic device (girdle coil) has been constructed for use as a therapeutic tool in magnetotherapy (Fig. 2).

The calculation exposes a low frequency magnetic field solver that allows evaluating the field strength throughout the volume influenced by the coil.

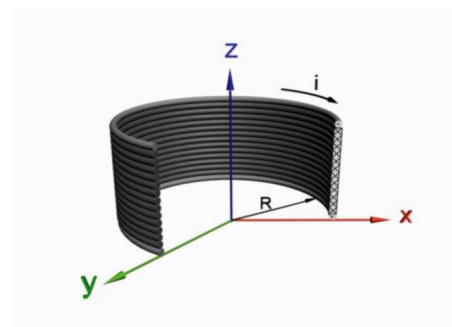


Fig. 2. Girdle coil

2. DESIGN STAGE

The evaluation of the low frequency magnetic field distribution and its visualization is a difficult task and usually requires a lot of time depend on the environment geometry and applied visualization techniques [1,2]. Additionally fields are often represented as large sums of field contributions of individual current turns.

The calculation of field in space (off-axis form) requires field formulas that involve elliptic integrals or other complicated expressions that have to be approximated some how.[3,4]. In the particular case the task is to evaluate the values of magnetic field induction at each point of the area of space enclosed into the coil with sizes according to the above Fig.3. For the axial symmetry of the generated low frequency magnetic field the calculations can be performed only for the section perpendicular

to the coil plain and going through the centre of the coil.

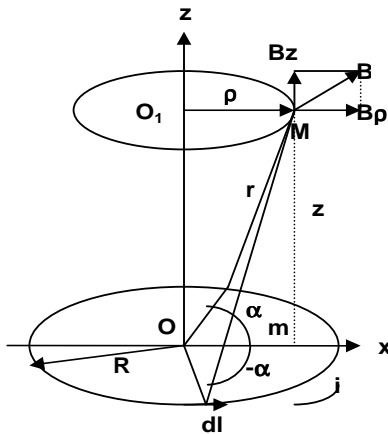


Fig. 3. Calculation of magnetic induction in the case of low frequency magnetic field created by girdle coil

To achieve better effectiveness of the calculations as well as to decrease the memory necessary to store the results, the values of magnetic induction are evaluated only for one half of this section (right half). Magnetic induction \mathbf{B} is stored together with its two ingredients – radial component \mathbf{B}_ρ and axial component \mathbf{B}_z for a future use to obtain vector form of accumulated field data. The magnetic induction \mathbf{B} generated by a separate turn with radius R at an arbitrary point M in the girdle coil (Fig.2) is calculated using a method based on magnetic vector-potential .

The key equations used to calculate the two components \mathbf{B}_ρ and \mathbf{B}_z of magnetic induction \mathbf{B} in a arbitrary point in the girdle coil:

$$B_\rho = \frac{\mu_0 i}{2\pi} \frac{z}{\rho \sqrt{(R+\rho)^2 + z^2}} \left[\frac{R^2 + \rho^2 + z^2}{(R-\rho)^2 + z^2} L - K \right] \quad (1)$$

$$B_z = \frac{\mu_0 i}{2\pi} \frac{1}{\sqrt{(R+\rho)^2 + z^2}} \left[\frac{R^2 - \rho^2 - z^2}{(R-\rho)^2 + z^2} L + K \right] \quad (2)$$

$$B = \sqrt{B_\rho^2 + B_z^2} \quad (3)$$

where:

- K and L are full elliptical integrals;
- R is the radius of the girdle coil (Fig. 2);
- ρ is the radius of an imaginary turn of the arbitrary point M (Fig. 2)
- z is the vertical axis (Fig. 2)
- i is the value of current in the girdle coil;
- μ_0 is the absolutely magnetic permeability;

3. EXPERIMENTAL RESULTS

The presented article illustrates one approach to calculate and visualize a low frequency magnetic field distribution in 2D. The field is used for therapeutic purposes in magnetotherapy and is generated by girdle coil. The coil consists of a number of current turns with the radius 1 mm. The histogram of experimental measurements of module of magnetic induction in the plane XOZ (Fig. 2) can be seen on Fig. 4.

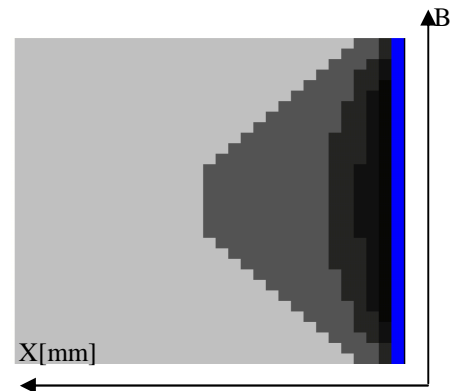


Fig. 4. Experimental histogram of the module of magnetic induction in the case of static activation of the girdle coil

4. DESIGN OF THE BED FOR GIRDLE COIL FLEXIBLE SYSTEM

The materials of the bed (Fig.5) should be non magnetic. An appropriate plastic can be used. This plastic should has enough mechanical strong. For instance can be used material Polipa PA6. This materials has high mechanical hardness, high chemical steady, high steady for wear out, good skid, high electrical steady, good absorption of hits.

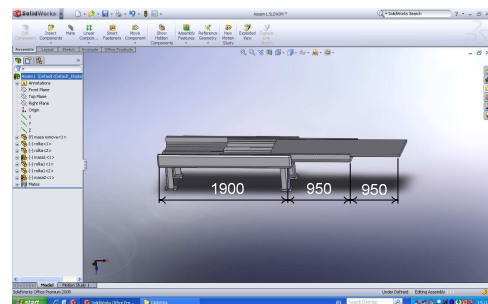


Fig. 5. Design of the bed for flexible girdle system

The bed should be adaptive according to the patient's body .Therefore the bed should be flexible.

The mechanical construction of girdle coil can be seen on fig. 6.

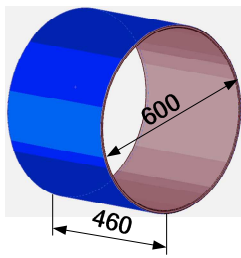


Fig. 6. Mechanical construction of girdle coil

The girdle coil should be flexible also. The idea for flexibility of girdle coil is illustrated on fig. 7.

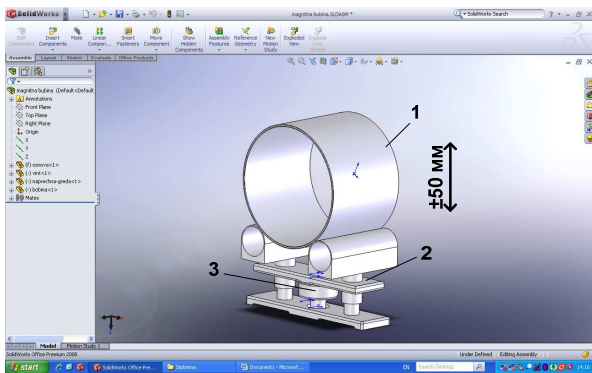


Fig. 7. A flexible girdle coil

It's clear (according to the fig. 5 and the fig. 7) that the described girdle coil system for magnetotherapy has independent flexibility in two orthogonal planes. The mechanical construction of this system can be seen on fig. 8.

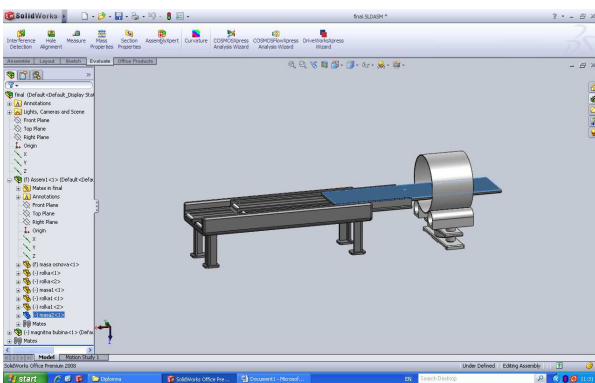


Fig. 8. A girdle coil flexible system

5. EXPERIMENTAL SETUP

A small coil (diameter $d = 8mm$, height $h = 10mm$ and current turns $w = 2 \times 300$) has been used as sensor for measurement of the value of magnetic induction. This coil has been connected with the inputs of differential amplifier in the input of appa-

ratus for measurement of magnetic induction of low frequency magnetic field. The measurement has been done for the sinusoidal current in the girdle coil with frequency $f = 50Hz$. It's well known that the frequency band $f = 10Hz - 100Hz$ is used in the process of magnetotherapy. The sensor has been putted in different points around the girdle coil. The measurement of the girdle coil's current has been done by ordinary ampermeter. The measurement of module of magnetic induction on the axes X and Z (Fig, 2) has been done. The results of experimental measurements together with the results of calculation of the module of magnetic induction on axis X can be seen on Fig. 9.

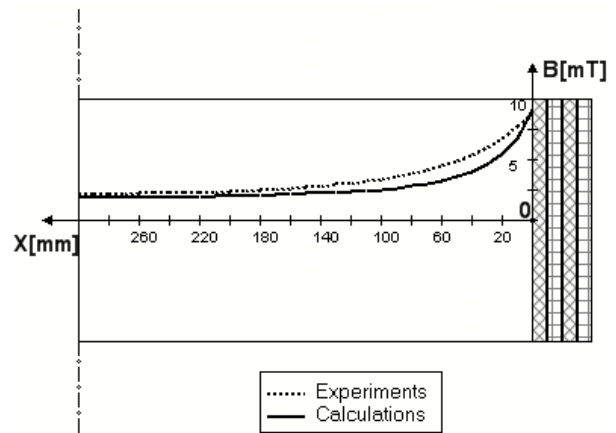


Fig. 9. Module of magnetic induction on the axis X

The results of experimental measurements together with the results of calculation of the module of magnetic induction on axis Z can be seen on Fig.10.

6. LEVEL OF ERRORS IN EXPERIMENTAL SETUP

The main causes for errors between calculated and measurement results are: the finite sizes of the sensor, the permanent error of the place of sensors in it's putting in different points and orientation of it's axis (the angle between the vector of magnetic induction and the axis of sensor), the error of the measurement of current in the girdle coil, the influence of other magnetic fields with the same frequency $f = 50Hz$. Some of these errors have been reduced using differential coil as sensors. The results of calculation and results of experimental measurements are similar. It was the main goal of investigation. Of course it's possible to obtain more precise methods and measurement devices, but it's not necessary in the case of magnetotherapy,

where usually the values of magnetic induction are 10-30mT and 10% error is acceptable. It's clear that only one small translation of the human body in the girdle coil would be enough for an error of the value of module of magnetic induction in an arbitrary point of the human body, more than 10%. The value of relative magnetic permeability of live tissue $\mu_r \approx 1$ as in the air.

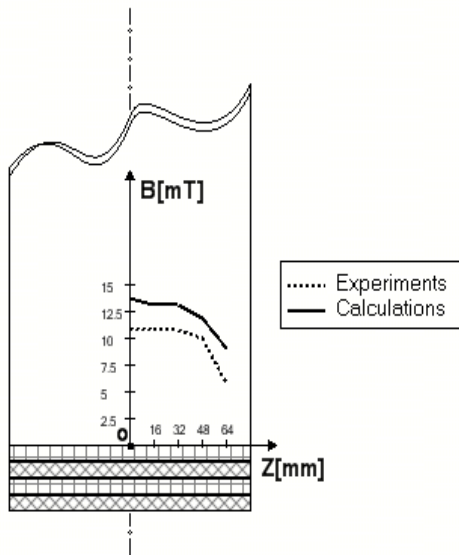


Fig. 10. Module of magnetic induction on the axis Z

Therefore computer simulation can be used successfully for future investigation of space configuration of low-frequency magnetic field in the human body, also. This is the main conclusion of the above investigations.

7. CONCLUSION

1. Visualization, calculation and experimental investigation of the space configuration of low frequency magnetic field in the patient's area is of great importance as preliminary result not only for the process of experimental measurement of the value of magnetic induction in magnetotherapy, but for evaluation of the effectiveness of developed electromagnetic devices, also. Additionally these two processes can be used to assist the design of such devices. Into the particular case of therapeutic magnetic field the calculation and visualization are intended to allow the user visually evaluate the strength of the field into the influenced area of space.

The data structures developed for geometric and calculated data representation are designed to store both radial B_p and axial B_z components of magnetic induction for future visualization of a vec-

tor field in 2D and 3D. At the implementation stage the data structures are chosen in such a way to allow data to be shared between different applications.

The experimental measurements of the module of magnetic induction in girdle coil confirm results, obtained by computer calculation.

2. One mechanical construction of system for magneto-therapy with running magnetic field has been done.

3. It's possible to provide easy influence of magnetic field on different parts of the human body because of bed's flexibility without movement of the patient.

4. It's possible to change easy the value of magnetic induction in the human body on the base of flexibility of the girdle coil.

References

- [1] D.Tz. Dimitrov, Computer Simulation of Space Configuration of Low Frequency Magnetic Field in Magnetotherapy, p.28-32, Electronics and Electrical Engineering, ISSN 1392-9631, 2005, -No.3(59),
- [2] Д. Ц. Димитров, Изследване на пространствената конфигурация на нискочестотно магнитно поле в магнитотерапията. стр.38-43. "Електроника и Електротехника", No.9-10, 2005
- [3] D. Dimitrov, A. Dimitrov, Computer Simulation of Low Frequency Magnetic Field, p.171-175, Proceedings of 17th EAEEIE Annual Conference on Innovation in Education for Electrical and Information Engineering, June, 1-3, 2006, University of Craiova, Romania.
- [4] Dimitrov, D.Tz. Visualization of a Low Frequency Magnetic Field, Generated by Girdle Coil in Magnetotherapy, Electronics and Electrical Engineering, Nr.3(59), 2005, p.28-32
- [5] Foley, J.D., A. van Dam, S. Feiner, J. Hughes, Computer Graphics: Principles and Practice, Addison-Wesley, Reading, MA, 1990
- [6] Hearn, D., M. P. Baker. Computer Graphics, Prentice-Hall, NJ, 1997

The paper is published with the financial support of the National Science Fund, Contr. № ДО 02-211/08.

SYSTEM FOR THERAPY WITH ACUPRESSURE AND LOW FREQUENCY MAGNETIC FIELD

Sasho Guergov*, Dimiter Dimitrov**, P. Petrov***

Technical University of Sofia, Bulgaria
1000 Sofia, "Kl. Ohridsky" str.8

*Tel.(+359) 2 965-3246;e-mail:sguergov@tu-sofia.bg

Tel. (+359 2) 965-2278;e-mail:dcd@tu-sofia.bg; *Medical centre, Ivanjane

Abstract

An simultaneously application of low frequency magnetic field and acupressure is described in the paper. A visualisation of space configuration of low frequency static magnetic field is done in the paper, also. A design of system for acupressure is done together with mathematical description of action of mechanical device for acupressure. The requirements for design of system for therapy with low frequency magnetic field and acupressure are presented. Some mechanical solutions for system for acupressure are described In the paper, also.

1. INTRODUCTION

The application of China's method for acupressure is very actual in medical therapy, now. Usually physicians provide application of acupressure by his hands. It's inconvenient first of all for physician. He's able to work for short time. Then he can continue after relax, but the number of these procedures per day are limited. In other side it would be better to provide acupressure simultaneously on more points on the human body. It's impossible because physician has only two hands.

The results of therapy by acupressure would be more good if there would be provided more intensive movement of the blud in around the points of acupressure. This activation of blud's movement can be provided by application of low frequency magnetic field together with acupressure.

It's clear that it' s necessary to provide special device for acupressure, which can be used together with special device for creating of low frequency magnetic filed around the points for acupressure. Therefore the application of system for simultaneously application of acupressure and low frequency magnetic field is very actual, now.

2. DESIGN OF DEVICES FOR CREATING OF LOW FREQUENCY MAGNETIC FIELD AROUND THE POINTS FOR ACUPRESSURE.

Usually the low frequency magnetic field can be created using two coils, connected to the output of apparatus for magneto-therapy. This apparatus is a source of special electrical signals for the coils.

Often the application of above described method for therapy is on the hand because there are situated many points of acupunctures.

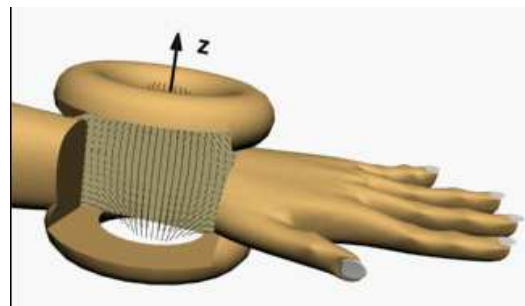


Fig. 1. A possibility for disposition of two coils on the hand

The space distribution of the values of magnetic induction can be seen on fig. 2.

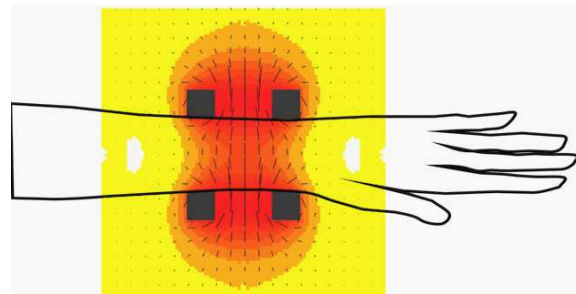


Fig. 2. The space distribution of the values of magnetic induction

In this case one possibility for disposition of two coils together with

The space configuration of the lines of vector of magnetic induction can be seen on fig. 1.

It's well known that on the spine there are many points of acupuncture, also. Some examples for disposition of coils on the spine can be seen on fig.3.

The axis of space components of magnetic induction of magnetic field, created by different coils can be seen on fig. 3, also.

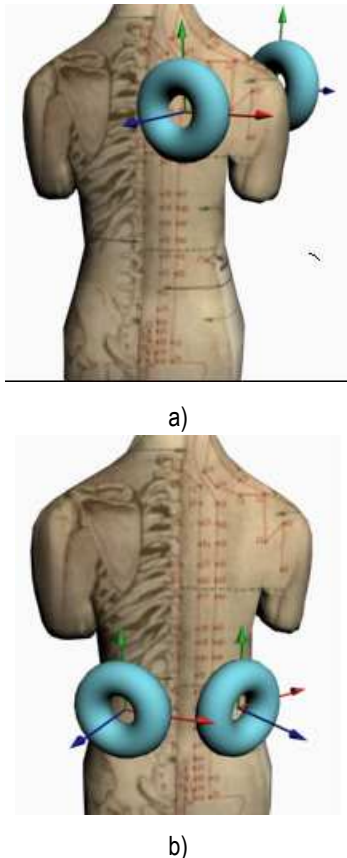


Fig. 3. Some examples for disposition of coils on the spine

A space disposition of two coils in the case of an other application of above mentioned method of acupuncture together with low frequency magnetic field can be seen on fig.4.



Fig. 4a. A space disposition of two coils on X-ray image

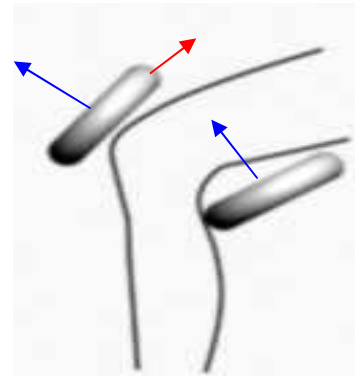


Fig. 4b. The axis of space components of magnetic induction of magnetic field, created by two coils

3. DESIGN OF MECHANICAL DEVICE FOR ACUPRESSURE

Usually the line of mechanical pressure is the axis of coils.

The sizes of coils can be different according to the sizes of "active" area around of the acupuncture points.

On fig. 5 can be seen a mechanical device for acupuncture, when:

- 1 is motor;
- 2 is axle;
- 3 is shaft;
- 4 is a coil, which provides axial movement of the shaft;
- 5 is metal disk;
- 6 is plastics body;
- 7 is massage pimple (osezatel).

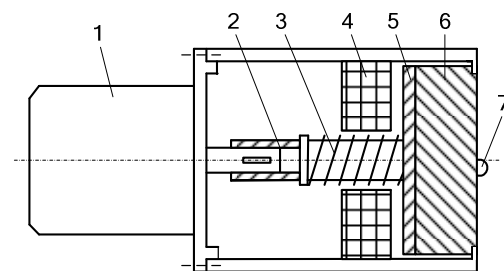


Fig. 5. Mechanical device for acupuncture

The equation of movement of the plastics body 6 is:

$$m\ddot{x} + bx = cx = H \sin(pt) \quad (1)$$

or

$$x + k^2 x = h \sin(pt) \quad (2)$$

When:

$$k = \sqrt{\frac{c}{m}} \text{ is the frequency of own oscillations.}$$

$$h = \frac{H}{m}$$

m [kg] is the masse of movement part;

c [$\frac{N}{m}$] is elastic constant of the spring;

H is the amplitude;

p is the frequency.

The period of oscillation can be determined using the equation (3).

$$T = \frac{2\pi}{k} = 2\pi\sqrt{\frac{m}{c}} \text{ [s]} \quad (3)$$

The integral of equation (2) is the sum of the integral of free oscillations and private solution of equation (2):

$$x = x_1 + x_2$$

When:

$$x_1 C_1 \cos(kt) \quad (4)$$

and

$$x_2 = A \sin(pt) \quad (5)$$

The equation (5) can be put in equation (2):

$$A(k^2 - p^2) = h \quad (6)$$

If $k \neq p$:

$$A = \frac{h}{k^2 - p^2} \quad (7)$$

The integral of equation (2) is:

$$x = C_1 \cos(kt_1) + C_2 \sin(kt) + \frac{h}{k^2 - p^2} \sin(pt) \quad (8)$$

If the frequency of own oscillation is small than intimidating force ($k \ll p$), $A \ll 0$, and taking in account the equation (5):

$$x_2 = -\frac{h}{p^2 - k^2} \sin(pt) = \frac{h}{p^2 - k^2} \sin(pt + \pi) \quad (9)$$

The basic output parameters of the described device for acupressure can be obtained using equations (10), (11) and (12):

$$x = \frac{h}{k^2 - p^2} \sin(pt) \quad (10)$$

$$x = \frac{ph}{k^2 - p^2} \cos(pt) \quad (11)$$

$$x = -\frac{p^2 h}{k^2 - p^2} \sin(pt) \quad (12)$$

For instance, if the movement of device for acupressure is by electrical engine for direct current (6V) with input power $P_1 = 15W$ and current $I_a = 2,5A$, the output torque is:

$$M_{out} = \frac{60P}{n2\pi2_{tr} \eta_{el.eng.}} = \frac{60.15}{50.2.\pi.0,2.5.0,75} = 5,09Nm$$

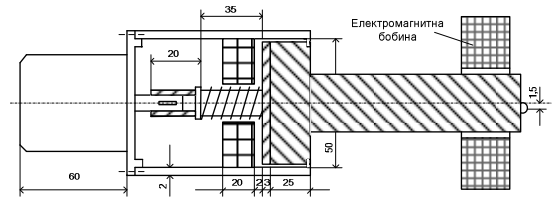


Fig. 6. The modified device for acupressure simultaneously with low frequency magnetic field.

For simultaneously application of low frequency magnetic field and mechanical acupressure, the line of mechanical pressure should be the same as the line of coil. Therefore the devices on fig. 5 should be modified according to the fig. 6.

4. CONCLUSION

1. A computer simulation of space distribution of magnetic induction' values of pair coils depending of the value of electrical current around the points of acupuncture in different cases of disposition of coils on the human body has been don in the paper .

2. A mathematical description of mechanical device for acupressure has been done.

3. Some mechanical constructions of devices for separate acupressure (Fig. 5) and for simultaneously acupressure with low frequency magnetic field (Fig. 6) have been done, also.

References

- [1] D.Tz. Dimitrov, Computer Simulation of Space Configuration of Low Frequency Magnetic Field in Magnetotherapy, p.28-32, Electronics and Electrical Engineering, ISSN 1392-9631, 2005, -No.3(59),
- [2] Д. Ц. Димитров, Изследване на пространствената конфигурация на нискочестотно магнитно поле в магнито-терапията. стр.38-43. "Електроника и Електротехника", No.9-10, 2005
- [3] D.Dimitrov, A.Dimitrov, Computer Simulation of Low Frequency Magnetic Field, p.171-175, Proceedings of 17th EAEEIE Annual Conference on Innovation in Education for Electrical and Information Engineering, June, 1-3, 2006, University of Craiova, Romania.
- [4] Хилебрехт, М. Акупресура, ISBN9548793253
- [5] Емас, 1998, с.240
- [6] Хилебрехт, М. Акупресура – път към добро здраве, Емас, 2000, с. 240

The paper is published with the financial support of the National Science Fund, Contr. № ДО 02-211/08

SIMULTANEOUSLY INFLUENCE OF PERMANENT ELECTRICAL FIELD AND LOW FREQUENCY MAGNETIC FIELD ON THE HUMAN BODY

Dimiter Tz. Dimitrov*, Nikola D. Ralev*, Lukosevicius Arunas**

*Faculty of Telecommunication, Technical University of Sofia,
"Kl.Ohridsky" str.8, 1000 Sofia, Bulgaria
Tel./Fax:+359 2 965 2278, E-mail:dcd@tu-sofia.bg

**Kaunas University of Technology, Faculty of Radioelectronics
Guobu str. 67, Kaunas, LT-52316, Lithuania
Ten. +370 37 769191, arunas.lukosevicius@ktu.lt

Abstract

The separate influence on the human body of permanent electrical field and separate influence of low frequency magnetic field is well known in medicine and especially in physiotherapy. An investigation of simultaneously influence of permanent electrical field and low frequency magnetic field on the human body is described in the paper.

1. INTRODUCTION

The diffusion of ions of different medicaments through the skin (ionophoresis) can be provided by permanent electrical field. The effect of this therapy can be more significant if the movement of medicament's ions can be not only on the lines of vector of intensity of electrical field, but on 3D curves. This movement of ions can be provided in the case of simultaneously influence of permanent electrical field and low frequency magnetic field.

2. MATHEMATICAL ANALYSIS

The simultaneously influence of electrical and magnetic fields on ion (ion of tissues or medicament's ion) can be seen on fig.1 According to the fig.1, the movements of ion on axis X,Y and Z can be described by the equation (1):

$$m \frac{d^2 \vec{r}(t)}{dt^2} = q \vec{E}(x, y, z, t) + q \left[\frac{d\vec{r}(t)}{dt} \times \vec{B}(x, y, z, t) \right] \quad (1)$$

Where:

$\vec{E}(x, y, z, t)$ is the intensity of electrical field;

$\vec{B}(x, y, z, t)$ is the magnetic induction.

m is the mass of ion;

q is the electrical charge of ion.

\vec{r} is the tangential vector of trajectory of movement of ion.

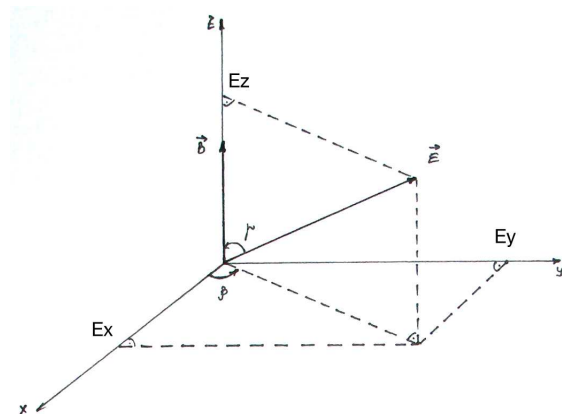


Fig. 1 Simultaneously influence of electrical and magnetic fields on ion

On the base of equation (1) can be obtained the system of equations (2) for every axis X,Y and Z.

$$m \frac{d^2 x(t)}{dt^2} = q [E(x, y, z, t) \sin \gamma \cos \beta + B(x, y, z, t) \frac{dy(t)}{dt}]$$

$$m \frac{d^2 y(t)}{dt^2} = q [E(x, y, z, t) \sin \gamma \sin \beta + B(x, y, z, t) \frac{dx(t)}{dt}]$$

$$m \frac{d^2 z(t)}{dt^2} = q E(x, y, z, t) \cos \gamma \quad (2)$$

3. COMPUTER SIMULATION OF MOVEMENT OF IONS IN LIVE TISSUES

The system of equations (2) can be solved using MATLAB. It's well known that the ions in alive tissues are first of all the ions of Na^+ and ions of Cl^- . Therefore the investigations have been done for movement of these ions.

In the case of homogeny permanent electrical field and homogeny low frequency magnetic field can be used equations (3)

$$\begin{aligned} \vec{E}(x, u, z, t) &= const \wedge \\ \wedge \vec{B}(t) &= \vec{B}_m \cos \omega_3 t \wedge \\ \wedge \vec{B}(x, y, z) &= const \wedge \\ \wedge \omega_3 &= const \wedge \beta = 45^\circ \wedge \gamma = 45^\circ \end{aligned} \quad (3)$$

Where:

B_m is the amplitude of magnetic induction in every point of the homogeny low frequency magnetic field;

ω_3 is the frequency of magnetic field;

E is the intensity of electrical field.

In this case the system of equations (2) is as (4):

$$\begin{aligned} m \frac{d^2 x(t)}{dt^2} &= q[E \sin \gamma \cos \beta + \\ &+ \frac{dy(t)}{dt} B_m \cos \omega_3 t] \\ m \frac{d^2 y(t)}{dt^2} &= q[E \sin \gamma \sin \beta + \\ &+ \frac{dx(t)}{dt} B_m \cos \omega_3 t] \end{aligned} \quad (4)$$

$$m \frac{d^2 z(t)}{dt^2} = qE \cos \gamma$$

The trajectories of movement of ions of Na^+ in alive tissues taking in account (3) and (4) when:

$$\begin{aligned} E &= 100[V/m], |\vec{B}_m| = 30[mT], \\ \omega_3 &= 2\pi 50[1/s] \end{aligned} \quad (5)$$

can be seen on fig. 2.

The system of equations (4) can be solved for different values of parameters. This is the way for investigation of influence of the values of these parameters on the trajectory of movement of ions. The trajectory of movement of ions of Na^+ for the case when:

$$\begin{aligned} E &= 200[V/m], \\ |\vec{B}_m| &= 3[mT], \\ \omega_3 &= 2\pi 50[1/s] \end{aligned} \quad (6)$$

can be seen on fig. 3.

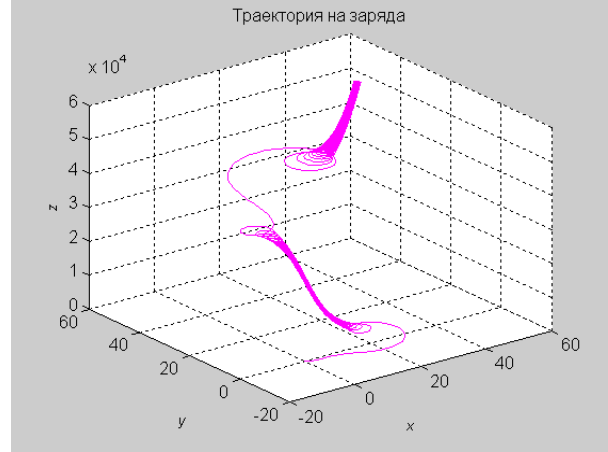


Fig. 2. Trajectory of movement of ions of Na^+ according to the equations: (3), (4) and (5)

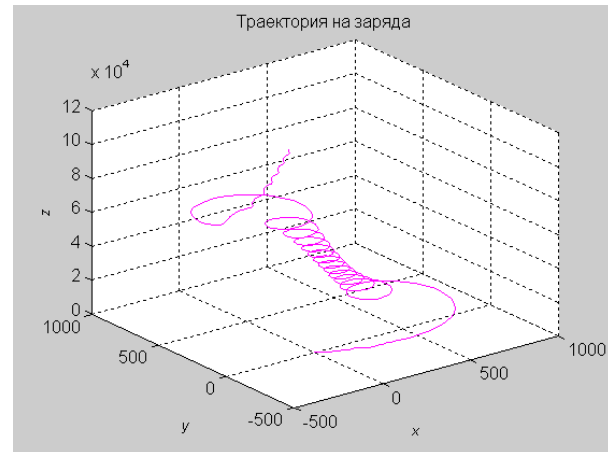


Fig. 3. Trajectory of movement of ions of Na^+ according to the equations: (3), (4) and (6)

The trajectory of movement of ions of Na^+ for the case when:

$$\begin{aligned} E &= 200[V/m], \\ |\vec{B}_m| &= 30[mT], \\ \omega_3 &= 2\pi 100[1/s] \end{aligned} \quad (7)$$

can be seen on fig. 4.

The trajectory of movement of ions of Na^+ for the case when:

$$\begin{aligned} E &= 200[V/m], \\ |\vec{B}_m| &= 30[mT], \\ \omega_3 &= 2\pi 20[1/s] \end{aligned} \quad (8)$$

can be seen on fig. 5.

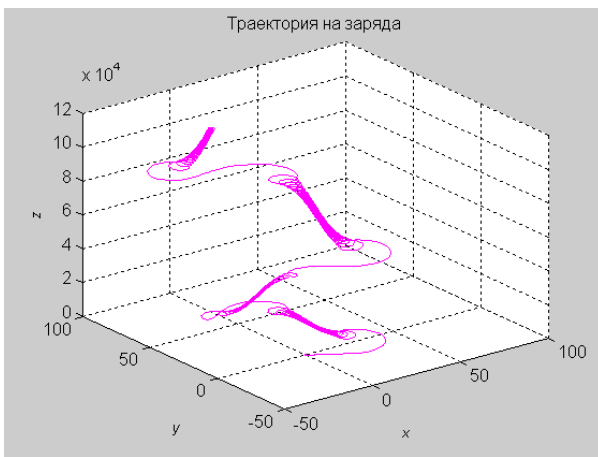


Fig. 4 Trajectory of movement of ions of Na^+ according to the equations: (3), (4) and (7)

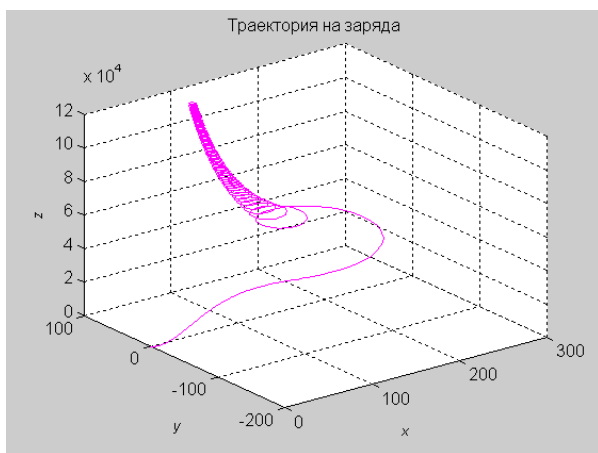


Fig. 5 Trajectory of movement of ions of Na^+ according to the equations: (3), (4) and (8)

The equations (3) are connected with application of low frequency magnetic field in the process of ionophoresis, which is often used in medicine. It's clear that 3D trajectory of movement of ions in alive tissues can be obtained as one result of additional application of low frequency magnetic field. It can be seen on Fig. 2, Fig. 3, Fig. 4 and Fig. 5 that the parameters of 3D trajectories of movement of ions can be changed not only by change of the value of intensity of permanent electrical field, but by change of parameters of low frequency magnetic field, also.

4. CONCLUSION

The 3D trajectory of movement of ions allows to obtain more good effect of therapy by ionophoresis than in the ordinary case, when only permanent electrical field is used without application of low frequency magnetic field.

A simultaneously application of permanent electrical field and low frequency magnetic field in the process of ionophoresis of foot can be seen on fig. 6.

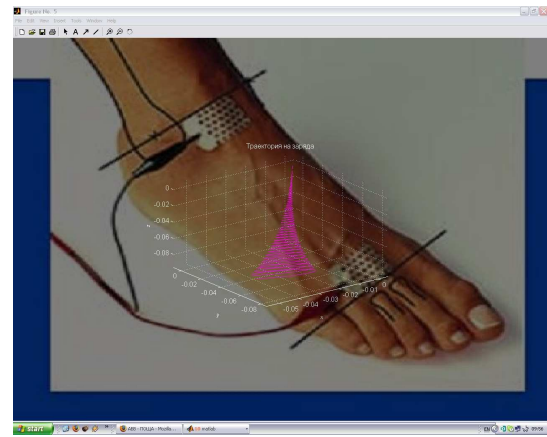


Fig. 6. A simultaneously application of permanent electrical field and low frequency magnetic field in the process of ionophoresis of foot.

References

- [1] Bekiarski Al., Sn. Pleshkova – Bekiarska. Simulation of Audio Visual Robot Perception of Speech Signals and Visual Information. Proceedings of International Conference on Communications, Electromagnetic and Medical Applications (CEMA'08), Athens, Greece, 6th-8th November, 2008, pp. 19 – 24.
- [2] Bekiarski Al., Sn. Pleshkova – Bekiarska. Visual Design of Mobile Robot Audio and Video System in 2D Space of Observation. Proceedings of International Conference on Communications, Electromagnetic and Medical Applications (CEMA'08), Athens, Greece, 6th-8th November, 2008, pp. 14 – 18.
- [3] Pleshkova-Bekiarska Sn., Al. Bekiarski, Speech Localization and Video Control for Audio and Visual Robot Systems. International Conference Computer Science'2008, 17 - 19 September pp.26-30, 2008, Kavala, Greece,
- [4] Docheva L., Al. Bekiarski. Analogue neural network comparative simulation by means of MATLAB and PSPICE software products. XXXVIII International Scientific Conference Information Communication and Energy Systems and Technologies, vol.№1, pp. 270-272, 2003.
- [5] Ахмед Алхадж Али, А. Б. Бекярски. Филтър за отделяне на движещи се обекти с използване на дискретно преобразуване на Фурие. Електротехника и Електроника, бр. 9-10, София, 1994 г., стр. 21-24.
- [6] D.Tz. Dimitrov, Computer Simulation of Space Configuration of Low Frequency Magnetic Field in Magnetotherapy, p.28-32, Journal " Electronics and Electrical Engineering", Lithuania, ISSN 1392-9631, 2005, -No.3(59),
- [7] D.Dimitrov, Visualization of a Low Frequency Magnetic Field, generated by Girdle Coil in Magnetotherapy, p.57-60, Journal "Electronics and Electrical Engineering", Lithuania, ISSN 1392-1215, 2007, -No.6(78)

The paper is published with the financial support of the National Science Fund, Contr. № ДО 02-211/08.

MODELLING OF INFLUENCE OF ELECTROMAGNETIC FIELD ON MOVEMENT OF IONS IN THE HUMAN BODY

Zoran Cvetkov*, Sasho Guergov**, Dimiter Dimitrov***, Petia Decheva****
Anton Savov*****

Technical University of Sofia, Bulgaria
1000 Sofia, "Kl. Ohridsky" str.8

*e-mail: zoran_cvetkov@yahoo.com

**Tel. (+359) 2 965-3246; e-mail: sguergov@tu-sofia.bg

***Tel. (+359 2) 965-2278; e-mail: dcd@tu-sofia.bg

*****Medical University of Sofia, Bulgaria

Abstract

In this paper we are proposing a method for computer simulation to study the behavior of charged particles in electromagnetic field. The main application of this method is the visualization of processes when of the electromagnetic field is applied to human body. Some exemplary simulations and their results are presented.

1. INTRODUCTION

Electrical and magnetic fields are often used for treating patients during recovery phase from certain illnesses. However at present time there is a lack of understanding of the exact influence of these methods on human body. Availability of such tools would visualise these processes which would greatly help the physicians to choose the proper positioning of the active devices and also their parameters in order to achieve maximum effect from this kind of treatment.

2. MODELING TARGET

Electromagnetic field has an influence on all kind of tissues. However for the current discussion we will focus our modelling attempts with the extra cellular liquid. Its properties as a medium for transportation of active chemical agents makes it perfect target for assessing effects of the influence of the electromagnetic field. Thus we limit our review only with the soft tissues and presence of the bones is ignored.

3. SIMPLIFIED MODEL OF BODY FLUIDS

As a simplified model of the body fluids we chose fluid saline. There are several types of this fluid used for transfusion [1] but in general it is sterile solution of sodium chloride (salt) in water. Up to 40g of NaCl fully dissolve in 1 L of water. For simpli-

fication we will accept that all molecules of NaCl are dissociated to Na⁺ and Cl⁻ ions.

The molecules of water are known to perform Brownian movement. It is generally random of direction and speed, and the average speed correlates to the temperature.

4. PHYSICAL MODEL

The forces generated by electromagnetic field on a charged particle is given by the Lorentz force equation [2]:

$$m\vec{a} = q[\vec{E} + (\vec{v} \times \vec{B})]$$

where:

m - is the mass of the particle,

\vec{v} - is the vector of its speed,

\vec{a} - is the vector of its acceleration,

q - it's electrical charge,

\vec{E} - intensity of the electrical field applied to it,

\vec{B} - vector of the magnetic induction.

Currently we don't take into account mutual influence of the simple charges. This would improve correctness of the model but for initial visualisation its influence is not a deciding factor.

5. ALGORITHM AND IMPLEMENTATION

Actual implementation of the calculation defined by the Lorentz force equation is given by the algorithm on Fig. 1.

For visualisation it is used SDL library [3]. Simple DirectMedia Layer is a C cross-platform multimedia library designed to provide low level access to the video framebuffer. Thus it provides high performance and portability to different computer platforms.

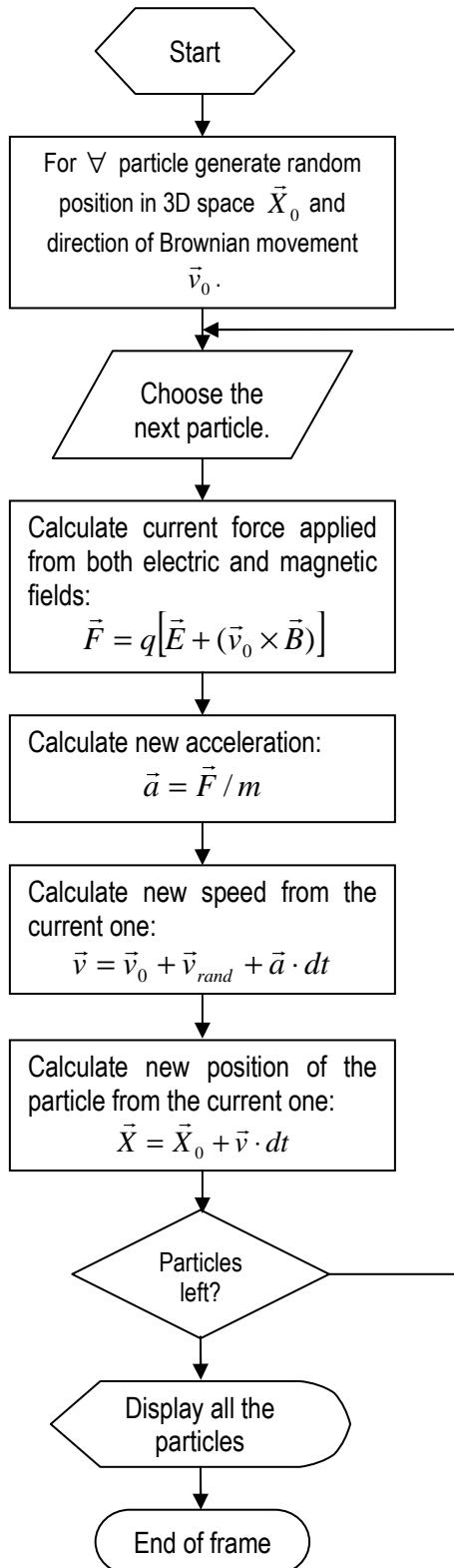


Fig. 1. Algorithm

For vector computation Eigen library is used [4]. Eigen is a C++ template library for linear algebra: vectors, matrices and related algorithms. It is versatile providing all needed operations in an elegant framework. But most of its virtue however is its speed thanks to C++ templates which enable optimisation of the code on multiple levels. Its performance is comparable with the traditionally unbeatable Fortran libraries. Syntax of the calculations is easy to use and intuitive.

Choice of the above two libraries, makes possible a visualisation of a large number of particles in real time on a personal computer.

6. SIMULATION RESULTS

Positions of the particles can be visualised using a 2D projection from their 3D simulated space as shown on Fig.2. This kind of view, although natural doesn't give much information on characteristics or the history of the process.

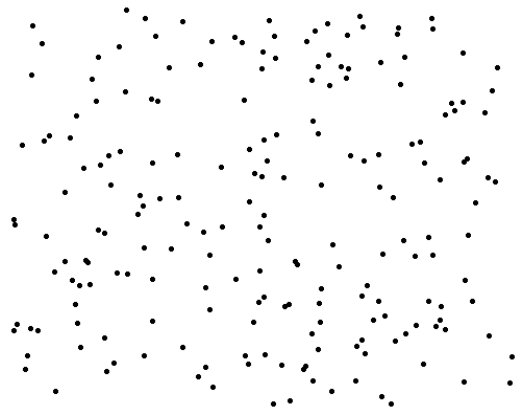


Fig. 2. Real time visualisation of the positions of the particles

Another much better approach is to give to user information of the trajectory of the particles. This method however is only practical for much smaller set of particles. Bigger sets of particles, very fast clutter the screen and make this type of visualization unusable.

As a first example of simulation we chose to use 20 particles put in a closed 3D space in electric field. It is applied using two electrodes, one above and the other below the simulated space. Intensity of the electric field \vec{E} is chosen to be constant for the whole volume. The boundaries of the volume make the particles reflect. The result is given on the Fig. 3.

It is clearly visible that main direction of movement is upwards and downwards which corresponds to the direction of the applied electric field.

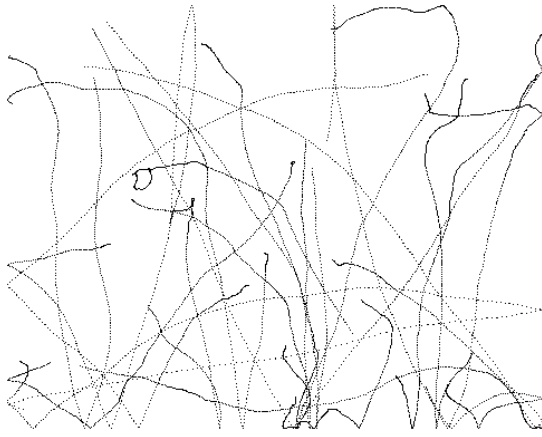


Fig. 3. Visualisation of the trajectory of the particles under constant electrical field

Next, Fig. 4 shows the result of the simulation for a similar setup where the two electrodes are substituted with a point charges. In this case the force is inversely proportional to the square of the distance between point charges and the particle.

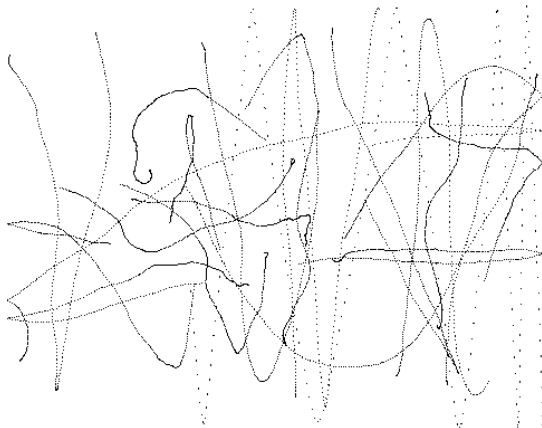


Fig. 4. Visualisation of the electrical field modelled by 1D Coulomb's law.

It is very well visible that the particles close to the point charges experience the strongest forces due to stronger electric field in proximity of the point charges. On the other hand the particles in the middle are not strongly affected by the electric field and perform quasi-random movement.

In described simulations only electric field is considered. Next step is to include the influence of the magnetic field as well, which is applied simultaneously to the electric one. On the next, Fig. 5 is shown the result of the simultaneous application of both fields. The electric field is applied using two electrodes, while the coil which generates magnetic field is in front and on the back of the volume on the image. Thus vector of the magnetic field corresponds to the direction of the viewing.

It is clearly visible that particles follow circular-like trajectories. This is a result of the force applied to them as a consequence of their movement and the magnetic field itself.

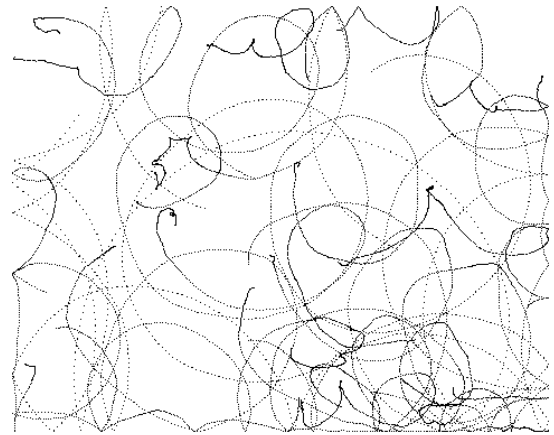


Fig. 5. Simultaneous influence of the electric and magnetic fields

Last simulation is of the same nature as the previous one with only one difference – the value of the applied magnetic field is larger. The result is shown on Fig. 6.

From the figure is visible that larger magnetic induction creates larger force and that leads to trajectories with smaller circles and much less drift of the particles from their original positions.

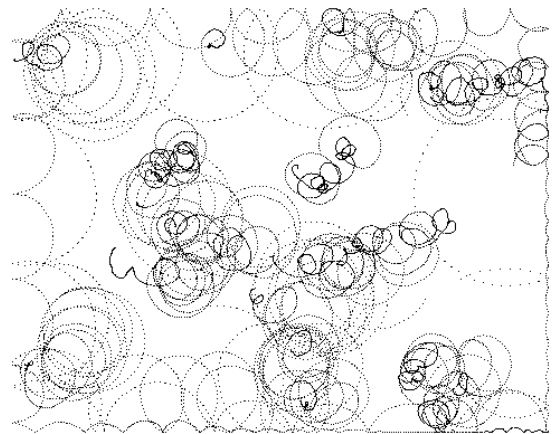


Fig. 6. Simultaneous influence of the electric and magnetic fields – different parameters

All of the given examples show that visual representation of the result of simulation can form intuitive understanding of the influence of electromagnetic field. Change of the configuration and/or the parameters have an easy visible change in particles behaviour.

7. FURTHER DIRECTIONS FOR DEVELOPMENT AND CONCLUSION

Further directions for work includes optimization of the algorithm to simulate larger volumes of particles in real time. Another possibility for speed up the simulation is to use programmable capabilities of modern graphics processing units of the PCs. Simulations like these are very well suited for a parallel computation and can lead to increased speed between one and two orders of magnitude.

Research needs to be done towards better and more intuitive methods of visualisation.

More complex shaped boundary conditions could be used to simulate different body tissues.

Presented simulations and their visualization give the physician outlook of the processes taking place in human body when electromagnetic field is applied. The ability to view, understand and control the treatment would be of great practical interest.

References

- [1] [http://en.wikipedia.org/wiki/Saline_\(medicine\)](http://en.wikipedia.org/wiki/Saline_(medicine))
- [2] http://en.wikipedia.org/wiki/Lorentz_force
- [3] <http://www.libsdl.org/>
- [4] <http://eigen.tuxfamily.org/>
- [5] D.Tz. Dimitrov, Computer Simulation of Space Configuration of Low Frequency Magnetic Field in Magnetotherapy, p.28-32, Electronics and Electrical Engineering, ISSN 1392-9631, 2005, -No.3(59),
- [6] Д.Ц.Димитров, Изследване на пространствената конфигурация на нискочестотно магнитно поле в магнито-терапията. стр.38-43. "Електроника и Електротехника", No.9-10, 2005

The paper is published with the financial support of the National Science Fund, Contr. № ДО 02-211/08

COMPUTER SIMULATION OF ECG SIGNAL RESTORATION

Mariya Nikolova¹, Tzveta Dimitrova²

¹Department of Mathematics and Informatics, N.Y.Vaptsarov NAVAL ACADEMY
73 V. Drumev St., Varna 9026, BULGARIA

²Technical University Sofia, 8 Bul. K. Ohridski
E-mail: mpn@abv.bg¹; tz.dimitrova@gmail.com²

Abstract

A computer simulation of loss of part of real ECG signal has been done in the paper. A restoration of ECG signal by using of mathematical method of Aizenberg for finite functions is described in the paper. The errors of signal's restoration in the cases of different number of values of loss have been calculated.

The software, which provides application of Aisenberg's method has been done in MATLAB. A comparison between obtained results and results of interpolation of ECG signals by function for interpolation in MATLAB has been done.

The application of Aizenberg's method has been confirmed by obtained results.

1. INTRODUCTION

When transmitting ECG signals, distortions occur, which can affect the exact diagnosis of patients. The morphology of ECG signal has been used for recognising much variability's of heart activity, so it is very important to get the parameters of ECG signal clear without noise [2, 4, 5]. This step gives a full picture and detailed information about the electrophysiology of the heart diseases and the ischemic changes that may occur like the myocardial infarction, conduction defects and arrhythmia. In order to support clinical decision-making, reasoning tool to the ECG signal must be clearly represented and filtered, to remove out all noises and artifacts from the signal. ECG signal is one of the biosignals that is considered as a non-stationary signal and needs a hard work to denoising. Interpolation of signal, which is lost at a certain time interval must be used. In regard to this, Aizenberg method for analytical continuation of finite functions may be used. The paper describes modeling of loss of real values of an ECG signal and their subsequent restoration. Signal restoration is done using Aizenberg formula [1] and the built-in function interp1 in Matlab [3]. Aizenberg method is applied for the first time in the restoration of one-dimensional real signal, recorded by the apparatus on the hard disk of the computer.

2. RESTORATION OF FINITE SIGNALS BY AIZENBERG METHOD

These ECG signals are one-dimensional finite signals. They are presented as functions of the time

in the positive direction of the axis t . This possibility of restoring the ECG signals is realized with the Aizenberg's formulae [1] for analytical continuation of finite functions from the Hardy's and Wiener's spaces. In short the method of Aizenberg consists in [1]:

If N_j is a limited sequence of different points in the halfplane $\{z_j \in D: \text{Im } z_j > -\sigma\}$ which has no points of density over its contour $1 \leq j \leq n$, let us consider the following problem of restoration of function $f(z)$ in D_σ where $D_\sigma = \prod_{j=1}^n \{z_j \in D: \text{Im } z_j > -\sigma\}$, in the set $M = N_1 \times N_2 \times \dots \times N_n$. For $N_l = \{x_{lj}\}$ is valid (1):

$$\omega(m, u, p, l) = \frac{x_{lp} - \bar{x}_{lp} + 2i\sigma \prod_{j=1, j \neq p}^m (u - x_{lj})(x_{lp} - \bar{x}_{lj} + 2i\sigma)}{u - \bar{x}_{lp} + 2i\sigma \prod_{j=1, j \neq p}^m (u - \bar{x}_{lj} + 2i\sigma)(x_{lp} - x_{lj})} \quad (1)$$

For $f \in H^2(D_\sigma)$, $z \in H^2(D_\sigma)$ is valid:

$$f(z) = \lim_{m \rightarrow \infty} \sum_{k_1=1}^m \sum_{k_2=1}^m \dots \sum_{k_n=1}^m f(x_k) \prod_{l=1}^m \omega(m, z_l, k_l, l) \quad (2)$$

$$x_k = (x_{1k_1}, \dots, x_{nk_n}), k = (k_1, \dots, k_n)$$

where H is a Hardy's class of functions, $\sigma > 0$ is a parameter, \bar{x} is a conjugate complex value of x .

The following formula can be used for interpolation of function $f(x)$ in Wiener class W_α^+ :

$$f(x) = \lim_{m \rightarrow \infty} \sum_{k=1}^m f(x_k) \frac{2i\sigma \prod_{j=1, j \neq k}^m (x - x_j)(x_k - x_j + 2i\sigma)}{x - x_k + 2i\sigma \prod_{j=1, j \neq k}^m (x - x_j + 2i\sigma)(x_k - x_j)} \quad (3)$$

Formula (3) contains two parameters m and σ ; The accuracy of signal restoration depends on their values. Results from previous experiments show that the number m of the known values of the signal must be not more than 30.

The parameter σ is defined by searching of the minimal root mean-square error ε by formula (4) between the real and interpolated values:

$$\varepsilon = \sqrt{\frac{1}{n} \sum_{i=0}^n (x_i - \tilde{x}_i)^2} \quad (4)$$

where x_i and \tilde{x}_i are the values of the real and restored signal.

3. COMPUTER SIMULATION OF ECG SIGNAL RESTORATION

Experiments were done in the Matlab software environment for interpolation of a real ECG signal, recorded by a cardiograph using the Aizenberg method and the built-in function `interp1` from Matlab. Data from echograph in the form of Microsoft Excel Workbook (xls).

The Excel table contains 3 columns of 7680 values for the cardiac signal parameters. Each of these columns is imported into the editor Matlab's Array Editor and stored as a separate variable in Matlab's Workspace. Then it is stored in Workspace as a .mat-file.

Program in the form of m-script, calling m-function is written, which implements formula (3). The algorithm of the program is as follows:

1. .mat-file with cardiogram data opens
2. The user enters the values of the start and end points of the readings of both intervals in which the signal of the first channel is known.
3. Function is called, in which formula (3) is programmed. The missing readings can be found by it using interpolation.
4. Graphs of the theoretical ECG signal and the signal obtained by formula (3) are plotted.
5. The results for the root mean-square error of the signal from the first channel are found.
6. Steps 2 - 5 are repeated for the signal from the second channel.

Computational experiments for restoration of the signal are performed by the use of the function `interp1` as well. Again, the root mean-square error of interpolation is calculated. `interp1` function uses the following methods:

'nearest' (Nearest neighbor interpolation); 'linear' (Linear interpolation) - default; 'spline' (Cubic spline interpolation); 'pchip' (Piecewise cubic Hermite interpolation); 'cubic' (Same as 'pchip'); 'v5cubic' (Cubic interpolation used in MATLAB 5).

Best results are obtained while using the method 'spline'.

4. RESULTS FROM COMPUTING EXPERIMENTS

Computing experiments for restoration of the missing 1 to 5 readings (values) of cardiogram for both channels were made. If there is loss of more values, it is considered that the ECG should be repeated.

Figure 1 shows the results from interpolation of a reading by Aizenberg method. The blue line displays the graph of interpolated signal, and the red line - the real signal from the ultrasonograph. Figure 1 and the subsequent Figures do not show the entire graph of the cardiogram, but only the part of it, which is used for the computation experiment on the purpose of more clear visualization of signals. The program enables the user to set different intervals for signal restoration for each channel. For the purpose of discussion, the signal for the first channel is named s_0 , and for the second - s_1 .

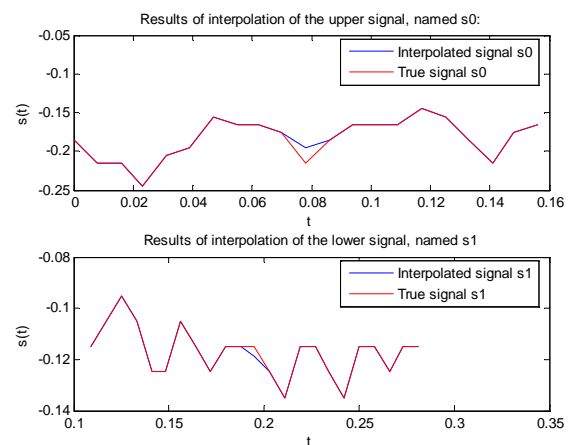


Fig. 1. Interpolation of one value according to Aizenberg's method

As it can be seen from Figure 1, interval of the known readings for the time $t \in [1 \ 10]$ and $t \in [12 \ 21]$ is set for the first channel, which implies that $t \in [0 \ 0.07]$ and $t \in [0.086 \ 0.1560]$. The value of the signal s_0 for $t = 0.078$ is interpolated. The interval of the known readings of s_1 is for $t \in [0.1090 \ 0.1880]$ and $t \in [0.2030 \ 0.2810]$. The value of the signal s_1 in $t = 0.1950$ is calculated by interpolation. The parameters m and σ in formula (3) are different for

the two signals - for s_0 : $m = 20, \sigma = 1$, for s_1 : $m = 22, \sigma = 0.1$. The values of the estimated root mean square errors are: for s_0 : $\varepsilon = 0.0043$, for s_1 : $\varepsilon = 0.00082757$. As it can be seen, the values of the root mean square errors are below 1%.

Figure 2 shows interpolation with the function `interp1`, when the spline method is used. The same value as in Figure 1 for the signal s_0 , i.e. $s_0(0.078)$ is interpolated. The blue dots in Fig. 2 indicate the known data (i.e. the basis points for interpolation), the graph of the interpolated function is depicted in green, and the real graph of s_0 is given in red.

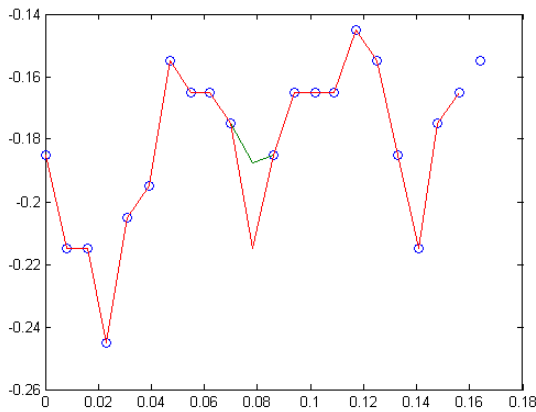


Fig. 2. Interpolation of one value from s_0 with the function `interp1` from Matlab

The root mean square error for signal restoration using `interp1` is 0.0051. The comparison between this value and the estimated value of the respective error in signal restoration of s_0 (and s_1) with interpolation by Aizenberg method proves the advantage of the latter to `interp1` with respect to the accuracy of interpolation. Similar results are obtained when interpolating s_1 by `interp1`.

Figure 3 shows the interpolation of 3 readings using Aizenberg method.

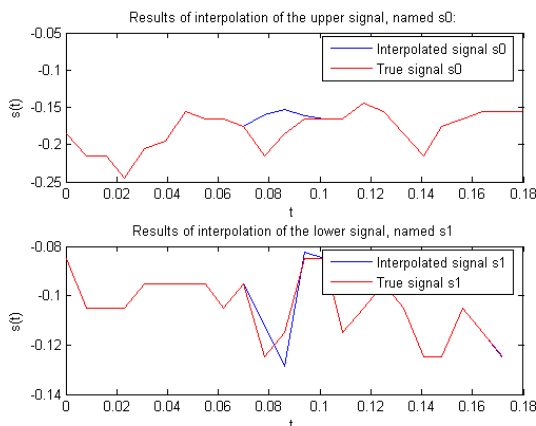


Fig. 3. Interpolation of three values according to Aizenberg's method

The readings for the two channels 11, 12, 13 are also restored, which means values of the signals s_0 and s_1 for $t = 0.0780, 0.0860, 0.0940$. Restoration errors are as follows: root mean square error for s_0 is 0.0137 and for s_1 is 0.000456. These values are smaller than the root mean square error calculated using `interp1` for interpolation of one value.

Figure 4 and Figure 5 show the interpolation of 5 values by Aizenberg method and by application of `interp1`, respectively.

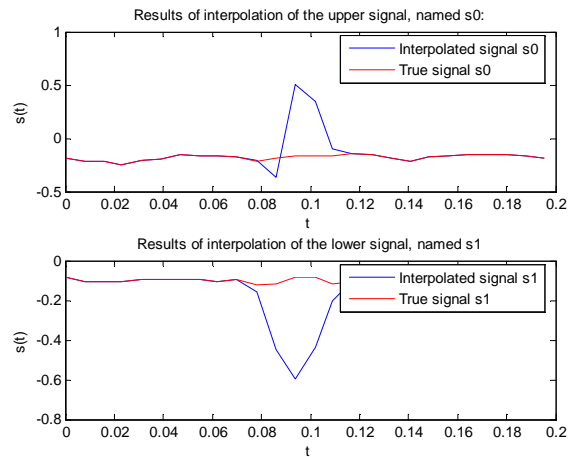


Fig. 4. Interpolation of five reads according to Aizenberg's method

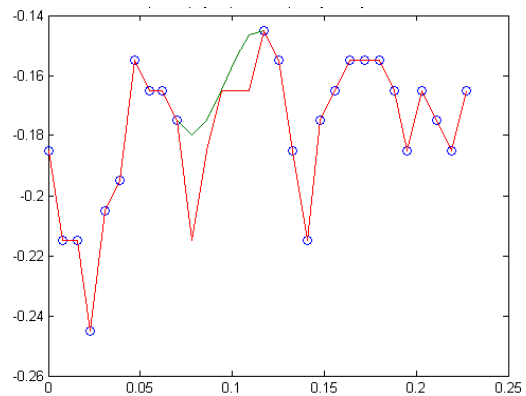


Fig. 5. Interpolation of five values from s_0 with the function `interp1` from Matlab

At restoration of 5 values better results are obtained using `interp1`. The two graphs show interpolation of readings from 11 to 15, i.e. for signals with values in $t = 0.0780, 0.0860, 0.0940, 0.1020, 0.1090$. The root mean square error in restoration using Aizenberg method is: for s_0 : $\varepsilon = 0.2095$, and for s_1 : $\varepsilon = 0.2577$. The root mean square error using `interp1` is 0.0139.

5. CONCLUSION

More accurate restoration of ECG signal in the case of loss of 1 to 4 values is done using the Aizenberg method. To obtain a smaller error in the interpolation, the optimal ratio between the parameters m and σ of the formula (3) must be calculated.

The need to obtain more precise restoration of the cardiac signal requires the use of both formula (3) of the Aizenberg method in case of fewer lost values - 1 to 4 readings, and the built-in function `interp1` (with spline method) in Matlab in case of loss of 5 readings.

Research activities in this field are under development, as experiments for extrapolation of cardiac signals are also planned.

References:

- [1] Aizenberg L., Dimiev S. P., Marinov M. S., Complex analysis and some applications, TU - Sofia, 1992, Bul.
- [2] Henzel N., and J. Leski, 1999. Efektywna obliczeniowo metoda analizy acyklicznych zdarzeń przy pomocy technik wieloczęstotliwościowych. XI konferencja Biocybernetyka i Inżynieria Biomedyczna, pp 188-122.
- [3] Matlab Help.
- [4] Thakor N.V., J. G. Webster, and J. Tompkins, 1985. Estimation QRS complex power spectra for design of QRS filter, IEEE Transactions on biomedical engineering, Vol. 31, pp: 702-706.
- [5] V.Almenar, A.Albiol, 1999. A new adaptive scheme for ECG enhancement, Signal Processing 75, pp: 253-265

The paper is published with the financial support of the National Science Fund, Contr. № ДО 02-211/08

MEDICAL DATA RISK EXPOSURE

Tzveta Dimitrova

BULGARIA
Technical University Sofia
8 Kl. Ohridski
Sofia 1000
e-mail: tz.dimitrova@gmail.com

Abstract

As networks are gradually turning into more intricate and accessible infrastructures, the threat environment is changing dramatically. New security risks are discovered every day in commonly used applications, operating Systems and network components. These are used by hackers and criminals to carry out attacks. With the increased dependency on information technology, the consequences of attacks are becoming increasingly severe. The victims are suffering from losses related to interruption in business, bad publicity and exposure of confidential information.

Medical organizations are forced to continuously maintain the protection of their networks. Traditionally, this has been accomplished by creating barriers against attacks by investing in reactive security tools such as firewalls, anti-virus tools and intrusion detection systems. In today's environment these reactive mechanisms simply are not enough. Instead of waiting for attacks to occur, there is a need to take a proactive approach. Only by using proactive security tools that continuously identify security risks, it is possible to effectively manage and reduce the risk exposure.

Legislation and compliance with security requirements are also becoming more demanding. The PCI (Payment Card Industry) security standards, Gramm Leach-Bliley act, HIPAA, Sarbanes-Oxley, among others all include requirements for regular testing of network security.

This article presents one of the steps in IT security applied in medical centers. This article, however, also points out that healthcare organizations appear to be increasingly vulnerable to exposing our personal health information as measured by the incidence of "reported" data breach incidents.

1. INTRODUCTION

In a paper-based charting environment (where most of the medical records reside nowadays), securing medical data – so-called Protected Health Information, or PHI – is a manual process.

Email communication, however, which flows across public, shared "information highways," is not suitable for PHI transmission, as it is not encrypted – in order to communicate PHI this way, a secure connection must be established. Secure web mail sites have been created which allow electronic transmission of PHI.

Secure websites with medical data have become an integral part of our day-to-daylife. People conduct both their personal and health-related information using these sites. Many consumers purchase medical goods online using sensitive credit card information.

Due to the sensitive nature of these sites, security is a top priority. They all deploy protocols such as SSL and many of them hire security experts to conduct vulnerability assessments.

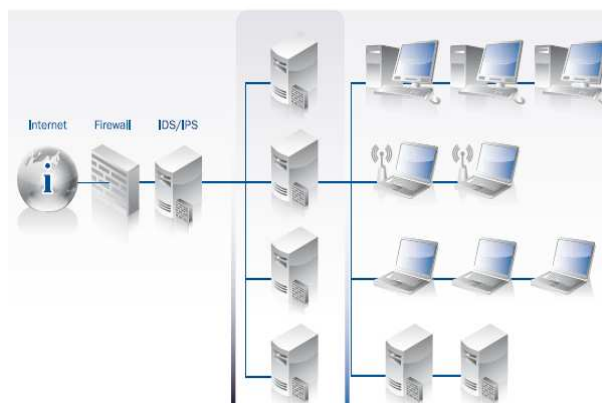


Fig. 1. Network accessible for vulnerabilities

2. MEDICAL INFORMATION VULNERABILITIES

When medical information is moved from paper onto an electronic platform, additional vulnerabilities for security breaches (i.e. theft) need to be identified and addressed. When implementing a local, client/server legacy EHR system, there are issues of securing the source of medical information (the server, which is the e-equivalent of the paper chart rack), as well as electronic transmission of data

across computer connections. If any PHI is stored locally onto workstations (which may occur, depending on the EHR system being used), then that workstation needs to have locks on it – password access to restart when timed out, as well as the need to have whatever PHI may be stored on the workstation encrypted too. A more significant risk is when the server is broken into and stolen, or local backup data devices are stolen. Physical theft of hardware containing PHI is an area of risk for local client/server EHRs and should be addressed by a policy and security plan at the local office.

3. VULNERABILITY ASSESSMENT AND MANAGEMENT

Vulnerability management is a process that can be implemented to make IT environments more secure and to improve an organization's regulatory compliance posture

The vulnerability management process includes these steps:

- Policy definition is the first step and includes defining the desired state for device configurations, user identity and resource access.
- Baseline your environment to identify vulnerabilities and policy compliance.
- Prioritize mitigation activities based on external threat information, internal security posture and asset classification.
- Shield the environment, prior to eliminating the vulnerability, by using desktop and network security tools.
- Mitigate the vulnerability and eliminate the root causes.
- Maintain and continually monitor the environment for deviations from policy and to identify new vulnerabilities.

The technology provided by vulnerability management vendors can be used to automate various aspects of the vulnerability management process. The four main technology categories are:

- Vulnerability assessment.
- Security configuration management and policy compliance.
- IT security risk management.
- Security information and event management (SIEM).

Using automated services is like having a highly skilled security team constantly probing your network to discover vulnerabilities. Identified vulnerabilities are rated and reported together with recommended remedy. The process of correcting identi-

fied vulnerabilities is supported by workflow tools for delegating remediation tasks to appropriate administrators. The results can also be compared over time, to monitor trends in risk exposure.

In contrast to manual penetration testing, automated vulnerability scanning is typically performed very frequently. This is important as new vulnerabilities are discovered in a high pace and your risk exposure increases in proportion to elapsed time since the last assessment of your network.

Other advantages of using normally automated services include:

- Proprietary technology
- 24/7 technical support
- Ease-of-use yet flexibility
- Cross platform support
- Maintains network availability
- Alignment with standards

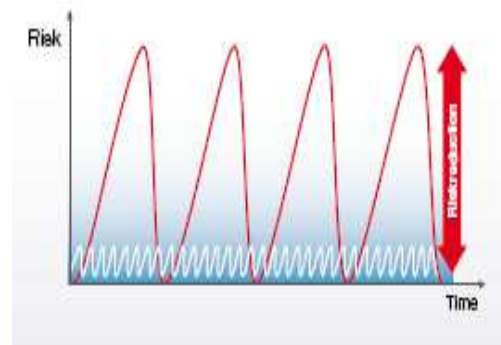


Fig. 2. Schematic risk exposures

4. METHODS USED BY CYBER CRIMINALS

You may ask yourself how is it possible for a cyber criminal to store child pornography on your computer without leaving any traces, how someone can get inside your corporate network to get their hands on your intellectual property and how such massive quantities of stolen financial account details, credit card numbers and personal identity information can be available for sale on the Internet? To straighten it out let's start with dividing attacks into two main groups; opportunistic and targeted attacks.

An opportunistic attack is when a cyber criminal targets potential victims randomly in the hope that some of them will be vulnerable to an attack. It is not important for the criminal who the victim is, but rather how many victims there are. For example, a cyber criminal stealing and trading stolen credit card information is likely to take an opportunistic approach as his income is in direct proportion to the

number of credit card details he can offer on the underground market. Mass mailing attacks are a typical opportunistic approach where the criminal only expects a low percentage of the targets to be affected.

In a targeted attack, the victim is a specific organization or person. Some possible scenarios could be cyber espionage, hijacking of a website due to political reasons, blackmailing or personal attacks for reasons of revenge. In general it is much harder to protect against a targeted attack, as the attack is tailored to make use of the specific security weaknesses you are exposed to rather than being a generic way of attacking the easiest targets, i.e. the least protected networks.

The traditional way of committing cyber attacks has been to send different types of malware, e.g. computer viruses or Trojan horses, in mass-mailing attacks to potential victims. Because commonly used anti-malware solutions today handle these kinds of opportunistic attack attempts quite well, the "effectiveness" of these kinds of attacks has definitely decreased.

But don't make the mistake of letting this give you a false sense of security. The cyber criminal community is very creative and dynamic in its nature. The methods for exploring the growing number of security weaknesses are constantly evolving. At the same time our network infrastructures are becoming increasingly complex, integrated, and open - which expands the attack surface for cyber criminals.

A very insidious way of committing cybercrime is to turn a legitimate website into a weapon to compromise and control computers that visit the website. This is achieved by injecting malicious code into the website by exploring vulnerabilities in the website architecture. Once the malicious code has been executed on your computer it is under complete control of the criminals, most likely without your knowledge. If your computer is connected to a network, you have now also provided the cyber criminals with an entry point to that entire network. Even worse, your computer can be used for criminal activities such as botnet attacks, where a large number of compromised computers are used as "weapons" by cyber criminals.

For targeted attacks, a very common approach is to hack into an organization's network by making use of security vulnerabilities that the infrastructure is exposed to. Vulnerabilities can be known security weaknesses or misconfigurations of any software or hardware component in the network. In fact, there

are tens of thousands of publicly known vulnerabilities, with numerous new vulnerabilities being discovered every day.

Hacking into networks may sound like something only a small community of very skilled technical people is involved in. However, that is no longer true since several different hacking tools are available for free or for sale in the underground communities.

The most popular hacking tools include:

Exploits – A small piece of code that explores specific vulnerabilities. This can be everything from exploits making use of general vulnerabilities in web browsers to exploits targeting site specific vulnerabilities on financial sites.

Autorooters – A tool that scans any specified network range for vulnerabilities. Found vulnerabilities are automatically explored by executing an exploit on the compromised computer providing the attacker with complete control of the computer. The autorooters then remove all traces of the intrusion by cleaning log files. According to Symantec, autorooters are available from \$40 with an average price of \$70.

The characteristics of a hacker have changed quite dramatically over the last few decades. The nice high school student in WarGames is no longer a good representative of today's heavy cyber criminals that are the brains behind the organized and economically devastating crimes being carried out today. The availability of easy-to-use tools for performing cyber-crime activities has definitely contributed to this development, luring in potential attackers all over the world and bringing cyber-crime to a completely new level.

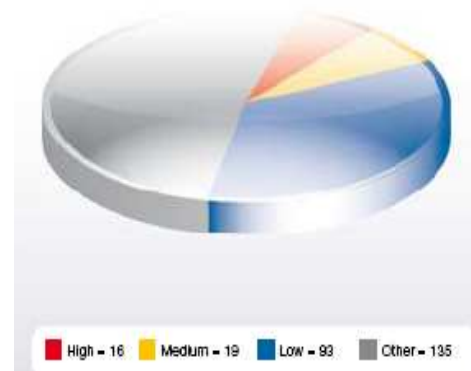


Fig. 3. Medical data risk exposure overview

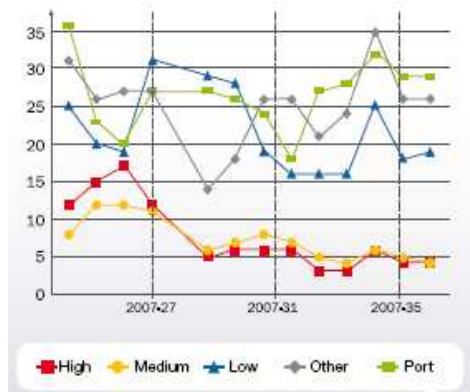


Fig. 4. Trend in risk exposure overview – weekly overview

5. CONCLUSION

As one can see, when health information moves from paper to local electronic systems, and then to hosted “cloud”-based systems, the risk of security breaches is actually *reduced*, provided that the vendors and systems utilized conform to specified standards covered by vulnerability management.

To summarize, cyber-crime has turned into a well-developed underground market of massive magnitudes. Attack methods are getting more sophisticated every day and organizations of all sizes are potential targets. So what can be done to protect your valuable assets?

First of all, it is important to take an overall approach to IT security. The chain is not stronger than the weakest link so it is crucial not to lose sight of the big picture. At the same time, we can conclude that most organizations have already implemented anti-malware software, firewalls and other reactive measures. Unfortunately, that is no longer enough. With today’s complex and open network infrastructures combined with a true explosion in security vulnerabilities in commonly used operating systems, applications, and hardware components a more proactive approach is needed.

In order to compromise a website or a network, cyber criminals, or the tools they are using, search for vulnerabilities to exploit. When visiting a website on which malicious code has been implanted, you are at greater risk of infection if your web browser has unknown vulnerabilities that can be exploited. Today, actively managing and eliminating vulnerabilities in order to reduce your risk exposure to an acceptable level is absolutely key. As new vulnerabilities are discovered at such a rapid pace, an automated approach that provides the ability to assess the network on a regular basis is the natural starting point.

References

- [1] L. Cranor, P. Guduru, and M. Arjula. User interfaces for privacy agents. *ACM Transactions on Computer Human Interaction*, 12(2):135–178, 2006.
- [2] R. de Paula and et. al. Two experiences designing for effective security. In *SOUPS '05: Proceedings of the second symposium on Usable privacy and security*, New York, NY, USA, 2005. ACM.
- [3] R. Dhamija, J. Tygar, and M. Hearst. Why phishing works. In *Proceedings of the SIGCHI Conference on Human Factors in Computing Systems*, 2006.
- [4] J. S. Downs, M. B. Holbrook, and L. F. Cranor. Decision strategies and susceptibility to phishing. In *SOUPS '06: Proceedings of the second symposium on Usable privacy and security*, New York, NY, USA, 2006. ACM.
- [5] D. Florencio and B. C. Cormac Herley. Do strong web passwords accomplish anything? In *Proceedings of the USENIX Workshop on Hot Topics in Security (HotSec)*, 2007.
- [6] L. Freed. State of customer satisfaction with online banking, forsee results/forbes.com, April 2007.

The paper is published with the financial support of the National Science Fund, Contr. № ДО 02-211/08.

CONTENT-BASED RETRIEVAL OF CALCIFICATION LESIONS IN MAMMOGRAPHY

Song Li-xin, Chang Rui-feng, Wang Qian

Harbin University of Science and Technology, Harbin 150040, China
T: 86-451-86396216; F: 86-451-86396201; E:lixins99@yahoo.com.cn

Abstract

In order to assist doctors to detect micro-calcifications, about the similar lesions retrieval problem of mammographic micro-calcification cluster, we develop a new algorithm with multi-feature fusion and relevance feedback based on the study of single feature and feature fusion using single distance measure image retrieving techniques, this method adopts multi-distance measure to calculate the similarity directing at different features. Experiment is based on mammography image database which contains 250 mammography images and each image contains calcification cluster, we verified the retrieval performance by the precision - recall ratio (PVR) of single feature, feature fusion and relevance feedback. Experimental results show that the method has a better retrieval result than these methods which based single feature and feature fusion which using single distance measurement.

Key words: mammography image, calcification lesions, Content-based Image Retrieval, feature fusion, relevance feedback, multi-distance measure

1. INTRODUCTION

With the number of medical images increasing, the capability to retrieval relevant images from large database is becoming more and more important. Although the progress made in general area of image retrieval in recent years, its success in biomedicine thus far has been quit limited [1]. In addition, mammography images have difference from general images, they have some characters, such as high gray-scale resolution, more visually similar. Therefore, it has more difficult to retrieve similar images in medical sense from database, it need to understand sufficiently the knowledge of diagnostic imaging, pathology and physiology [2]. It is an in-depth study problem that how to retrieve calcification lesions according to the characteristics of the mammography images, so that the retrieval result can help medical diagnosis.

At present, there are some works have explored the use of CBIR in mammographic calcification lesions retrieval. For example, El-Naqa et al. [3] proposed an approach to the retrieval of digital mammograms using micro-calcification clusters. They explored the use of neural networks and support vector machines, in a two-stage hierarchical learning network to predict perceptual similarity from similarity scores collected in human-observer studies. Chia-Hung Wei et al. [4] proposed the method that using six relevance feedback algorithms, which fall in the category of query point movement, for improving system performance. Although CBIR has

been many applications proposed for several applications abroad, one encounters a "semantic gap" between the quantitative features used to represent the images and the interpretation of the images by users who are experts in the domain of application [5]. This leads to the need to guide the retrieval algorithm by incorporating the user's judgment of similarity and the relevance of each retrieved [6, 7].

Because simple distance measure based on a single method of similarity measure calcification of breast lesions can not meet the similarity of retrieval results in the medical sense [3], in this paper, we propose a new similarity measurement that uses multi-distance, which was determined by he optimal query rules, it solved the defect of single distance existing, and combined with the user's relevance feedback to adjust the characteristics component weight dynamically, thus the similarity of medical sense was enhanced.

2. IMAGE RETRIEVAL ALGORITHM

2.1. Feature Extraction

Conventional content-based retrieval system aimed at improving the visual similarity between retrieval images and the query images, but the mammography images are visually similar, so the process of feature selection should not simply base on visual sense similarity. Therefore, doctors will be more inclined to see the same types of images as similar images, this is the medical sense similarity.

In this paper, feature selection bases on the following principles: if a feature was effective in classification, it was also effective in the retrieval [8]. At the same time, taking into account the performance and characteristics of calcifications, and in accordance with the theory of computer image recognition and machine vision, we use the following search features:

- (1) Gray-Scale Features: We extracted the mean, variance, kurtosis, skewness, entropy, and energy characteristics as the gray features.
- (2) Texture Features: We combine the Tamura [9] and Gabor [10] features to compose the texture feature.
- (3) Shape Feature: The shape feature is composed of the seven invariant moments [11] and five other features [3]: Cross sectional area, Compactness, Eccentricity, Density, Solidity.

Due to the ranges of feature components between each feature are different, we should normalize these feature components using Gauss normalization to make them have the same range [-1, 1].

The specific method is as following:

$$f_{i,j} = (f_{i,j} - \mu_i) / 3\sigma_i \quad (1)$$

Where $f_{i,j}$ denotes the feature component of feature f_i , μ_i and σ_i denote the mean and the standard deviation of f_i .

This allows almost all the characteristics value falling into the range of [-1, 1], the values outside the range are set to -1 and 1, so we assure all the values are in [-1, 1].

2.2. Image Retrieval based on feature fusion and multi-distance similarity measure

We integrate the gray-scale feature, shape feature and texture feature of the mammography images which contain micro-calcification cluster to retrieve the calcification lesions. At the same time, we adopt different distance measurement to compute similarity directing at lack of single distance measure.

As the important degree of every feature is different in retrieval, therefore, we should adjust the weight of these features before computing similarity. The specific method is as follows:

(1) all the weight $W = [W_i, W_{ij}]$ will be initialized $W0$ according to the number of the extracted features and feature components they in-

clude, so that all the features and characteristics of components have the same weight: $W_i = W0_{i_j} = 1/L$, $W_{ij} = W0_{i_j} = 1/J_i$, where L denotes the number of image features, J_i denotes a characteristic feature of the number of components.

(2) Calculating the similarity between the query image and database image:

$$D(f_i) = \sum_j W_{ij} D_i(r_{ij}), D = \sum_i W_i D_i(f_i) \quad (2)$$

Where D_i denotes the similarity among features, D denotes the total similarity.

2.2.1. Distance measure methods

At present, the common methods of similarity measure are as follows:

(1) Minkowski distance:

$$D(q, p) = (\sum_m (q_m - p_m)^L)^{1/L}$$

(3)

it is the Euclidean distance when $L = 2$.

(2) The histogram intersection distance:

$$D_{hi}(q, p) = 1 - \frac{\sum_{m=0}^{M-1} (h_q[m], h_p[m])}{|h_q|} \quad (4)$$

$$|h| = \sum_{m=0}^{M-1} h[m]$$

(3) Quadratic distance:

$$D(p, q) = \sqrt{(p_m - q_m)^T A (p_m - q_m)} \quad (5)$$

where $A = [a_{ij}]$ denotes the similarity matrix among features.

(4) Canberra Distance

$$D(q, p) = \sum_{m=0}^{M-1} |q_m - p_m| / (|q_m| + |p_m|) \quad (6)$$

2.2.2. The determination of the optimal similarity measure

We definite the optimal method of similarity measure in accordance with the optimal query rule to meet the similarity of mammographic calcification

lesions retrieval in medical sense. The basic idea of the optimal query rule is:

- (1) Every feature all has some measure methods, these combinations compose a collection, in the collection, every element expresses a query rule.
- (2) For every query rule, compute the similarity distance between the query image and all the images in the database. Sort the distance in ascending order and construct a length- $2N$ rank list (N is the number which the user specifies how many retrieval images to be returned). Every element in the list is the image id, the image is similar to the query image
- (3) Set the list that obtains in some query rule to reference list, the first N images in the reference are the retrieval results. At the same time, we obtain the corresponding list in accordance with the other query rules, define a rank function, it expresses rank number of the image in the list, if the images in the retrieval results is in the list, the function value is the rank number of the image in the list, otherwise, assign $2N+1$ to the function value.
- (4) For the each image in the reference list, compute the overall rank numbers, these rank numbers are obtained by every query rule, then establish a length- N combined rank list, which contains the overall most similar N images, then return them to the user.
- (5) The ranks for the retrieved images might not be the same as the user's perception, the user sends back a modified feedback rank list.
- (6) Compute the rank difference in every list (the rank sum of the absolute difference of the first N images before and after the reorder by the user), the smaller the difference the better the query rule.

By the optimal query rule which is introduced above, we get the optimal similarity measure: gray feature adopts quadratic distance, texture feature adopts Canberra distance, shape feature adopts the Euclidean distance.

2.2.3. The Normalization Among Features

The range of the similarity distance which obtained by different similarity measurement is not different, it causes the assignment imbalance of the weights, so we should normalize the distance. The method is as follows:

$$D_{i,j} = [1 + (\frac{D_{i,j} - \mu_{iD}}{3\sigma_{iD}})] / 2$$

(7)

$D_{i,j}$ is the similarity distance based on the feature part $f_{i,j}$ between the query image and all the images in the database, μ_{iD} and σ_{iD} denote the mean and the standard deviation respectively of the similarity distance vector.

We normalize all the similarity distance which obtained by different similarity measurement, it makes sure that all the distance have the same importance.

2.3. Relevance Feedback Algorithm

If we only use the bottom features of the image to retrieve the calcification lesion, it can not always meet the use's "semantic", we introduce relevance feedback algorithm in order to reduce the semantic gap between user and the retrieval result. The basic idea is: return the first N retrieved images to the user, the user estimates the relevant degree between each returned image and the query image according to the requirements and the subjective views. We adjust dynamically the feature weight by the feedback information, so as to improve the medical similarity.

The Specific method is as follows:

$RT = [RT_1, RT_2, \dots, RT_N]$ is the first retrieval result based on all features. The collection: $RT^{ij} = [RT^{ij}_1, RT^{ij}_2, \dots, RT^{ij}_N]$ is composed of the first N (in the experience, $N=32$) images which are retrieved according to a certain feature component r_{ij} , the user judge the relevance of each image that is in the RT^{ij} , we let Score denotes the collection of feedback scores which given by user.

$$score_i \begin{cases} = 1, & \text{relevant} \\ = 0, & \text{not sure} \\ = -1, & \text{not relevant} \end{cases}$$

Next, we calculate the weights. First of all, we initialize the weights: $W_{ij} = 0$, then calculate the weights as following:

$$W_{ij} = \begin{cases} W_{ij} + score_i & RT_i^{ij} \in RT \\ W_{ij} + 0 & RT_i^{ij} \notin RT \end{cases}$$

If $W_{ij} < 0$, W_{ij} will be set 0. Finally, we nor-

malize the weights: $W_{ij} = W_{ij} / \sum W_{ij}$.

We can carry out a new round retrieval by adjusting the weights as the above method introduced, it will be repeated until the user is pleased with the retrieval result.

3. EXPERIMENT AND RESULT ANALYSIS

The images used in the experiment are from the mammographic image database of the University of South Florida. The image contents were approved by clinical diagnosis and pathology. According to the doctor marked to the calcification cluster region, we extract 250 regions of interest (ROIs) which all contain calcification cluster. There are 145 ROIs which are malignant calcifications cluster, 105 ROIs are benign, the size of each ROI is 256×256 pixels.

We return the first five images to user as the retrieval result in the experiment. Because doctor are more inclined to consider the images which have the same kind lesions as the similar images, so we evaluate the retrieval performance according to this character.

We use query method of QBE (Query By Example), and select any image from the database as the query image to verify the retrieval performance by four methods. The experimental result shows the method that we proposed is superior to the traditional method which uses single-distance to measure similarity. Figure 1 is the result based on texture feature, Figure 2 is the result based on shape feature, Figure 3 is the result based on feature fusion using single distance, Figure 4 is the result based

on feature fusion using multi-distance, Figure 5 is the result based on feature fusion using multi-distance and relevance feedback.

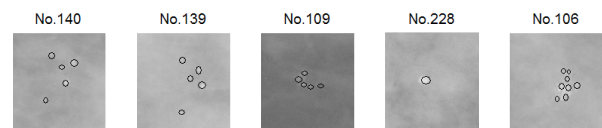


Fig. 1. The retrieval result based on texture feature

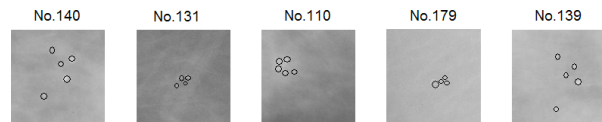


Fig. 2. The retrieval result based on shape feature

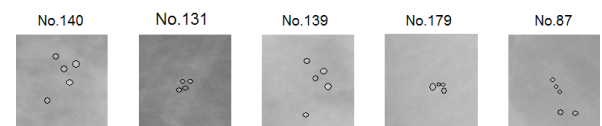


Fig. 3. The retrieval result based on single distance measure feature fusion

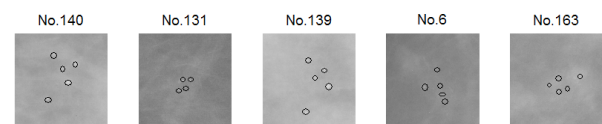


Fig. 4. The retrieval result based on multi-distance measure feature fusion

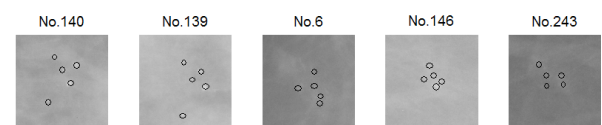


Fig. 5. The retrieval result based on feature fusion using multi-distance and relevance feedback

We choose 3 images from the database as the sample images to evaluate the precision-recall ratio of different methods quantitatively. See Table 1.

Table 1 the precision and recall based various feature and similarity measurement

feature	Image A		Image B		Image C	
	Precision	Recall	Precision	Recall	Precision	Recall
texture	0.77	0.34	0.75	0.46	0.69	0.62
shape	0.79	0.42	0.77	0.52	0.72	0.65
Mixed feature using single distance	0.81	0.58	0.79	0.65	0.76	0.72
Mixed feature using multi-distance	0.84	0.64	0.82	0.74	0.79	0.78
RF after 5 times	0.89	0.81	0.86	0.83	0.83	0.85

We can see from Table 1, the method based on multi-distance similarity measure has a higher precision-recall ratio, the effect is superior clearly to the methods based on single feature and feature fusion using single distance to measure the similarity. After

five times feedback, the recall and precision is improved markedly. But take into account the retrieval time, the feedback times should not too much. The retrieval result is closer to the user request by the feature fusion and relevance feedback.

4. CONCLUSION

We can see that the retrieval performance of the calcification lesion is related to the extracted features and the method that measures the similarity by the experiment. The method based on feature fusion and relevance feedback that we have adopted enhanced the validity of the retrieval technology of the mammographic calcification lesion, and we adopted using multi-distance to measure the similarity which determined by the optimal query rule, the precision ratio is improved. Due to features are extracted are more, the computing speed is slower, we should consider the characteristics optimization problems, at the same time, in order to reduce the function of user demand and the gap between systems, we should combine the low-level features and semantic features, thereby, it provide better assisted diagnosis of mammographic calcification lesions to doctor.

Reference

- [1] S. Wong. CBIR in medicine: still a long way to go. IEEE Workshop on content-Based Access of Image and Video Libraries, Santa Barbara, CA, June, 1998.
- [2] Shao Hong, Cui Wen cheng, Zhao Hong. Research of content- based image retrieval technology [J]. Mini-Micro Systems, 2003, 24(10):1845-1848.
- [3] El- Naqa I, Yang Y, Nishikawa RM et al. A similarity learning approach to content-based image retrieval: application to digital mammography [J]. IEEE Trans Med Imaging, 2004, 23: 1233–1244.
- [4] Chia-Hung Wei, Chang-T, Sun Li. Calcification Descriptor and Relevance Feedback Learning Algorithms for Content-Based Mammogram Retrieval [C]. Springer-Verlag Berlin Heidelberg, Susan M. Astley et al. (Eds.): IWDM 2006, LNCS 4046, 2006: 307-308.
- [5] Müller H, Michoux N, Bandon D. A review of content-based image retrieval systems in medical applications clinical benefits and future directions [J]. Int J Med Inform 2004,73:1–23.
- [6] Baeza-Yates RA, BA. Modern information retrieval. Addison- Wesley, Wokingham.1999.
- [7] Ortega- Binderberger M, Mehrotra S Relevance feedback in multimedia databases[C]. In: Furht B, Marques O(eds) Handbook of video databases—design and applications. CRCPress, Boca Raton, 2003: 511–536.
- [8] Ren-chao Jin, Bo Meng, En-ming Song. Content-based Image Retrieval for Computer-aided Detection of Mammographic Masses [J]. Mini- Micro Systems,2008, 29(2), 326- 327.
- [9] Quan-ming Zhou, Guo-hua Geng, Na Wei. Content-Based Image Retrieval Technology [M]. 2007, 5: 100- 101.
- [10] Zhi-jie Qiao, Jia-fu. Jiang Texture Image Retrieval Based on Gabor Wavelet Transform [D]. 2006: 22- 23.
- [11] Fan Ya-chun, Geng Guo-hua, Zhou Quan-ming. Shape-Based Retrieval Using Invariant Moments and Edge Direction. Mini- Micro Systems, 2004, 25(4):659-660.

ON APPLICATION OF CORRELATION DIMENSION FOR EEG ANALYSIS OF PATIENTS WITH EPILEPSY

Natalia Ampilova,

*St. Petersburg State University, Dept. Computer Science
St. Petersburg, Zagrebski bul. 35/28, ap.320
192283 Russia
E-mail. nataly@is1483.spb.edu*

Darina Nikolaeva,

*St. Petersburg State University, Dept. Computer Science
E-mail. Nicolaeva Darina <darina@math.spbu.ru>*

Abstract

This article is concerned with obtaining numerical values of EEG to recognize records that are specific for epilepsy. The correlation dimension of restored attractor is supposed to be such a characteristic.

The method of restoration of the attractor of a system by a time series was applied. Under certain conditions relating to the series length and delay value this method enables one to obtain numerical characteristics of complex processes. To calculate correlation dimension Grossberger-Procaccia procedure, which is in common use in practice, was employed.

In this work the mentioned method was used to study the dynamics of α -rhythm. The patterns of EEG of a patient with generalized epilepsy were studied. The results of experiments show that correlation dimension for the canals corresponding to lesion focus less than such a characteristic for healthy patients. Apart from that the decrease of correlation dimension extends to adjacent areas of brain, which corresponds to and may lead to the appearing α -rhythm in frontal parts (α -synchronization phenomena).

1. INTRODUCTION

EEG of human brain is the record of its bioelectrical activity. When the signal is registered, a sequence of numerical values is obtained. Hence we have a time series that may be considered as a result of functioning of some complex dynamical system. The application of nonlinear dynamics methods for the analysis of time series allows us to restore properties of the system generating the series. The dynamics of a system is characterized by its invariant sets (in particular - attractors). By using Takens method for the time series analysis we can find a restored attractor. We calculate correlation dimension of the attractor to estimate the complexity of the system.

In our case this characteristic is decreasing for patients with epilepsy. Moreover, the comparison of correlation dimensions for different canals allows us to find α -synchronization phenomena.

2. MAIN NOTIONS

According to current concepts, excitation of neurons appears as a result of their polarization and depolarization. The bioelectrical currents which occur in this process interact with each other and form a complex interference curve EEG [1].

The main goal of encephalography is a registration and an analysis of EEG. It means a localization of significant features, an identification of their parameters and formulation of a conclusion.

As EEG is a random oscillating process, its main characteristics are frequency, amplitude, and phase. Frequency rhythm is a type of electrical activity corresponding to a state of the brain. (There are 4 main rhythms: alpha-, beta-, delta-, theta-.) Phenomenon is a part of EEG which is differ from the background record and has the diagnostic value for analysis. One of the most important phenomena is epileptic activity [2].

It is well known that high level of functional brain activity which corresponds to an emotional tension results in increasing the size of the information that the brain can assimilate. In this case neurons are in considerable autonomy and such a process is characterized by desynchronization in summary electrical activity. When the level of functional activity is decreasing, some neurons unite into large synchronized groups. In this connection neurons do not enter into a new activity. Such an activity of synchronized neurons correspond to a reduced brain functioning. It should be noted that a distinguishing characteristic of brain at epilepsy is a synchronization of neuron activity. It turns out that using the

methods of nonlinear analysis may be applied to obtain a numerical value for such synchronization. It is the correlation dimension of an attractor that may be restored using EEG time series.

3. METHOD OF ANALYSIS

We apply methods of nonlinear dynamics [3] to analyze time series that are EEG records.

The method is based on the following idea. Let f be a dynamical system defined on a manifold M , $\dim M=d$ and our time series is a result of its functioning. Let $x(t_i)$ be a value of the time series at the moment t_i . For an integer m form m -dimensional space R^m (embedding space) of vectors $z_i=\{x(t_i), x(t_i+\tau), \dots, x(t_i+(m-1)\tau)\}$ for all i from 1 to N , where N is the length of the series. So, we have a mapping g that maps $x(t_i)$ in z_i . Takens theorem claims that generic property of g is that for $m \geq 2d+1$ it is embedding. Hence $g(M)$ has not self-intersections and g is nondegenerate transformation. It is well known that correlation dimension is invariant relatively g . By this means we can calculate correlation dimension using experimental data (time series) and by doing so obtain a result for initial system f .

Now we take an increasing sequence $\{m_j\}$ and repeat the described procedure to compute sequential values of correlation dimensions of obtained spaces --- $C(m_j)$. If $C(m_j)$ stabilizes then m_j is the dimension of the embedding space, being the dimension of the restored attractor not greater than $(m_j-1)/2$. If stabilization does not occur the considered series is the record of a random process.

Correlation integral is defined by the formula:

$$C(\epsilon) = \frac{1}{N^2} \sum_{i,j=1, i \neq j} \Theta(\epsilon - |x_i - x_j|) \quad (1)$$

where $\Theta(x)$ – Heviside function:

$$\Theta(x) = \begin{cases} 0, & x < 0 \\ 1, & x \geq 0 \end{cases}$$

N – the length of the series, ϵ – distance, x_i, x_j are elements of a sample. Correlation dimension D_c is defined by the formula

$$D_c = \lim_{\epsilon \rightarrow 0} \frac{\log C(\epsilon)}{\log \epsilon}$$

For small ϵ $\lim_{\epsilon \rightarrow 0} \frac{C(\epsilon)}{\epsilon} \approx \epsilon^{D_c}$, hence

$$\log C(\epsilon) = D_c \log \epsilon + const, \text{ and}$$

$$D_c = \frac{\log C(\epsilon) - const}{\log \epsilon}$$

We can calculate correlation integral (1) for x_i and reconstructed vectors z_i . In the second case correlation dimension depends not only on ϵ , but from the parameters of reconstruction m and τ .

It should be noted that in practice we have problems concerning both the boundedness of a time series and the stationarity of the object under investigation. EEG that is recorded over along period of time is not stationary process. The process may be considered as stationary one if a part of the record by length not greater than 1s is investigated.

4. RESULTS

We use described algorithms to implement an application for EEG analysis and calculation. The application computes correlation integral for a given time series and τ and shows EEG record; computes correlation integral for each canal; construct images of attractors in two-dimensional phase space; plots graphs of dependence obtained correlation dimension on the dimension of embedding. Package TISEAN [4] was used to calculate correlation integral.

When working we analyzed 3 EEG records of a patient with epilepsy: 1 --- before stimulation, 2 --- few days after stimulation and 3 --- a month after it. Every record was divided into equal time parts (to satisfy stationarity condition); correlation dimension was calculated for each fragment and averaged. The results are shown in the table.	Dc .av - 1	Dc .av - 2	Dc .av - 3
Fd2	6,27	6,8	6,37
Fs2	5,91	6,9	6,16
Od	5,99	5,76	5,70
Os	6	6,4	5,86

In the process of EEG analysis the brain areas for which correlation dimension is small enough were determined. It points to the fact that at epilepsy a system of brain functioning becomes simpler and depends on smaller number of parameters than for normal state. As this takes place a process of synchronization accompanies to the lowering correlation dimension. Lesion focuses cover adjacent brain areas.

For normal state there is no α -rhythm in frontal parts of brain, whereas at epilepsy α -rhythm may appear in these parts as a result of synchronization. отделами. We study a frontal-occipital relation to reveal distant synchronization of α -rhythm in frontal areas.

5. CONCLUSIONS

The method of estimation of correlation dimension applied to the analysis of EEG of patients with epilepsy allows us to separate systems controlled by small number of parameters from "random" systems. On the canals where Dc did not achieve saturation the systems generating EEG are controlled by large numbers of parameters and close to random systems.

Close values of Dc obtained for different canals when m is increasing may be a sign of synchronization of neuron activity.

Our method may be applied to obtain numerical characteristic to analyze α -rhythm synchronization phenomena.

6. ACKNOWLEDGEMENTS

Authors wish to express their thanks to Neurosurgical Institute by A. Polenov for given data.

References

- [1] Vasserman E..L. Methodic aspects of numerical electroencephalography (in Russian), Saint-Petersburg, 2002.
- [2] Zenkov L.R. Clinical electroencephalography (with elements of epileptology) (in Russian) . Taganrog, 1996.
- [3] Malinetsky G.G., Potapov A.B. Contemporary problems of nonlinear dynamics (in Russian). Moscow, 2001.
- [4] R. Hegger, H. Kantz, and T. Schreiber, Practical implementation of nonlinear time series methods: The TISEAN package, CHAOS 9, 413 (1999) (http://www.mpipksdresden.mpg.de/~tisean/TISEAN_2.1/index.html)

INTELLIGENT MODULE FOR DATA EXCHANGE USING CAN INTERFACE

Ljudmila Roumenova Taneva

Technical University – Sofia,
Technological School „Electronic Systems“
Sofia, Mladost 1,
T.02 8751094; E. lusy_t@yahoo.com.

Abstract

The paper describes a CAN-bus based control system with changeable message priority. The system consists of microcontroller MSP430F149 (TI), sensors, CAN controller and several subsystems typical for the automotive industry and the industrial automation.

The CAN bus system is a multi-master system and the arbitration of the access to the bus is based on the transmitting devices' unique priority codes which are usually fixed. The priority code of the transmitting device determines the priority of the message transmitted by it.

In the proposed system the priority of the messages could be changed dynamically according the process stage and fixed priorities of the other nodes connected to the network.

The intelligent CAN controller increases the quality of the controlling complex processes and reduces the used hardware.

1. INTRODUCTION

The Controller-Area-Network (CAN) bus provides high level of noise immunity and fault tolerance [1]. For this reason it dominates the automotive industry and is widely used in industrial automation, military and many other areas characterized with harsh environment [2].

The CAN bus is a balanced (differential) 2-wire interface running over either a Shielded Twisted Pair (STP), Un-shielded Twisted Pair (UTP), or Ribbon cable. The bus is controlled by CAN controller and the devices interface with it via transmitters. The CAN controller also queues the incoming and outgoing messages [3]. These messages are usually broadcasted, i.e. sent to all bus participants simultaneously.

The transmission rate depends on the bus length. For buses shorter than 40 meters, the transmission rate is up to 1Mbits/s. Due to the practical limitation of the transceivers, in a single system could be linked up to 110 nodes (fig.1).

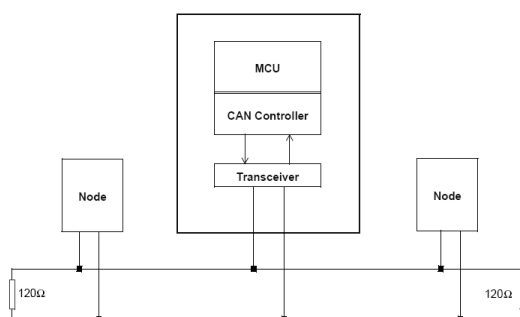


Fig. 1. CAN network

The messages with higher priority are always transmitted, but sometimes at the expense of the lower priority ones [4]. By loading the bus heavily it is possible for higher priority messages to interfere with the timely delivery of the low priority ones or even “block” them, not allowing transmission at all.

The developed intelligent CAN controller makes program changes of the message priority. The algorithm is preliminary defined and the microcontroller executes it. CAN protocol does not use physical addresses and sends messages with identifier that can be recognized by the various nodes. The identifier is used for message filtering and for determining message priority. The recipient node address in both transmit and receive modes is placed in the identifier as well.

2. PRINCIPLES OF DATA EXCHANGE

CAN is based on the “broadcast communication mechanism”, which is based on a message-oriented transmission protocol. It defines message contents rather than stations and station addresses [2]. Every message has a message identifier, which is unique within the whole network since it defines content and also the priority of the message. The level of importance is used when several stations compete for bus access (bus arbitration) [1]. As a result of the content-oriented addressing scheme a high degree of system and configuration flexibility is achieved. It is easy to add stations to an

existing CAN network without making any hardware or software modifications to the present stations as long as the new stations are purely receivers. This allows for a modular concept and also permits the reception of multiple data and the synchronization of distributed processes. Also, data transmission is not based on the availability of specific types of stations, which allows simple servicing and upgrading of the network.

In real-time processing the urgency of messages to be exchanged over the network can differ greatly: a rapidly changing dimension, e.g. engine load has to be transmitted more frequently and therefore with less delays than other dimensions, e.g. engine temperature. The priority, at which a message is transmitted compared to another less urgent message, is specified by the identifier of each message. The priorities are set during system design in the form of corresponding binary values and cannot be changed dynamically. The identifier with the lowest binary number has the highest priority.

Bus access conflicts are resolved by bit-wise arbitration of the identifiers involved by each station observing the bus level bit for bit. This happens in accordance with the wired-and-mechanism, by which the dominant state overwrites the recessive state. All those stations (nodes) with recessive transmission and dominant observation lose the competition for bus access. All those "losers" automatically become receivers of the message with the highest priority and do not re-attempt transmission until the bus is available again.

Transmission requests are handled in order of their importance for the system as a whole. This proves especially advantageous when system is overloaded. Since bus access is prioritized on the basis of the messages, it is possible to guarantee low individual latency times in real-time systems.

2.1. Message frame formats

The CAN protocol supports two message frame formats, the only essential difference being the length of the identifier (fig.2). The "CAN base frame" supports a length of 11 bits for the identifier (formerly known as CAN 1.0 A), and the "CAN extended frame" supports a length of 29 bits for the identifier (formerly known as CAN 2.0 B).



Fig. 2. Message frame format

2.1.1. CAN base frame format

A CAN base frame message begins with the start bit called "Start Of Frame (SOF)", this is followed by the "Arbitration field" which consist of the identifier and the "Remote Transmission Request (RTR)" bit used to distinguish between the data frame and the data request frame called remote frame. [2] The following "Control field" contains the "Identifier Extension (IDE)" bit to distinguish between the CAN base frame and the CAN extended frame, as well as the "Data Length Code (DLC)" used to indicate the number of following data bytes in the "Data field". If the message is used as a remote frame, the DLC contains the number of requested data bytes. The "Data field" that follows is able to hold up to 8 data byte. The integrity of the frame is guaranteed by the following "Cyclic Redundant Check (CRC)" sum. The "ACKnowledge (ACK) field" compromises the ACK slot and the ACK delimiter. The bit in the ACK slot is sent as a recessive bit and is overwritten as a dominant bit by those receivers, which have at this time received the data correctly. Correct messages are acknowledged by the receivers regardless of the result of the acceptance test. The end of the message is indicated by "End Of Frame (EOF)". The "Intermission Frame Space (IFS)" is the minimum number of bits separating consecutive messages. Unless another station starts transmitting, the bus remains idle after this.

2.1.2. CAN extended frame format

The difference between an extended frame format message and a base frame format message is the length of the identifier used. The 29-bit identifier is made up of the 11-bit identifier ("base identifier") and an 18-bit extension ("identifier extension"). The distinction between CAN base frame format and CAN extended frame format is made by using the IDE bit, which is transmitted as dominant in case of an 11-bit frame, and transmitted as recessive in case of a 29-bit frame. As the two formats have to co-exist on one bus, it is set which message has higher priority on the bus in the case of bus access collision with different formats and the same identifier / base identifier: The 11-bit message always has priority over the 29-bit message. The extended format has some trade-offs: The bus latency time is longer (in minimum 20 bit-times), messages in extended format require more bandwidth (about 20

%), and the error detection performance is lower (because the chosen polynomial for the 15-bit CRC is optimized for frame length up to 112 bits). CAN controllers, which support extended frame format messages are also able to send and receive messages in CAN base frame format. CAN controllers that just cover the base frame format do not interpret extended frames correctly. However there are CAN controllers, which only support the base frame format, recognize extended messages and ignore them.

3. MODULE PRINCIPLE OF OPERATION

The developed intelligent CAN controller uses 12-channel 12-bit ADC to receive data from various sensors. The used microcontroller (MSP430F149) [1] receives information from the sensors, calculates data and transmits message via CAN bus to the receiving nodes (fig.3). As transmitter is used CAN transceiver 82C250, Philips [3]. It operates in differential mode with inverted signals CAN_H and CAN_L.

For example, if the system consists of five nodes, the priority of each node is fixed from 0 to 8 and 0 is the highest priority.

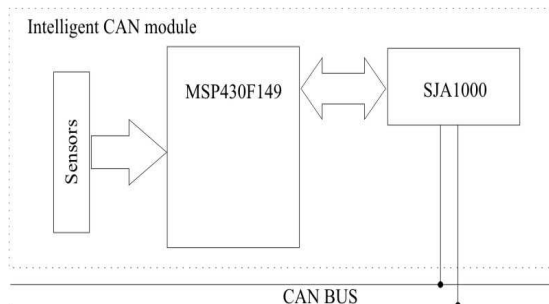


Fig. 3. Intelligent CAN controller

In the complex processes the importance of the parameters are different in the different stages of the process. To escape the loss of information, the sample rate and the message priority have to be changed depending on the algorithm of the program. At least two unique identifiers will have to be reserved for the intelligent CAN module (in this case four identifiers: 0, 2, 5, 8). The priority of the module will be changed according the algorithm when conditions for the parameters values are in the preliminary defined limits. If one of the conditions is available, the intelligent CAN controller changes the level of its own priority, righting 0 or 2, 5, 8 in the area of identifier.

The basic algorithm which the microcontroller executes is the follow: The microcontroller permanently receives the signals from the sensors, calculates data and store the result in the variable. When there is a request from the CAN Host node, the microcontroller sends the last actualization of this variable.

For example, if the measured signal is temperature, in this way the Host node receives the data in suitable type. It is not necessary to make additional calculations.

The algorithm calculates data in the measured unit, which is used by the Host node. If the Host node sends a command for continuous transmitting, transmits the value on every measurement. The program informs the Host node when the data is equal to the value, defined before,

4. CONCLUSION

The paper describes a CAN-bus based control system with non-fixed message priority. This intelligent CAN controller increases the quality, reliability and flexibility of the controlling complex processes and reduces the used hardware.

References

- [1] Application Reports, TI, "MSP430 Family Mixed-Signal Microcontroller", 2003.
- [2] R. Bosch, "CAN Specification", Robert Bosch GmbH, Stuttgart, 1991.
- [3] Data Sheet, "PCA82C250 CAN controller interface", Philips, 2000.
- [4] Docheva L., Al. Bekiarski ,I. Dochev, Analysis of Analog Neural Network Model With CMOS Multipliers, Proceedings of Czech and Slovak Technical Universities and URSI Committees, Journal Radioengineering, vol.16, №3, pp. 103-107, 2007.